AUTOMATIC CARRIER LANDING SYSTEM FOR V/STOL AIRCRAFT USING $\mathcal{L}_1$ ADAPTIVE AND OPTIMAL CONTROL

by

SHASHANK HARIHARAPURA RAMESH

Presented to the Faculty of the Graduate School of
The University of Texas at Arlington in Partial Fulfillment
of the Requirements
for the Degree of

MASTER OF SCIENCE IN AEROSPACE ENGINEERING

THE UNIVERSITY OF TEXAS AT ARLINGTON

December 2015

To my parents, Meera and Ramesh

ACKNOWLEDGEMENTS

My deepest gratitude goes to my supervising professor, Dr Kamesh Subbarao for providing me an opportunity to work on a topic of my interest, for his guidance and encouragement for research. I would like to thank Dr. Atilla Dogan and Dr. Donald Wilson for being a part of my thesis committee.

I am thankful to my colleagues at Aerospace Systems Laboratory - Dr Ghassan Atmeh, Dr Pavan Nuthi, Dr Alok Rege, and Pengkai Ru, for their invaluable inputs towards my research. Many thanks to Ameya Godbole, Tracie Perez, Paul Quillen and Ziad Bakhya for their support and encouragement.

I would like to thank my roommates Vijay Gopal, Varun Vishwamitra, and Rohit Narayan for their patience, tolerance, and brotherly affection without which my sojourn at graduate school would have been burdensome.

I would like to thank my parents for their unconditional love and support. It is only because of their dedication, hardwork, and sacrifice I am what I am today. I am thankful to my sister, Shobhita, and my grandmothers, for their moral support which provided me the strength to deal with uneasy times. Special thanks to my aunt and uncle, Shubha and Ravi Murthy who have been extremely supportive during my stay in USA.

December 8, 2015

ABSTRACT

AUTOMATIC CARRIER LANDING SYSTEM FOR V/STOL AIRCRAFT USING $\mathcal{L}_1$ ADAPTIVE AND OPTIMAL CONTROL

SHASHANK HARIHARAPURA RAMESH, M.S.

The University of Texas at Arlington, 2015

Supervising Professor: Dr Kamesh Subbarao

This thesis presents a framework for developing automatic carrier landing systems for aircraft with vertical or short take-off and landing capability using two different control strategies - gain-scheduled linear optimal control, and $\mathcal{L}_1$ adaptive control. The carrier landing sequence of V/STOL aircraft involves large variations in dynamic pressure and aerodynamic coefficients arising because of the transition from aerodynamic-supported to jet-borne flight, descent to the touchdown altitude, and turns performed to align with the runway. Consequently, the dynamics of the aircraft exhibit a highly non-linear dynamical behavior with variations in flight conditions prior to touchdown. Therefore, the implication is the need for non-linear control techniques to achieve automatic landing. Gain-scheduling has been one of the most widely employed techniques for control of aircraft, which involves designing linear controllers for numerous trimmed flight conditions, and interpolating them to achieve a global non-linear control. Adaptive control technique, on the other hand, eliminates the need to schedule the controller parameters as they adapt to changing flight conditions.

A fully-non-linear high fidelity simulation model of the AV-8B is used for simulating aircraft motion, and to develop the two automatic flight control systems. Carrier motion is simulated using a simple kinematic model of a Nimitz class carrier subjected to sea-state 4 perturbations.

The gain-scheduled flight control system design is performed by considering the aircraft's velocity, altitude, and turn-rate as scheduling variables. A three dimensional sample space of the scheduling variables is defined from which a large number of equilibrium flight conditions are chosen to design the automatic carrier landing system. The trim-data corresponding to each flight condition is extracted following which the linear models are obtained. The effects of inter-mode coupling and control-cross coupling are studied, and control interferences are minimized by control decoupling. Linear optimal tracking controllers are designed for each trim point, and their parameters are scheduled. Using just two linear models, an $\mathcal{L}_1$ adaptive controller is designed to replace the gain-scheduled controller. The adaptive controller accounts for matched uncertainties within a control bandwidth that is defined using a low-pass filter.

Guidance laws are designed to command reference trajectories of velocity, altitude, turn-rate and slip-velocity based on the deviation of the aircraft from a predefined flight path. The approach pattern includes three flight legs, and culminates with a vertical landing at the designated landing point on the flight deck of the carrier.

The simulations of automatic landing are performed using SIMULINK® envrironment in MATLAB ®. The simulation results of the automatic carrier landing obtained using the gain-scheduled controller, and the $\mathcal{L}_1$ adaptive controller are presented.

TABLE OF CONTENTS

LIST OF ILLUSTRATIONS

LIST OF TABLES

CHAPTER 1

BACKGROUND AND MOTIVATION

Aircraft carrier landings have been regarded as one of the most challenging phases of flight due to the extremely tight space available for touchdown on the flight-deck of a ship or aircraft carrier. Night operations, rough seas, and adverse weather conditions further increase the risks associated with carrier landing, sometimes making manual landings impossible. After flying for long hours on combat missions, executing a shipboard landing is usually seen as a daunting task by even the most experienced naval aviators. Shipboard vertical landing of VSTOL aircraft such as the AV-8B harrier have been known to be extremely dangerous due to the aircraft's inherent instabilities that prevail in hover flight conditions [1]. A testament to this is the large number of crashes of the Harrier that have occurred during shipboard approaches either due to pilot error or stability issues [2]. Automatic carrier landing systems play a pivotal role in mitigating such accidents arising from the pilot's physiological factors or flight dynamic instabilities. The precision approach landing system (PALS) employed by the US Navy is an automatic carrier landing system that is housed in the carrier, and provides guidance commands to approaching aircraft [3]. Currently, majority of the aircraft in the US Navy are capable of executing an all-weather automatic carrier landings by relying on PALS. The approaching aircraft couple their autopilots with the guidance signals issued by PALS to execute a fully automatic landing. The AV-8B Harrier, however, does not possess an automatic flight control system which (AFCS) permits automatic carrier landing. Therefore, in this thesis, an automatic carrier landing system (ACLS), comprising of an AFCS and

a guidance system will be developed for the AV-8B Harrier. Nuthi P. and Subbarao K. [4] develop a gain-scheduled AFCS and guidance laws for the AV-8B Harrier, and demonstrate autonomous vertical landing on a marine vessel. The authors define a flight envelope characterized by airspeed and altitude from which numerous trim points are selected. A linear quadratic regulator (LQR)-based inner and outer loop controllers are designed for each trim point with a view to provide stabilization, and track velocity and altitude reference commands that are computed using adaptive guidance laws. Since the controllers are only capable of tracking velocity and altitude, the applicability of this design is limited to straight-in carrier landings that do not require any lateral maneuvering. McMuldroch [5] addresses the shipboard vertical landing problem for lift-fan type VSTOL aircraft. The landing sequence is separated into two phases - hover and landing- and linear quadratic gaussian controllers are synthesized for either phases. While in hover, the controller ensures that the aircraft tracks the position and orientation of the flight deck, and the landing controller hovers smoothly to touchdown using minimum control effort. Deck motion prediction is included in the controller design which enhances the tracking performance of the controller. Hauser et. al. [6] design a feedback-linearized controller to stabilize the unstable roll dynamics of VSTOL aircraft in hover. A simplified 3 degree of freedom aircraft model is considered to explain roll instabilities and the associated limit cycles. Dynamic extension is performed until a model inversion is achieved following which a control law is synthesized to regulate roll angle to zero. Marconi et. al. [7] design an autonomous vertical landing system for a VTOL aircraft by considering planar dynamics of the aircraft. The objective is to land on a marine vessel which under the influence of sea-states, however the parameters that characterize the ship motion are assumed to be unknown. The controller is required to adapt itself with the ship motion to prevent negative vertical offsets and crashes. Denison N. [8] designs a

dynamic inversion-based automated carrier landing system for futuristic unmanned combat aerial vehicles (UCAV) by including the effects of winds, turbulences, and burble. Due to the stochastic nature of the problem, the performance of the system is evaluated using Monte-Carlo simulations. Fitzgerald P. [9] compares the performances of direct lift control, and thrust vectoring control applied to automatic carrier landing in the presence of turbulence. The navigation system provided a reference flight path, and also accounted for position corrections during touchdown.

1.1 Thesis Outline

The objective of this thesis is to simulate automatic vertical landing of AV-8B Harrier-like-V/STOL aircraft on an aircraft carrier using two different flight control techniques - linear, gain-scheduled control system, and $\mathcal{L}_1$ adaptive control. The aircraft is required to fly along a predefined, fully three-dimensional flight path prior to executing a vertical landing. Chapter 2 presents the aircraft and the carrier models employed in this thesis. A high fidelity, fully non-linear flight simulation model of the aircraft and a kinematic model of the carrier is considered. Gain-scheduled landing autopilot design is presented in chapter 3. A flight envelope characterized by the aircraft's velocity, altitude, and turn-rate is first defined within which numerous equilibrium points are selected. Trim data pertaining to each flight condition is extracted following which plant linear models are obtained. Linear quadratic integral (LQI) controllers are designed for each equilibrium point, and the controller parameters are scheduled. The chapter also investigates inter-mode coupling, and control cross-coupling, and presents a control decoupling technique. Chapter 4 presents the design of landing autopilots using $\mathcal{L}_1$ adaptive control. This control technique eliminates the need for a precomputed gain-database, unlike gain-scheduling. Proofs of stability for adaptation laws are presented, and the low-pass filter design is discussed

in detail. The chapter concludes with reference model selection, and control architecture. Guidance laws which facilitate in automatic landing are presented in chapter 5. Design procedures for obtaining velocity, altitude, and turn-rate reference commands are presented. Chapter 6 presents simulation results of automatic carrier landing that are performed using the gain-scheduled and the $\mathcal{L}_1$ adaptive autopilots.

CHAPTER 2

SIMULATION MODELS

2.1 Flight Dynamics Model

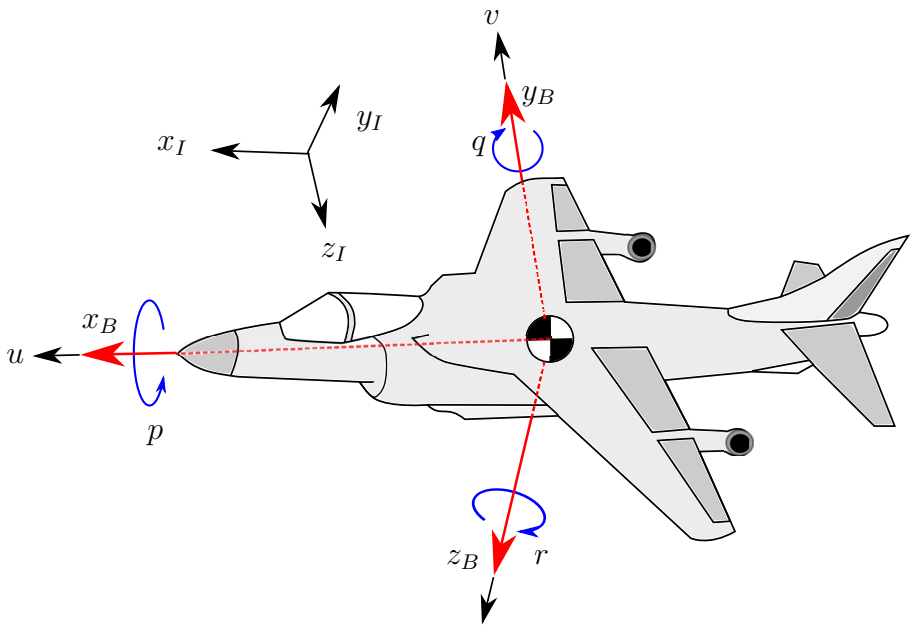

Figure 2.1: Reference Frames in the AV-8B Harrier Model

A high-fidelity, fully non-linear simulation model of the AV-8B Harrier is employed in this research. This simulation model was originally developed by the Department on Aerospace Engineering at Texas A&M University in collaboration with the United states Navy, and Engineering Systems Inc. [10]. The entire simulation, which was programmed in C++, was compiled to a C-Mex function by the authors in [4]. The origin of the body frame is fixed to the aircraft's center of gravity with the axes of the frame oriented in the usual directions - the x_B axis lies in the plane

of symmetry and points towards the nose, the y_B axis points to the right while being perpendicular to the plane of symmetry, and the z_B axis lies in the plane of symmetry and points downwards. The inertial frame is fixed to a point on the earth with its x_I axis pointing towards true North, y_I axis pointing towards East, and z_I axis pointing down while being mutually perpendicular to x_I and y_I axes. The orientation of the aircraft with respect to the inertial frame is parametrized in terms of 3-2-1 Euler angles - ϕ, θ, and ψ . Let $u,\ v,$ and w denote the components of the aircraft's velocity with respect to the inertial frame, represented on the body frame; $p,\ q$ and r denote the components of the aircraft's angular velocity represented on the body frame. The governing kinematic and dynamic equations of the aircraft motion presented in this section are based on [11], [12], and personal notes. The translational dynamics of the aircraft are governed by

$$\dot{u} = rv - qw + \frac{F_x}{m} - g\sin\theta \tag{2.1}$$

$$\dot{v} = pw - ru + \frac{F_y}{m} - g\cos\theta\sin\phi \tag{2.2}$$

$$\dot{w} = qu - pv + \frac{F_z}{m} - g\cos\theta\cos\phi \tag{2.3}$$

'm' denotes the aircraft's mass, and 'g' denotes acceleration due to gravity. F_x, F_y, and F_z denote the aerodynamic and thrust forces that are acting on the aircraft along the x_B, y_B, and z_B directions. The aircraft's rotational dynamics are given by

$$\dot{p}I_{xx} - \dot{q}I_{xy} - \dot{r}I_{xz} = L + pqI_{xz} - (r^2 - q^2)I_{yz} - qr(I_{zz} - I_{yy}) - prI_{xy} \tag{2.4}$$

$$\dot{q}I_{yy} - \dot{p}I_{xy} - \dot{r}I_{yz} = M - pr(I_{xx} - I_{zz}) - (p^2 - r^2)I_{xz} + qrI_{xy} - pqI_{yz} \tag{2.5}$$

$$\dot{r}I_{zz} - \dot{p}I_{xz} - \dot{q}I_{yz} = N - pq(I_{yy} - I_{xx}) - qrI_{xz} - (q^2 - p^2)I_{xy} + prI_{yz} \tag{2.6}$$

where, I_{xx}, I_{yy}, and I_{zz} represent the aircraft's principal moments of inertia, and I_{xy}, I_{yz}, and I_{xz} denote the aircraft's products of inertia. L, M, and N represent the

moments due to thrust and aerodynamics acting on the aircraft about the x_B, y_B, and z_B axes, respectively. In the presence of wind, the forces F_x, F_y, and F_z, and the moments L, M, and N depend on the relative velocity of the aircraft with respect to wind, which is determined as follows. Let $\boldsymbol{\mathcal{R}}_{BI}$ denote the rotation matrix from the inertial frame to the body frame, which is given by

$$\boldsymbol{\mathcal{R}}_{BI} = \begin{bmatrix} \cos\theta\cos\psi & \cos\theta\sin\psi & -\sin\theta \\ -\cos\theta\sin\psi + \sin\phi\sin\theta\cos\psi & \cos\phi\cos\psi + \sin\phi\sin\theta\sin\psi & \sin\phi\cos\theta \\ \sin\phi\sin\psi + \cos\phi\sin\theta\cos\psi & -\sin\phi\cos\psi + \cos\phi\sin\theta\sin\psi & \cos\phi\cos\theta \end{bmatrix} \tag{2.7}$$

Let $\mathbf{v}^B = [\ u\ v\ w\ ]^T$ be the representation of the aircraft's inertial velocity on the body frame, and $\mathbf{W} = [\ W_N\ W_E\ W_D\ ]^T$ denote the wind velocity vector represented on the inertial frame with W_N, W_E, and W_D denoting the North, East and down components of wind velocity. The relative velocity of the aircraft with respect to the surrounding air, expressed on the body frame, denoted by $\bar{\mathbf{v}}_B$ is given by

$$\bar{\mathbf{v}}^B = \mathbf{v}^B - \boldsymbol{\mathcal{R}}_{BI}\mathbf{W} \tag{2.8}$$

Let $\mathbf{U} = [\ \delta_S\ \delta_T\ \delta_N\ \delta_A\ \delta_R\ \delta_F]^T$ denote a vector constituting the control inputs available on the AV-8B Harrier model. δ_S is the longitudinal stick deflection, δ_T is the throttle, δ_N is the nozzle gimbal angle, δ_A is the aileron deflection, δ_R is the rudder deflection, and δ_F is the flaps setting. Let $\boldsymbol{\mathcal{W}} = [\ p\ q\ r]^T$ denote the aircraft's angular velocity vector with respect to the inertial frame expressed on the body frame. The forces arising due to aerodynamics and thrust in Eqs.(2.1) - (2.6) are non-linear functions of $\bar{\mathbf{v}}^B$, $\boldsymbol{\mathcal{W}}$, and $\mathbf{U}$, as shown in Eqs.(2.10) - (2.14). $\mathcal{X}$, $\mathcal{Y}$, $\mathcal{Z}$, $\mathcal{L}$, $\mathcal{M}$, and $\mathcal{N}$ represent the unknown non-linear functions contained in the AV-8B simulation model.

$$F_x = \mathcal{X}\left(\bar{\mathbf{v}}^B, \boldsymbol{\mathcal{W}}, \mathbf{U}\right) \tag{2.9}$$

$$F_x = \mathcal{Y}\left(\bar{\mathbf{v}}^B, \boldsymbol{\mathcal{W}}, \mathbf{U}\right) \tag{2.10}$$

$$F_x = \mathcal{Z}\left(\bar{\mathbf{v}}^B, \boldsymbol{\mathcal{W}}, \mathbf{U}\right) \tag{2.11}$$

$$L = \mathcal{L}\left(\bar{\mathbf{v}}^B, \boldsymbol{\mathcal{W}}, \mathbf{U}\right) \tag{2.12}$$

$$M = \mathcal{M}\left(\bar{\mathbf{v}}^B, \boldsymbol{\mathcal{W}}, \mathbf{U}\right) \tag{2.13}$$

$$N = \mathcal{N}\left(\bar{\mathbf{v}}^B, \boldsymbol{\mathcal{W}}, \mathbf{U}\right) \tag{2.14}$$

Let p_E and p_N denote the North and the East inertial position of the aircraft with with h being its altitude. The velocity of the aircraft expressed on the inertial frame, denoted by $\mathbf{v}^I$ can be obtained by transforming the body velocity components to inertial frame. It is to be noted that $\mathbf{v}^I = [\ \dot{p}_E\ \dot{p}_N - \dot{h}\ ]^T$. Therefore

$$\mathbf{v}^I = \boldsymbol{\mathcal{R}}_{BI}^T \mathbf{v}^B \tag{2.15}$$

Further,

$$\dot{p}_N = u\cos\theta\cos\psi + v(-\cos\phi\sin\psi + \sin\phi\sin\theta\cos\psi) \tag{2.16}$$

$$\begin{aligned}\dot{p}_E &= u\cos\theta\sin\psi + v(\cos\phi\cos\psi + \sin\phi\sin\theta\sin\psi) \\ &\quad + w(-sin\phi\cos\psi + \cos\phi\sin\theta\sin\psi)\end{aligned} \tag{2.17}$$

$$\dot{h} = u\sin\theta + v\sin\phi\cos\theta + w\cos\phi\cos\theta \tag{2.18}$$

The rotational kinematic equations are

$$\dot{\psi} = (q\sin\phi + r\cos\phi)\, sec\theta \tag{2.19}$$

$$\dot{\theta} = q\cos\theta - r\sin\phi \tag{2.20}$$

$$\dot{\phi} = p + q\sin\phi\tan\theta + r\cos\phi\tan\theta \tag{2.21}$$

Therefore the state variables that characterize the behavior of the aircraft in the simulation model are written in the form of a vector $\mathbf{X} \in \mathbb{R}^{12\times 1}$ which is given by $\mathbf{X} = [\, p_N\ p_E\ h\ \phi\ \theta\ \psi\ u\ v\ w\ p\ q\ r]^T$. p_N, p_E, and h are measured in ft; ϕ, θ, and ψ are measured in deg.; u, v and w are measured in ft/s; and p, q, r are measured in $deg./s$. The wind velocities, W_N, W_E, and W_D, are measured in ft/s. The control inputs δ_N, δ_A, δ_R, and δ_F are measured in $deg.$, while δ_S and δ_T are measured in percentage. A positive aileron deflection results in a positive roll rate, and a positive rudder deflection results in negative yaw rate. The longitudinal stick deflection corresponding to zero δ_S is 28%. Any value of $\delta_S > 28\%$ results in a positive pitch rate. The nozzle can swivel from a fully-upright position to 90°, and a downward deflection is considered positive. A reaction control system is also built into the model, and is automatically activated based on the nozzle setting. Table (2.1) shows the limits on each of the control effectors on the harrier model.

Table 2.1: Limits on Control inputs

Control Inputs	Limits
Stick δ_S	0 to 100 % (Stick Center - 28 %)
Throttle δ_T	0 to 100 %
Nozzle δ_N	0 - 90^o
Aileron δ_A	-25^o to +25^o
Rudder δ_N	-15^o to +15^o
Flaps δ_F	0^o to 60^o

The system of non-linear differential equations that govern the motion of the aircraft in Eqs.(2.1) -(2.6), (2.16)-(2.21), can be written as

$$\dot{\mathbf{X}} \;=\; \mathbf{F}\left(\mathbf{X}, \mathbf{U}, \mathbf{W}\right) \tag{2.22}$$

where $\mathbf{F}(\cdot) \in \mathbb{R}^{12}$ denotes a vector of non-linear algebraic equations involving $\mathbf{X}$, $\mathbf{U}$, and $\mathbf{W}$.

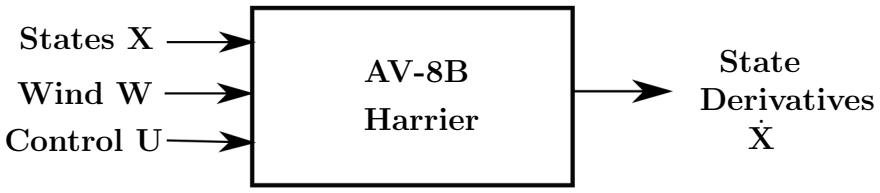

Figure 2.2: Schematic diagram of the AV-8B simulation model

2.2 Aircraft Carrier Model

The NAVAIR kinematic model of a Nimitz class carrier that is found in [8] is employed in this research. The landing spot is approximately 374 ft to the aft of C.G, and 22 ft towards the port side. The flight deck is angled at 9° to the longitudinal axis.

The ship's body frame is rigidly fixed to the hull at the C.G. with the x_S axis pointing towards the bow, the y_S axis pointing towards starboard, and the z_S axis pointing downwards. The orientation of the ship with respect to the inertial frame is parameterized using 3-2-1 Euler angles. The motion of the carrier is composed of a forward motion with constant velocity at zero pitch and roll angles, and perturbations caused due to sea states. The carrier is considered to have perturbations in heave, surge, sway, pitch and roll.

However, yaw perturbations are assumed to be zero. x_{ac}, y_{ac} are the inertial coordinates (North-East) of the carrier, V_{ac} is the velocity of the carrier, and ψ_{ac} denotes the heading of the carrier. ϕ_{ac}, θ_{ac}, and ψ_{ac} denote the roll, pitch, and yaw angles of the carrier. The mean forward motion of the ship is given by

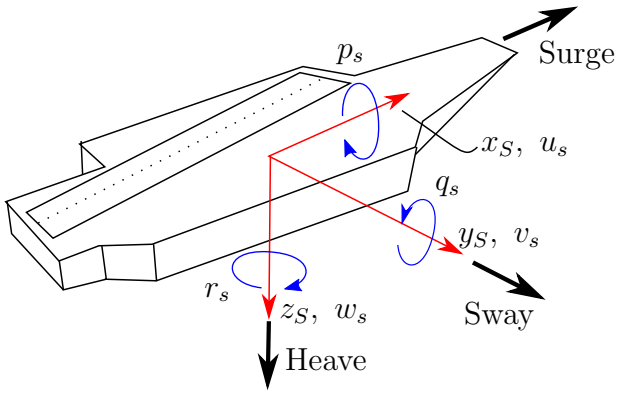

Figure 2.3: Notations used for the aircraft carrier

$$\dot{x}_{ac} = V_{ac} \cos \psi_{ac} \tag{2.23}$$

$$\dot{y}_{ac} = V_{ac} \sin \psi_{ac} \tag{2.24}$$

$$\dot{\psi}_{ac} = 0 \tag{2.25}$$

The translational perturbations acting on the C.G. of the ship are found using

$$\begin{bmatrix} \delta x_1 \\ \delta y_1 \\ \delta z_1 \end{bmatrix} = \begin{bmatrix} \cos \psi_{ac} & \sin \psi_{ac} & 0 \\ \sin \psi_{ac} & \cos \psi_{ac} & 0 \\ 0 & 0 & 1 \end{bmatrix} \begin{bmatrix} \delta u_{ac} \\ \delta v_{ac} \\ \delta w_{ac} \end{bmatrix} \tag{2.26}$$

where δu_{ac}, δv_{ac}, and δw_{ac} denote the surge, sway, and heave displacements, respectively, which are measured in feet.

The perturbations due to pitching and rolling are determined using

$$\begin{bmatrix} \delta x_2 \\ \delta y_2 \\ \delta z_2 \end{bmatrix} = \mathcal{R}_{IB}(\ \delta\phi_{ac},\ \delta\theta_{ac},\ \delta\psi_{ac}) \begin{bmatrix} -\Delta X_{CM} \\ -\Delta Y_{CM} \\ -\Delta Z_{CM} \end{bmatrix} \tag{2.27}$$

where $\mathcal{R}_{IB}(\cdot)$ represents the rotation matrix from the carrier's body frame to inertial frame; $\delta\phi_S$, $\delta\theta_S$, and $\delta\psi_S$ denote the sea-state perturbations in the carrier's bank, pitch, and yaw angles, respectively. ΔX_{CM}, ΔY_{CM}, and ΔZ_{CM} denote the separation between the landing point and the center of gravity of the carrier expressed on the carrier's body frame, and their respective values are -374 ft, -22 ft and -50 ft. The height of the carrier from the sea-level is assumed to be 70 ft. The total perturbation is obtained by summing up Eqs. (2.26) and (2.27) which is added to the mean forward motion in Eq.(2.25). A sea-state 4 perturbation model that is provided in [8] is considered in the simulation. The perturbations are modeled as sinusoidal waves using the information provided in table.(2.2)

Table 2.2: Sea-State 4 Perturbations

Perturbation	Amplitude	Frequency rad/s
Roll $\delta\phi_S$	0.6223 deg.	0.2856
Pitch $\delta\theta_S$	0.5162 deg.	0.5236
Yaw $\delta\psi_S$	0.0 deg.	0.0
Surge δu_{ac}	0.9546 ft.	0.3307
Sway δv_{ac}	1.4142 ft.	0.3307
Heave δw_{ac}	2.2274 ft.	0.3491

CHAPTER 3

GAIN-SCHEDULED CONTROLLER

The non-linear aircraft dynamics in Eq.(2.22)can be parametrized in terms of a vector of scheduling variables $\boldsymbol{\sigma} \in \mathbb{R}^3$ as

$$\dot{\mathbf{X}}(\boldsymbol{\sigma}) \;=\; \mathbf{F}\left(\mathbf{U}(\boldsymbol{\sigma}), \mathbf{X}(\boldsymbol{\sigma})\right) \tag{3.1}$$

where $\boldsymbol{\sigma} \;=\; [\;\; V_d \;\; \dot{\psi}_d \;\; h_d \;\;]^T$ with $V_d,\ \dot{\psi}_d,$ and h_d denoting the desired values of velocity, turn-rate, and altitude, respectively. Note that the wind term $\mathbf{W}$ has been dropped from Eq.(3.1), since the controller is developed assuming no winds. Let $\mathcal{S}$ denote a three dimensional, admissible convex sample space of $V_d,\ h_d$ and, $\dot{\psi}_d$, defined as

$$\mathcal{S} \;\triangleq\; \left\{\; \boldsymbol{\sigma} \in \mathbb{R}^3 \;:\; V_d \in [\;0 \;\; 500\;],\ \dot{\psi}_d \in [-10 \;\; 10\;],\ h_d \in [\;10 \;\; 1000\;] \;\right\}$$

The bounds on $V_d, \dot{\psi}_d$ and h_d are imposed based on the flight envelope considered for ACLS design. The equilibrium family for Eq.(3.1) defined on the set $\mathcal{S}$, represented by $(\mathbf{X}_0(\boldsymbol{\sigma}), \mathbf{U}_0(\boldsymbol{\sigma}))$ satisfies the relation

$$\dot{\mathbf{X}}_0(\boldsymbol{\sigma}) \;=\; \mathbf{F}\left(\mathbf{U}_0(\boldsymbol{\sigma}), \mathbf{X}_0(\boldsymbol{\sigma})\right) \tag{3.2}$$

where $\dot{\mathbf{X}}_0(\boldsymbol{\sigma})$ is the state derivative vector corresponding to zero steady-state error, which is given by $\dot{\mathbf{X}}_0(\boldsymbol{\sigma}) \;= [\dot{p}_N \;\; \dot{p}_E \;\; 0\;0\;0\;0\;0\;0\;0\;0\;0\;0\;]^T$ for steady, straight and level flight condition, and $\dot{\mathbf{X}}_0(\boldsymbol{\sigma}) \;=\; [\;\dot{p}_N \;\; \dot{p}_E \;\; 0\;0\;0 \;\; \dot{\psi}_d \;\; 0\;0\;0\;0\;0\;]^T$ for steady turning flight condition.

For both cases, the following constraint relations, $\dot{p}_N = V_d \cdot \cos\psi$, $\dot{p}_E = V_d \cdot \sin\psi$, and $\dot{\psi}_d = \text{sign}(\dot{\psi}_d)\sqrt{p^2+q^2+r^2}$, hold good. Note that the equilibrium pair $(\mathbf{X}_0, \mathbf{U}_0)$ are unknown for any given $\boldsymbol{\sigma}$, and are determined by the process of trimming. Discretizing the sample-space $\mathcal{S}$, which is a 3-dimensional box, produces a finite set of grid elements as illustrated in Fig.(3.1), and the associated grid points represent the desired operating points. The grid dimensions must be small enough

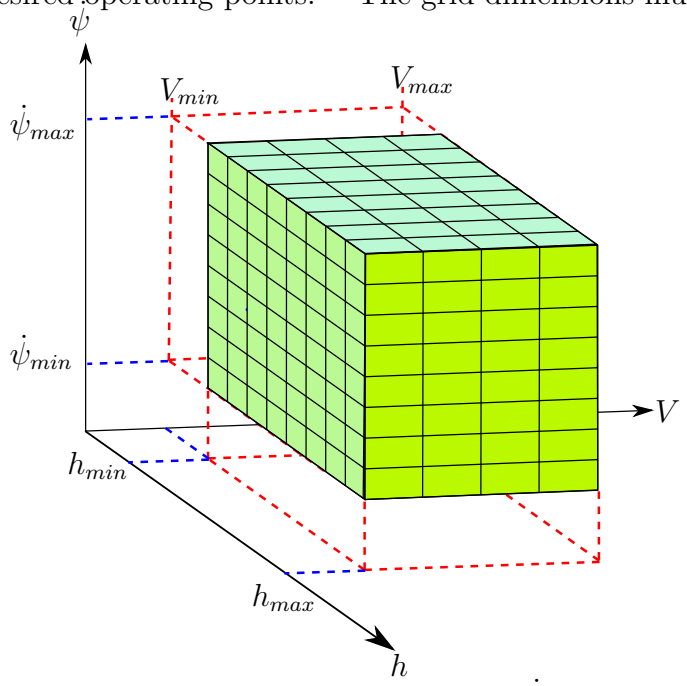

Figure 3.1: Illustration of discretized $V - \dot{\psi} - h$ sample-space

to capture the effect of non-linearities present in the aircraft's dynamics, and are selected purely based on engineering intuition since the non-linearities are unknown. The landing autopilot developed in [4] is scheduled on airspeed and altitude, and provided satisfactory performance with the corresponding sample steps being $20ft$ and $20ft/s$, respectively. However, decreasing the step sizes can enhance the controller's performance. In this research, step sizes of $5ft/s$ and $1°/s$ are conservatively chosen for V_d and $\dot{\psi}_d$, respectively. From the trim study performed in section 3.1, the equi-

librium pair $(\mathbf{X}_0(\boldsymbol{\sigma}), \mathbf{U}_0(\boldsymbol{\sigma}))$ is found to be highly sensitive to changes in altitude for $h_d \leq 100ft$. Therefore, an altitude step increment of 10 ft is chosen for $h_d < 100ft$. However, when $100ft \leq h_d \leq 1000ft$, the equilibrium pair varied more smoothly with h because of which an altitude step increment of $100ft$ is chosen in this range. Due to the conservativeness adopted in selecting the grid dimensions, the $V_d, \dot{\psi}_d$ and h_d axes of the sample-space $\mathcal{S}$ contain 101, 21, and 19 equilibrium points, respectively. Hence, discretization yields $101 \times 21 \times 19 \ = \ 40299$ trim points in total. The grid dimensions are summarized in the table below.

Table 3.1: Summary of sample-space mesh dimensions

Scheduling Variable	Range	Step size	No. of points
V_d	$0.1ft/s$ - $500.1ft/s$	$5ft/s$	101
h_d	$10ft$ - $100ft$ $100ft$ - $1000ft$	$10ft$ $100ft$	19
$\dot{\psi}_d$	$-\ 10°/s$ to $10°/s$	$1°/s$	21

3.1 Trim Database

Extraction of trim data is the most crucial stage is developing a gain-scheduled flight controller - the quality of trim data, and the variation of trim states and control inputs along the equilibrium trajectories in $\mathcal{S}$ govern the performance of the controller. The objective of trimming is to determine the equilibrium pair $(\mathbf{X}_0(\boldsymbol{\sigma}), \mathbf{U}_0(\boldsymbol{\sigma}))$ corresponding to every grid point in $\mathbf{S}$ by solving the set of non-linear differential equations in Eq.(3.2). However, the solution to the trim problem is non-unique as $\mathbf{F}(\cdot, \cdot, \cdot)$ is non-linear, and $\dim\{\mathbf{X}\}+\dim\{\mathbf{U}\} > \dim\{\boldsymbol{\sigma}\}$. Hence, the trim states and control in-

puts have to be estimated by specifying the desired upper and lower bounds, and this is made possible by resorting to constrained numerical optimization. First, an objective function $\mathcal{J}$ is defined with a motivation to perform seek for trim solution pertaining to both steady turning, and steady straight and level flight conditions, as follows.

$$\mathcal{J} \triangleq E_1 + E_2 + E_3 + \dot{\mathbf{e}}^T \dot{\mathbf{e}} \tag{3.3}$$

where,

$$\mathbf{e} = [h\ \phi\ \theta\ u\ v\ w\ p\ q\ r]^T \tag{3.4}$$

$$E_1 = (u^2 + w^2 - V_d^2)^2 \ + \ (\dot{p}_N^2 + \dot{p}_E^2 - V_d^2)^2 \tag{3.5}$$

$$E_2 = (h - h_d)^2 \tag{3.6}$$

$$E_3 = \left|\text{sign}(\dot{\psi}_d)\ \sqrt{p^2 + q^2 + r^2} - \dot{\psi}_d\right| + (\dot{\psi} - \dot{\psi}_d)^2 \tag{3.7}$$

The state-derivative terms in Eqs.(3.4)-(3.7) , $\dot{\mathbf{e}}$, $\dot{\psi}$, $\dot{p}_N$, and $\dot{p}_E$, are determined from Eq.(2.22) while holding $\mathbf{W} = [\ 0\ 0\ 0\ ]^T$. The rationale behind the definition of the objective function in Eq.(3.3) in explained as follows. Minimizing E_1 constrains the aircraft's velocity vector to the inertial $x_I - y_I$ plane, and to the aircraft's $x_B - z_B$ plane (plane of symmetry) which in turn causes the slip-velocity v, and the time derivative of altitude $\dot{h}$ to be zero. Minimizing E_2 trims the aircraft at the desired altitude, whereas minimizing E_3 ensures the aircraft's turn-rate equals the desired turn-rate. Finally, a steady flight condition is obtained by minimizing $\dot{\mathbf{e}}^T\dot{\mathbf{e}}$. Let ($\mathbf{X}_{min}$ $\mathbf{U}_{min}$) and ($\mathbf{X}_{max}$ $\mathbf{U}_{max}$) denote the desired upper and lower bounds on the equilibrium pair $(\mathbf{X}_0(\boldsymbol{\sigma}), \mathbf{U}_0(\boldsymbol{\sigma}))$. These bounds become the constraints on states and controls for the trim problem which is stated as :

$$\min_{\mathbf{X},\mathbf{U}} \ \mathcal{J} \ \text{ subject to the constraints } \ \mathbf{X} \in [\ \mathbf{X}_{min}\ \mathbf{X}_{max}\ ] \ \text{ and } \mathbf{U} \in [\ \mathbf{U}_{min}\ \mathbf{U}_{max}\ ]$$

This constrained minimization problem is initialized with an guess $\mathbf{X}_i \in [\ \mathbf{X}_{min}\ \mathbf{X}_{max}\ ]$ and $\mathbf{U}_i \in [\ \mathbf{U}_{min}\ \mathbf{U}_{max}\ ]$, and is solved iteratively until $(\mathbf{X}, \mathbf{U})$ converge to the unknown equilibrium pair $(\mathbf{X}_0(\boldsymbol{\sigma}), \mathbf{U}_0(\boldsymbol{\sigma}))$. The *fmincon* function available in MATLAB® was employed for solving the problem. The constraints $[\ \mathbf{X}_{min}\ \mathbf{X}_{max}\ ]$ and $[\ \mathbf{U}_{min}\ \mathbf{U}_{max}\ ]$ are carefully varied as a function of V_d and $\dot{\psi}_d$ to ensure fast, error-free convergence of the optimization problem.

3.1.1 Turn Coordination

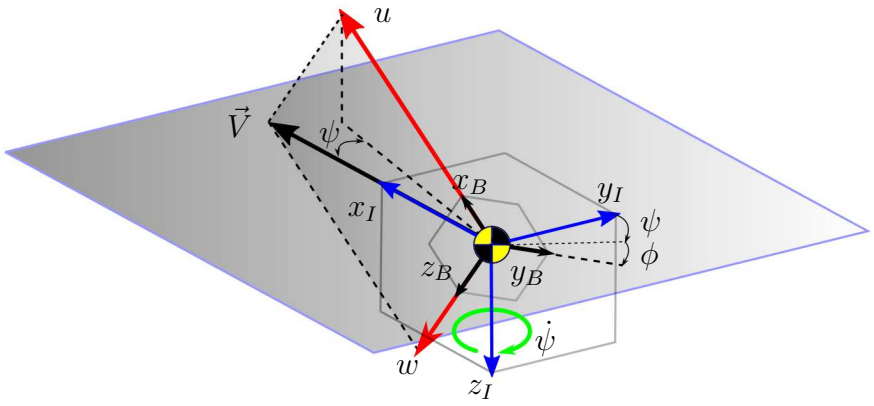

Figure 3.2: Illustration of constraints in steady turning flight condition

Coordinated turns are a direct consequence of minimizing the first constituent, E_1 of the objective function. Fig. (3.2) illustrates the steady turning flight condition at the instant when course $\chi = 0$. Besides reducing the aerodynamic drag, driving the slip velocity v to zero also ensures that the turns are coordinated, and this is elucidated using the aircraft's translational dynamics in y_B direction from Eq.(2.2)

$$a_{By} \;=\; g\,\sin\!\phi\,\cos\!\theta \;+\; \frac{1}{m}\,F_y \tag{3.8}$$

where, $a_{By} = \dot{v} - pw + ru$ denotes the component of the aircraft's inertial acceleration along the y_B axis. For turn coordination, it is essential that the inertial acceleration component a_{yB} must be parallel to the component of gravity along y_B, i.e., $a_{yB} = g \sin\phi \cos\theta$. From Eq.(3.8), this coordination condition is satisfied if the side-force $f_y = 0$. For symmetric aircraft, $v = 0$ implies $f_y = 0$, which is not the case for asymmetric aircraft. Though the AV-8B Harrier is not exactly known to be symmetric, $v = 0$ yields coordination. This is seen by computing the difference between a_{yB} and $g \sin\phi \cos\theta$, which is the lateral g-acceleration. Fig.(3.3) shows that the lateral g-acceleration is negligibly small for most flight conditions.

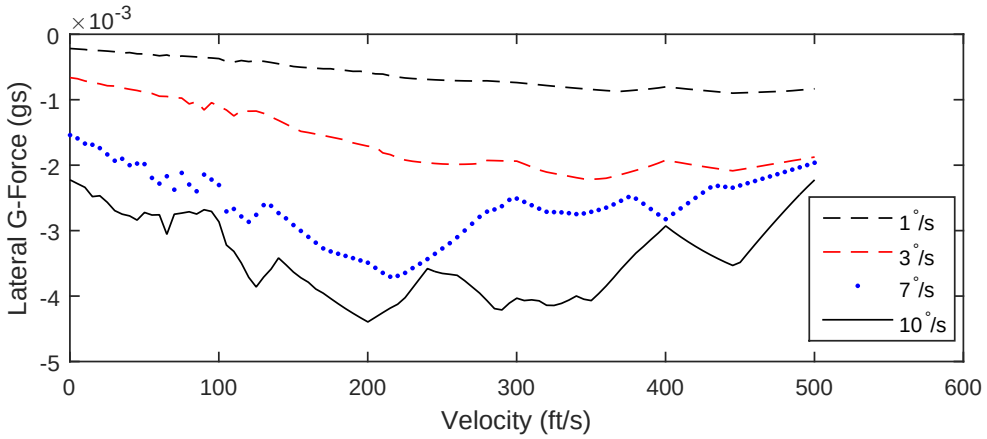

Figure 3.3: Variation of lateral g-acceleration with velocity for different turn-rates under trim conditions for steady turn.

3.1.2 Flap and Nozzle Schedules

For high speed flight conditions, it is essential to trim the aircraft by restricting the flap and nozzle deflections to zero to eliminate unrealistic trim attitudes. On the other hand, achieving a low-speed or a hovering flight condition is impossible without deploying flaps and nozzle. Considering these factors, the following schedul-

ing laws, that are based on the operating procedures mentioned in [13], are imposed as constraints in the trim optimization problem. The nozzle deflection δ_N has been scheduled with respect to airspeed to cause a smooth transition from high-speed, lift-supported flight to jet-borne flight, using the nozzle scheduling law given by

$$\delta_N = \begin{cases} 0 & \text{if } V > 400 ft/s \\ 0.35(400 - V) & \text{if } 200 ft/s \leq V \leq 400 ft/s \\ \text{Between } 70^\circ \text{ and } 90^\circ & \text{if } V < 200 ft/s \end{cases}$$

This nozzle scheduling law maintains a zero nozzle-deflection at high-speeds ($V > 400 ft/s$), and interpolates linearly between 0° and 70° as the velocity varies from $400 ft/s$ to $200 ft/s$. For low velocities ($V < 200 ft/s$), the nozzle deflection is not specified, but determined as a solution to the optimization problem between 70° and 90°.

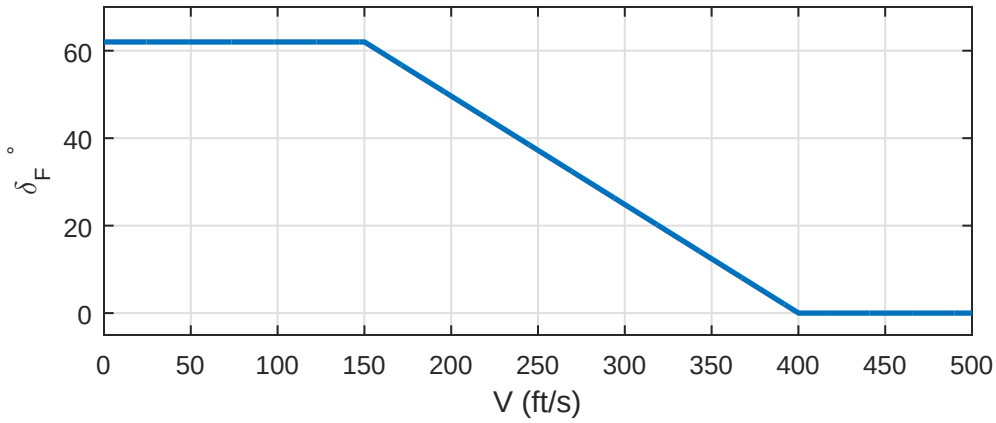

Figure 3.4: Flap Schedule

Similarly, the flap deflection is also scheduled with respect to airspeed as shown in Fig.(3.4) using the following flap scheduling law.

$$\delta_F = \begin{cases} 0 & \text{if } V > 400ft/s \\ 0.248(400 - V) & \text{if } 150ft/s \leq V \leq 400ft/s \\ 62^\circ & \text{if } V < 150ft/s \end{cases}$$

3.1.3 Trim Results

The trim states and control inputs, $\mathbf{X}_0$ and $\mathbf{U}_0$, that were determined for each of the 40299 points in $\mathcal{S}$ are stored in a three-dimensional array. Some trim results from the large data set of equilibrium points in are presented below.

- High speed, lift-supported turning flight

  $V = 500ft/s$, $\dot{\psi} = 10^\circ/\text{s}$, $h = 1000ft$

$$\begin{aligned} \mathbf{X}_0 &= [\ 0ft\ \ 0ft\ \ 1000ft\ \ 70.03^\circ\ \ 3.04^\circ\ \ 0^\circ\ 494.16ft/s\ \ 0ft/s\ .... \\ &\quad .... \ 76.87ft/s\ \ -0.53^\circ/s\ \ 9.39^\circ/s\ \ 3.41^\circ/s\ \ ]^T \\ \mathbf{U}_0 &= [\ \ 57.7\%\ \ 69.49\%\ \ 0^\circ\ \ -0.12^\circ\ \ -0.4^\circ\ \ 0^\circ\ \ ]^T \end{aligned}$$

- Low-speed, jet-borne straight and level flight

  $V = 100ft/s$, $\dot{\psi} = 0^\circ/\text{s}$, $h = 300ft$

$$\begin{aligned} \mathbf{X}_0 &= [\ \ 0ft\ \ 0ft\ \ 300ft\ \ 0^\circ\ \ 10.9^\circ\ \ 0^\circ\ \ 98.29ft/s\ \ 0ft/s\ .... \\ &\quad .... \ 18.93ft/s\ \ 0^\circ/s\ \ 0^\circ/s\ \ 0^\circ/s\ \ ]^T \\ \mathbf{U}_0 &= [\ \ 34.2\%\ \ 83.92\%\ \ 71.41^\circ\ \ 0^\circ\ \ 0^\circ\ \ 62^\circ\ \ ]^T \end{aligned}$$

- Turning at intermediate, transition speed

  $V = 300ft/s$, $\dot{\psi} = -10°/s$, $h = 600ft$

$$\begin{aligned}
\mathbf{X}_0 &= [\ 0ft\ \ 0ft\ \ 600ft\ \ -58.97°\ \ 5.32°\ \ 0°\ \ 295.32ft/s\ \ .... \\
&\qquad ....0ft/s\ \ 53.37ft/s\ \ 0.93°/s\ \ 8.53°/s\ \ -5.13°/s\ \ ]^T \\
\mathbf{U}_0 &= [\ 30.42\%\ \ 74.26\%\ \ 35°\ \ 0.22°\ \ 0.99°\ \ 24.8°\ \ ]^T
\end{aligned}$$

3.2 Linearization of the Equations of Motion

Linear models of the aircraft at every trim point in $\mathcal{S}$ are determined by jacobian-linearization of the governing equations of motion in Eq.(2.22), which is achieved by providing small perturbations to the corresponding trim states $\mathbf{X}_0(\boldsymbol{\sigma})$ and $\mathbf{U}_0(\boldsymbol{\sigma})$. The perturbed dynamics are given by

$$\dot{\mathbf{X}} = \mathbf{F}(\mathbf{U}_0 + \Delta\mathbf{U},\ \mathbf{X}_0 + \Delta\mathbf{X}) \tag{3.9}$$

Expressing the perturbed state derivative as $\dot{\mathbf{X}} = \dot{\mathbf{X}}_0 + \Delta\dot{\mathbf{X}}_0$, and expanding the right hand side of the above equation using Taylor series, we obtain,

$$\dot{\mathbf{X}}_0 + \Delta\dot{\mathbf{X}}_0 = \mathbf{F}(\mathbf{U}_0, \mathbf{X}_0) + \mathbf{A}\Delta\mathbf{X} + \mathbf{B}\Delta\mathbf{U} + H.O.T \tag{3.10}$$

where, $\mathbf{A} \in \mathbb{R}^{12\times12}$ and $\mathbf{B} \in \mathbb{R}^{12\times6}$ are the systems drift and control effectiveness matrix that are respectively given by

$$\mathbf{A} = \left.\frac{\partial\mathbf{F}}{\partial\mathbf{X}}\right|_{(\mathbf{X}_0,\mathbf{U}_0)} \text{ and } \mathbf{B} = \left.\frac{\partial\mathbf{F}}{\partial\mathbf{U}}\right|_{(\mathbf{X}_0,\mathbf{U}_0)}$$

H.O.T. denotes higher order terms whose contribution in the above equation is insignificant due to the perturbations being small.

Subtracting Eq.(3.2) from Eq.(3.9), yields the linearized dynamics of the aircraft, mentioned as follows.

$$\Delta\dot{\mathbf{X}} \;=\; \mathbf{A}\;\Delta\mathbf{X} + \mathbf{B}\Delta\mathbf{U} \tag{3.11}$$

u_0, v_0, and w_0 denote the body velocity components under trim conditions, and V_0 is the corresponding airspeed. The $\mathbf{A}$ and $\mathbf{B}$ matrices for all the trimmed flight conditions are determined in MATLAB® using the *Partial Differentiation Equation toolbox* by providing a perturbation of magnitude 10^{-6} to each element in the state and control input vectors. Following the linearization, it is important to determine the controllability of the aircraft within the flight envelope considered for AFCS design. The ranks of the controllability matrix $\boldsymbol{\mathcal{C}} = [\ \mathbf{B} \mid \mathbf{AB} \mid \mathbf{A}^2\mathbf{B} \mid .... \mid \mathbf{A}^{11}\mathbf{B}\ ]$ is 12 for all points in $\mathcal{S}$; $\text{rank}(\boldsymbol{\mathcal{C}}) = \dim(\mathbf{X})$ implies the system is completely controllable at all flight conditions.

3.2.1 Selection of Output Variables

The linearized dynamics will be used for designing a MIMO proportional-intergral controller with an view to drive the steady state errors in the velocity 'V', altitude 'h' and lateral velocity 'v' to zero. If $\Delta\mathbf{Y} \in \mathbb{R}^3$ is a vector of desired outputs given by $\Delta\mathbf{Y} \;=\; [\ \Delta V\ \Delta H\ \Delta v\ ]^T$, and $\mathbf{C} \in \mathbb{R}^{3\times 12}$ denotes the plant output matrix given by, then

$$\Delta\mathbf{Y} = \mathbf{C}\ \Delta\mathbf{X} \tag{3.12}$$

where,

$$\mathbf{C} \;=\; \begin{bmatrix} 0 & 0 & 0 & 0 & 0 & 0 & \frac{u_0}{V_0} & \frac{v_0}{V_0} & \frac{w_0}{V_0} & 0 & 0 & 0 \\ 0 & 0 & 1 & 0 & 0 & 0 & 0 & 0 & 0 & 0 & 0 & 0 \\ 0 & 0 & 0 & 0 & 0 & 0 & 0 & 1 & 0 & 0 & 0 & 0 \end{bmatrix} \tag{3.13}$$

3.3 Inter-mode Coupling

The conventional approach followed to design AFCS consists of first decoupling the linearized lateral and longitudinal aircraft dynamics followed by designing the corresponding feedback gains, separately. This decoupling prevents control interferences, which are the adverse effects of the lateral control inputs on longitudinal state variables, and vice-versa . However, if inter-mode coupling, which is the coupling between longitudinal and lateral modes, exists, the lateral and longitudinal dynamics cannot be separated . Therefore, prior to designing controllers, it is imperative to check for any inter-mode coupling to decide whether feedback gains are designed using decoupled linear models, or the full-state model. In this regard, a reduced order, permuted liner model of the AV-8B is considered as follows

$$\Delta\dot{\mathbf{x}} = \bar{\mathbf{A}}\Delta\mathbf{x} + \bar{\mathbf{B}}\Delta\mathbf{u} \tag{3.14}$$

$\Delta\mathbf{x} = [\ \Delta\mathbf{x}_{Lon}^T \quad \Delta\mathbf{x}_{Lat}^T\ ]^T$, where $\Delta\mathbf{x}_{Lon} \in \mathbb{R}^{4\times1}$ and $\Delta\mathbf{x}_{Lon} \in \mathbb{R}^{4\times1}$ are the longitudinal and lateral state vectors given by $\Delta\mathbf{x}_{Lon} = [\ \Delta\theta\ \Delta u\ \Delta w\ \Delta q\ ]^T$ and $\Delta\mathbf{x}_{Lat} = [\ \Delta\phi\ \Delta v\ \Delta p\ \Delta r\ ]^T$. The control vector $\Delta\mathbf{u} = [\ \Delta\mathbf{u}_{Lon}^T \quad \Delta\mathbf{u}_{Lat}^T\ ]^T$, where $\Delta\mathbf{u}_{Lon} \in \mathbb{R}^{2\times1}$ and $\Delta\mathbf{u}_{Lat} \in \mathbb{R}^{2\times1}$ are the longitudinal and lateral control input vectors that are respectively given by $\Delta\mathbf{u}_{Lon} = [\ \Delta\delta_S\ \Delta\delta_T\ ]^T$ and $\Delta\mathbf{u}_{Lat} = [\ \Delta\delta_A\ \Delta\delta_R\ ]^T$ The permuted drift and the control effectiveness matrices, $\bar{\mathbf{A}}$ and $\bar{\mathbf{B}}$, are partitioned to identify the coupling matrices as shown below.

$$\Delta\dot{\mathbf{x}} = \left[\begin{array}{c|c} \mathbf{A}_{Lon} & \mathbf{A}_{12} \\ \hline \mathbf{A}_{21} & \mathbf{A}_{Lat} \end{array}\right]\Delta\mathbf{x} + \left[\begin{array}{c|c} \mathbf{B}_{Lon} & \mathbf{B}_{12} \\ \hline \mathbf{B}_{21} & \mathbf{B}_{Lat} \end{array}\right]\Delta\mathbf{u} \tag{3.15}$$

The sub-matrices $\mathbf{A}_{12} \in \mathbb{R}^{4\times4}$ and $\mathbf{A}_{21} \in \mathbb{R}^{4\times4}$ represent coupling between the longitudinal and lateral states while $\mathbf{B}_{12} \in \mathbb{R}^{4\times2}$ and $\mathbf{B}_{21} \in \mathbb{R}^{4\times2}$ denote the coupling in respective control effectivenesses. $\mathbf{A}_{Lon} \in \mathbb{R}^{4\times4}$ and $\mathbf{A}_{Lat} \in \mathbb{R}^{4\times4}$ are the decoupled longitudinal and lateral drift matrices with the corresponding control effectiveness being $\mathbf{B}_{Lon} \in \mathbb{R}^{4\times2}$ and $\mathbf{B}_{Lat} \in \mathbb{R}^{4\times2}$, respectively . If $\mathbf{A}_{12} = \mathbf{A}_{21} = 0$ indicating the absence of inter-mode coupling, then Eq.(3.14) can be separated into longitudinal and lateral dynamics as shown below,

$$\Delta\dot{\mathbf{x}}_{Lon} = \bar{\mathbf{A}}_{Lon}\ \Delta\mathbf{x}_{Lon} + \bar{\mathbf{B}}_{Lon}\ \Delta\mathbf{u}_{Lon} \tag{3.16}$$

$$\Delta\dot{\mathbf{x}}_{Lat} = \bar{\mathbf{A}}_{Lat}\ \Delta\mathbf{x}_{Lat} + \bar{\mathbf{B}}_{Lat}\ \Delta\mathbf{u}_{Lat} \tag{3.17}$$

and the feedback gains can be designed separately. The procedure can be extended to cases when the coupling drift matrices are non-zero, however, a requisite is inter-mode coupling must be insignificant. The magnitudes of eigen vectors or eigen functions characterize inter-mode coupling. The modal transformation $\Delta\mathbf{x} = \boldsymbol{\mathcal{V}}\Delta\boldsymbol{\xi}$, with $\boldsymbol{\mathcal{V}} \in \mathbb{C}^{8\times8}$ representing the modal matrix of $\bar{\mathbf{A}}$, is substituted in Eq.(3.14) to yield

$$\Delta\dot{\boldsymbol{\xi}}(t) = \boldsymbol{\Lambda}\Delta\boldsymbol{\xi} + \boldsymbol{\mathcal{V}}^{-1}\bar{\mathbf{B}}\ \Delta\mathbf{u} \tag{3.18}$$

where $\boldsymbol{\Lambda} = \boldsymbol{\mathcal{V}}^{-1}\mathbf{A}\boldsymbol{\mathcal{V}}$ is the diagonal matrix of eigen values of $\bar{\mathbf{A}}$. The solution to Eq.(3.18) is given by

$$\Delta\boldsymbol{\xi}(t) = e^{\boldsymbol{\Lambda}(t-t_0)}\ \Delta\boldsymbol{\xi}\,(t_0) + \int_{t_0}^{t} e^{\boldsymbol{\Lambda}(t-\tau)}\ \boldsymbol{\mathcal{V}}^{-1}\ \bar{\mathbf{B}}\ \mathbf{u} \tag{3.19}$$

Transforming the above equation back to the actual states,

$$\Delta\mathbf{x}(t) = \boldsymbol{\mathcal{V}}\ e^{\boldsymbol{\Lambda}(t-t_0)}\ \boldsymbol{\mathcal{V}}^{-1}\Delta\mathbf{x}\,(t_0) + \int_{t_0}^{t} \boldsymbol{\mathcal{V}}\ e^{\boldsymbol{\Lambda}(t-\tau)}\ \boldsymbol{\mathcal{V}}^{-1}\ \bar{\mathbf{B}}\ \mathbf{u} \tag{3.20}$$

Eqs.(3.19) and Eq.(3.20) the mode shapes are governed by the eigen values and the eigen vectors of $\bar{\mathbf{A}}$, or alternatively the eigen functions $\boldsymbol{\mathcal{V}}\ e^{\mathbf{\Lambda}(t-t_0)}$. The relative degree of involvement of each state in a dynamic mode can rather be found by examining the magnitude of the elements in corresponding eigen vectors. To investigate the inter-mode coupling phenomenon, the $\bar{\mathbf{A}}$ matrix at a trimmed flight condition of $V = 500ft/s$, $h = 1000ft$, and $\dot{\psi} = 0°/s$ is first considered.

Table 3.2: Eigen values at $V = 500ft/s$, $h = 1000ft$, and $\dot{\psi} = 0°/s$

Mode	Eigen Value
Short Period	-0.826 ± i 3.96
Phugoid	-0.0019 ± i 0.08
Dutch Roll	-0.544 ± i 3.046
Roll Subsidence	-4.382
Spiral Divergence	0.013

$$\bar{\mathbf{A}} = \left[\begin{array}{cccc|cccc} 0 & 0 & 0 & 1 & 0 & 0 & 0 & 0 \\ -0.56 & -0.039 & 0.134 & -0.556 & 0 & 0 & 0 & 0 \\ -0.036 & -0.05 & -1.259 & 8.575 & 0 & 0 & 0 & 0 \\ 0 & 0.088 & -1.85 & -0.391 & 0 & -0.22 & 0 & 0 \\ \hline 0 & 0 & 0 & 0 & 0 & 0 & 1 & 0.064 \\ 0 & 0 & 0 & 0 & 0.56 & -0.326 & 0.557 & -8.684 \\ 0 & 0 & 0 & 0 & 0 & -1.712 & -4.448 & 2.043 \\ 0 & 0 & 0 & 0 & 0 & 0.92 & -0.303 & -0.681 \end{array}\right]$$

The coupling matrices $\bar{\mathbf{A}}_{12}$ and $\bar{\mathbf{A}}_{21}$ zeros due to which there is no inter-mode coupling. This is also verified by observing the magnitude of the eigen vectors of the dynamic modes.

Table 3.3: Magnitude of Eigen function at $h = 1000\ ft$, $V = 500.1\ ft/s$, and $\dot{\psi} = 0°/s$

State	Roll Subsidence	Short Period	Dutch Roll	Phugoid	Spiral Divergence
$\Delta\theta$	0	0.103	0.028	0.146	0.007
Δu	0	0.054	0.014	0.988	0.065
Δw	0.003	0.901	0.241	0.044	0.003
Δq	0.001	0.419	0.088	0.012	0
$\Delta\phi$	0.223	0	0.101	0	0.995
Δv	0.044	0	0.859	0	0.05
Δp	0.971	0	0.318	0	0.009
Δr	0.068	0	0.29	0	0.063

From table (3.3), the magnitudes of lateral states $\Delta\phi\ \Delta v\ \Delta p\ \Delta r$ present in short-period and phugoid modes are zero, whereas the relative magnitudes of longitudinal states $\Delta\theta\ \Delta u\ \Delta w\ \Delta q$ present in lateral modes - dutch roll, spiral divergence, and roll subsidence - are insignificant compared to that of the lateral states. This is a clear indication of the absence of any inter-mode coupling in steady straight and level flight condition. As the carrier landing sequence involves turns at high-bank angles, inter-mode coupling may exist at flight conditions involving high turn-rates. Therefore, the trimmed flight condition of $V = 500ft/s$, $h = 1000ft$, and $\dot{\psi} = 0°/s$ is now considered for analysis.

$$\bar{\mathbf{A}} = \left[\begin{array}{cccc|cccc} 0 & 0 & 0 & 0.341 & -0.174 & 0 & 0 & -0.94 \\ -0.561 & -0.031 & 0.087 & -1.342 & 0 & 0 & 0 & 0 \\ -0.01 & 0.003 & -1.468 & 8.483 & -0.527 & 0.009 & 0 & 0 \\ 0 & 0.072 & -0.873 & -0.403 & 0 & -0.441 & 0.056 & -0.003 \\ \hline 0.175 & 0 & 0 & 0.05 & 0 & 0 & 1 & 0.018 \\ -0.028 & -0.06 & -0.009 & 0 & 0.191 & -0.477 & 1.342 & -8.598 \\ 0 & -0.034 & 0.083 & -0.038 & 0 & -3.077 & -4.474 & 2.47 \\ 0 & 0.013 & -0.029 & 0.003 & 0 & 0.407 & -0.572 & -0.636 \end{array}\right]$$

Table 3.4: Eigen values at $V = 500ft/s$, $h = 1000ft$, and $\dot{\psi} = 10°/s$

Mode	Eigen Value
Short Period	1.06 ± i 2.73
Phugoid	-0.0016 ± i 0.18
Dutch Roll	-0.587 ± i 2.77
Roll Subsidence	-4.15
Spiral Divergence	-0.0189

Clearly, the off-diagonal sub-matrices, which are the attributes for inter-mode coupling, are non-zero. The implication is that the magnitude of the eigen vector $\boldsymbol{\mathcal{V}}$ has to be determined to ascertain the extent to which the coupling exists. From table (3.5), the existence of a strong inter-mode coupling is clearly evident; especially, the dutch-roll mode involves large perturbation in the longitudinal states Δq and Δw.

Table 3.5: Magnitude of Eigen Vectors at $h = 1000$ ft, $V = 500.1$ ft/s, and $\dot{\psi} = 10°/s$

State	Roll Subsidence	Short Period	Dutch Roll	Phugoid	Spiral Divergence
$\Delta\theta$	0.0261	0.041	0.0526	0.305	0.0494
Δu	5.47×10^{-4}	0.135	0.115	0.906	0.994
Δw	0.00494	0.912	0.799	0.09	0.0856
Δq	0.0129	0.299	0.272	0.00238	0.0172
$\Delta\phi$	0.233	0.042	0.102	0.279	0.0475
Δv	0.0216	0.185	0.411	0.0273	0.0219
Δp	0.96	0.14	0.281	0.00821	0.00694
Δr	0.154	0.0516	0.116	0.00997	0.00356

Therefore, inter-mode coupling, which is absent at the trimmed straight and level flight condition, manifests at the trimmed turning flight condition, and this trend is observed at all velocities and altitudes in $\mathcal{S}$. Though the gains of longitudinal and lateral controllers of the AFCS can be separately designed for trimmed straight and level flight conditions, full state linear models are necessary for designing gains for all other flight conditions. It is convenient to design a controller that retains the same structure at all flight conditions because of which full state linear models will be considered for designing the controllers.

3.4 Control Cross-Coupling

A major draw-back of employing full-state linear models for designing the gains of the autopilots is the control cross coupling. In this section, the relative control effectiveness method provided in [14] is used to assess the control influence that each

control effector possess over the flight dynamic modes. With the objective of this technique being synthesis of a relative control effectiveness matrix, the state equation in Eq.(3.14) is transformed to block diagonal form using the similarity transformation $\Delta\mathbf{x} = \mathbf{M}\,\Delta\mathbf{z}$ as

$$\Delta\dot{\mathbf{z}} = \tilde{\mathbf{\Lambda}}\Delta\mathbf{z} + \mathbf{M}^{-1}\bar{\mathbf{B}}\Delta\mathbf{u} \tag{3.21}$$

where, $\tilde{\mathbf{\Lambda}} = \mathbf{M}^{-1}\bar{\mathbf{A}}\mathbf{M}$ is the diagonal matrix of *real* eigen values. The similarity transformation matrix $\mathbf{M} \in \mathbb{R}^{8\times 8}$ is constructed as follows. The columns in $\mathbf{M}$ that correspond to real eigen values of $\bar{\mathbf{A}}$ are set equal to the respective eigen vectors found in $\boldsymbol{\mathcal{V}}$. For every complex conjugate eigen value pair of $\bar{\mathbf{A}}$, one column in $\mathbf{M}$ is set equal to the real part of the corresponding eigen vector, and the neighboring column is set equal to the imaginary part of one of the complex conjugate eigen vectors. Let $\mathbf{\Sigma} \in \mathbb{R}^{4\times 4}$ denote a diagonal matrix of control authorities of each input in $\Delta\mathbf{u}$ constructed using the limits given in Table (2.1) i.e. $\mathbf{\Sigma} = diag\,([\ 100\ 100\ 25\ 15\ ])$.

$$\Delta\mathbf{u} = \mathbf{\Sigma}\,\Delta\tilde{\mathbf{u}} \tag{3.22}$$

where $\Delta\tilde{\mathbf{u}}$ is the normalized input vector which has limits ± 1. Let $\mathbf{\Gamma} \in \mathbb{R}^{8\times 4}$ be the transformed control influence matrix given by $\mathbf{\Gamma} = \mathbf{M}^{-1}\,\bar{\mathbf{B}}\,\mathbf{\Sigma}$ using which Eq.(3.21) is written as

$$\Delta\dot{\mathbf{z}} = \tilde{\mathbf{\Lambda}}\Delta\mathbf{z} + \mathbf{\Gamma}\Delta\bar{\mathbf{u}} \tag{3.23}$$

Let γ_{ij} denote the element of $\mathbf{\Gamma}$ which corresponds to the i^{th} modal coordinate $\Delta\mathbf{z}$, and j^{th} control input $\Delta\tilde{\mathbf{u}}$. The relative control effectiveness of a j^{th} control input upon an i^{th} real mode is found by

$$c_{re} = \frac{|\gamma_{ij}|}{\sqrt{\sum_j (\gamma_{ij})^2}} \tag{3.24}$$

The relative control effectiveness of a j^{th} control input on a i^{th} and $(i+1)^{th}$ complex conjugate mode is determined as

$$c_{im} = \frac{\sqrt{(\gamma_{i,j})^2 + (\gamma_{i+1,j})^2}}{\sqrt{\sum_j \left[(\gamma_{i,j})^2 + (\gamma_{i+1,j})^2\right]}} \tag{3.25}$$

Using the above definitions, the relative control effectiveness matrix found for the steady, straight and level flight condition at V = 500 ft/s , $\dot{\psi} = 0°/s$ and h = 1000 ft is shown below.

$$\begin{array}{cccc} \delta_S & \delta_T & \delta_A & \delta_R \\ \left(\begin{array}{cccc} 0.9941 & 0.0571 & 0.06099 & 0.06963 \\ 0.96 & 0.2266 & 0.1544 & 0.05619 \\ 1.703 \cdot 10^{-11} & 3.764 \cdot 10^{-12} & 0.9977 & 0.06746 \\ 3.721 \cdot 10^{-9} & 1.545 \cdot 10^{-10} & 0.4112 & 0.9116 \\ 2.78 \cdot 10^{-10} & 2.54 \cdot 10^{-11} & 0.9998 & 0.01902 \end{array}\right) & \begin{array}{c} \text{Short Period} \\ \text{Phugoid} \\ \text{Roll Subsidence} \\ \text{Dutch Roll} \\ \text{Spiral Divergence} \end{array} \end{array} \tag{3.26}$$

The stick deflection principally influences short-period and phugoid modes while the throttle deflection affecting only the phugoid mode. The aileron deflection affects roll subsidence and spiral divergence modes while, rudder influences the dutch-roll mode. Therefore, control cross coupling is negligible at this condition. Now, consider the control effectiveness matrix at V = 500 ft/s , $\dot{\psi} = 10°/s$ and h = 1000 ft.

$$\begin{array}{cccc} \delta_S & \delta_T & \delta_A & \delta_R \\ \left(\begin{array}{cccc} 0.734 & 0.0604 & 0.555 & 0.387 \\ 0.0862 & 0.0179 & 0.975 & 0.206 \\ 0.00738 & 9.62 \cdot 10^{-4} & 1.0 & 0.0224 \\ 0.397 & 0.0302 & 0.747 & 0.533 \\ 0.0744 & 0.0504 & 0.976 & 0.199 \end{array}\right) & \begin{array}{c} \text{Short-Period} \\ \text{Phugoid} \\ \text{Roll Subsidence} \\ \text{Dutch Roll} \\ \text{Spiral Divergence} \end{array} \end{array} \tag{3.27}$$

At this turning flight condition, there is a clear existence of control cross-coupling is clearly evident - the stick deflection injects energy into the dutch-roll mode and the aileron deflection injects energy into short period mode. For instance, if feedback gains are computed using the full state linear models, then perturbations in lateral state variables - v and r - will result in stick deflection in turn causing undesired pitching motion. Therefore, prior to synthesizing feedback gains, control decoupling is essential.

3.5 Control Decoupling

Numerous control decoupling and allocation schemes exist for systems with redundant control effectors [15], all of which solve an optimization problem to synthesize a mixing matrix which effectively reduce them to elevator, aileron, and rudder. For aircraft with non-redundant controls, such as the AV-8B, [16] proposes synthesizing an auxiliary control vector by partial inversion of the control variable matrix, $\bar{\mathbf{B}}$. Equivalently, decoupling can also be achieved by setting the elements of $\bar{\mathbf{B}}$ that correspond to undesired control coupling, to zero. Therefore, if b_{ij} represents an element in the '$\mathbf{B}$' matrix which corresponds to state 'i' and control input 'j', the following elements – $b_{p\delta_S}$, $b_{v\delta_S}$, $b_{r\delta_S}$, $b_{p\delta_T}$, $b_{v\delta_T}$, $b_{r\delta_T}$, $b_{u\delta_A}$, $b_{w\delta_A}$, $b_{q\delta_A}$,$b_{u\delta_R}$, $b_{w\delta_R}$, $b_{q\delta_R}$ – are set to zero. It is to be noted that this decoupling scheme will not minimize the undesired coupling between control effectors and principal modes, however, adverse feedback control signals can be minimized.

3.6 Linear Quadratic Tracking Control

The control objective of the automatic flight control system is to track the reference commands of velocity V, altitude h and slip velocity v. Besides augmenting

the stability and tracking the reference states, the controller should also ensure that the steady-state tracking error is driven to zero. These control requirements can be satisfied by employing, infinite horizon Linear Quadratic Integral (LQI), a multi-variable optimal tracking controller whose formulation is done as follows. Consider the following reduced order linear model of the AV-8B Harrier

$$\begin{aligned} \Delta\dot{\mathbf{X}}_g &= \mathbf{A}_g\Delta\mathbf{X}_g + \mathbf{B}_g\Delta\mathbf{U}_g \\ \Delta\mathbf{Y} &= \mathbf{C}_g\mathbf{X}_g \end{aligned} \tag{3.28}$$

$\Delta\mathbf{X}_g = [\ \Delta h\ \Delta\phi\ \Delta\theta\ \Delta\psi\ \Delta u\ \Delta v\ \Delta w\ \Delta p\ \Delta q\ \Delta r\ ]^T$ and $\Delta\mathbf{U}_g = [\ \Delta\delta_S\ \Delta\delta_T\ \Delta\delta_A\ \Delta\delta_R\ ]^T$, $\mathbf{A}_g \in \mathbb{R}^{10\times10}$, and $\mathbf{B}_g \in \mathbb{R}^{10\times4}$. $\Delta\mathbf{Y} = [\Delta V\ \Delta h\ \Delta v]^T$ is the output vector with $\mathbf{C}$ being the output matrix obtained by eliminating the first two columns from $\mathbf{C}$ in Eq.(3.13). The flap and nozzle deflections, δ_F and δ_N, are not used for controller design, and are restricted to their trim values. Let $\Delta\mathbf{r}_c \in \mathbb{R}^{3\times1}$ denote the commanded reference signal that are determined using a guidance system given by $\Delta\mathbf{r}_c = [\Delta V_c\ \Delta h_c\ \Delta v_c]^T$. The tracking error is $\boldsymbol{\zeta} = \Delta\mathbf{r}_c - \Delta\mathbf{Y}$. The LQI formulation assumes $\Delta\mathbf{r}_c$ to be a constant signal because of which

$$\dot{\boldsymbol{\zeta}} = -\ \Delta\dot{\mathbf{Y}} = -\ \mathbf{C}_g\Delta\dot{\mathbf{X}}_g \tag{3.29}$$

Taking the derivative of Eq.(3.29), and augmenting the state-space using Eq. (3.29)

$$\Delta\dot{\tilde{\mathbf{X}}}_g = \tilde{\mathbf{A}}_g\Delta\tilde{\mathbf{X}}_g + \tilde{\mathbf{B}}_g\Delta\dot{\mathbf{U}}_g \tag{3.30}$$

where $\Delta\tilde{\mathbf{X}}_g \in \mathbb{R}^{13\times1}$ is the augmented state vector given by $\Delta\tilde{\mathbf{X}}_g = [\Delta\dot{\mathbf{X}}_g\ \zeta]^T$ and

$$\tilde{\mathbf{A}}_g = \left[\begin{array}{c|c} \mathbf{A}_g & [0]_{10\times3} \\ \hline \mathbf{C}_g & [0]_{3\times3} \end{array}\right] \quad \tilde{\mathbf{B}}_g = \left[\begin{array}{c} \mathbf{B}_g \\ \hline [0]_{4\times3} \end{array}\right] \tag{3.31}$$

The scalar objective function chosen to determine optimal feedback gains is

$$J \;=\; \frac{1}{2}\int_0^\infty \Big(\Delta\tilde{\mathbf{X}}_g^T(\tau)\;\mathbf{Q}\;\Delta\tilde{\mathbf{X}}_g(\tau) + \Delta\dot{\mathbf{U}}_g^T(\tau)\;\mathbf{R}\;\Delta\dot{\mathbf{U}}_g(\tau)\;\Big)\,d\tau \tag{3.32}$$

subject to the constraints in equation (3.30). $\mathbf{Q} \in \mathbb{R}^{13\times 13}$ is the positive semi-definite state weighting matrix, and $\mathbf{R} \in \mathbb{R}^{4\times 4}$ is the positive definite control weighting matrix. The linear quadratic optimal controller is found using the relation

$$\Delta\dot{\mathbf{U}}_g \;=\; -\;\mathbf{R}^{-1}\;\tilde{\mathbf{B}}_g^T\;\mathbf{S}\;\Delta\tilde{\mathbf{X}}_g \tag{3.33}$$

where, $\mathbf{S}$ is determined as a solution to the following algebraic Riccati equation

$$\mathbf{S}\;\tilde{\mathbf{A}}_g \;+\; \tilde{\mathbf{A}}_g^T\;\mathbf{S} \;-\; \mathbf{S}\;\tilde{\mathbf{B}}_g\;\mathbf{R}^{-1}\;\tilde{\mathbf{B}}_g^T\;\mathbf{S} \;+\; \mathbf{Q} \;=\; 0 \tag{3.34}$$

Let $\mathbf{K}_g \in \mathbb{R}^{4\times 13}$ be the feedback gain matrix given by $\mathbf{K}_g \;=\; \mathbf{R}^{-1}\;\tilde{\mathbf{B}}_g^T\;\mathbf{S}$, which is separated into a gain $\mathbf{K} \in \mathbb{R}^{4\times 10}$ which is associated with the state vector $\Delta\mathbf{X}_g$, and a gain $\mathbf{K}_I \in \mathbb{R}^{4\times 3}$ which multiplies the tracking error $\boldsymbol{\zeta}$, i.e. $\mathbf{K}_g \;=\; [\,\mathbf{K} \mid \mathbf{K}_I]$. Therefore, Eq.(3.33) is expressed in terms of the decoupled gains is

$$\Delta\dot{\mathbf{U}}_g \;=\; -\;\mathbf{K}\;\Delta\dot{\mathbf{X}}_g \;-\; \mathbf{K}_I\;\boldsymbol{\zeta} \tag{3.35}$$

If $\mathbf{X}_{g0}$ and $\mathbf{U}_{g0}$ are the augmented state and control vectors corresponding to a trimmed flight condition, then

$$\Delta\mathbf{X}_g \;=\; \mathbf{X}_g \;-\; \mathbf{X}_{g0} \tag{3.36}$$

$$\Delta\mathbf{U}_g \;=\; \mathbf{U}_g \;-\; \mathbf{U}_{g0} \tag{3.37}$$

where $\mathbf{X}_g$ is the actual or the perturbed state, and $\mathbf{U}_g$ is actual control input. Integrating Eq.(3.35), and using the relations in Eqs.(3.37) and (3.37), the control law obtained is

$$\mathbf{U}_g \;=\; \mathbf{U}_{g0} - \mathbf{K}\;\left(\mathbf{X}_g - \mathbf{X}_{g0}\right) - \mathbf{K}_I \int_0^t \left(\Delta\mathbf{r}_c\left(\tau\right) - \Delta\mathbf{Y}\left(\tau\right)\right) d\tau \tag{3.38}$$

However, $\Delta\mathbf{r}_c$ is an incremental reference command provided to the controller about a trimmed flight condition which can be expressed as

$$\Delta\mathbf{r}_c \;=\; \mathbf{r}_c \;-\; \mathbf{r}_{c0} \tag{3.39}$$

$$\Delta\mathbf{Y} \;=\; \mathbf{C}_g\;\left(\mathbf{X}_g \;-\; \mathbf{X}_{g0}\right) \tag{3.40}$$

$\mathbf{r}_c = [\; V_c \; h_c \; v_c \;]^T$ is the absolute value of the reference command, with $\mathbf{r}_{c0} = [\; V_0 \; h_0 \; v_0 \;]^T$ corresponding to that at the trim conditions. Consequently, $\mathbf{r}_{c0} \;=\; \mathbf{C}_g\;\mathbf{X}_{g0}$ which on substituting to Eq.(3.39), and subtracting the result from Eq.(3.40) yields $\Delta\mathbf{r}_c - \Delta\mathbf{Y} = \mathbf{r}_c - \mathbf{Y}$. Hence the control law in Eq.(3.38) becomes

$$\mathbf{U}_g \;=\; \mathbf{U}_{g0} - \mathbf{K}\;\left(\mathbf{X}_g - \mathbf{X}_{g0}\right) - \mathbf{K}_I \int_0^t \left(\mathbf{r}_c\left(\tau\right) - \mathbf{Y}\left(\tau\right)\right) d\tau \tag{3.41}$$

Eq.(3.38) is the control law that is used for simulating automatic landing. The augmented trim states and controls, $\mathbf{X}_{g0}$ and $\mathbf{U}_{g0}$, are determined by employing scheduling laws that are discussed in 3.7. The gains $\mathbf{K}$ and $\mathbf{K}_I$ are determined using LQI command in MATLAB® by supplying the state and control weighting matrices, $\mathbf{Q}$ and $\mathbf{R}$, along with the system matrices $\mathbf{A}_g$, $\mathbf{B}_g$, and $\mathbf{C}_g$. The $\mathbf{Q}$ and $\mathbf{R}$ matrices are chosen as diagonal matrices for convenience, and the weights are turned to obtain the desired performance. Using this approach, the gains were determined for all the trim points in $\mathcal{S}$.

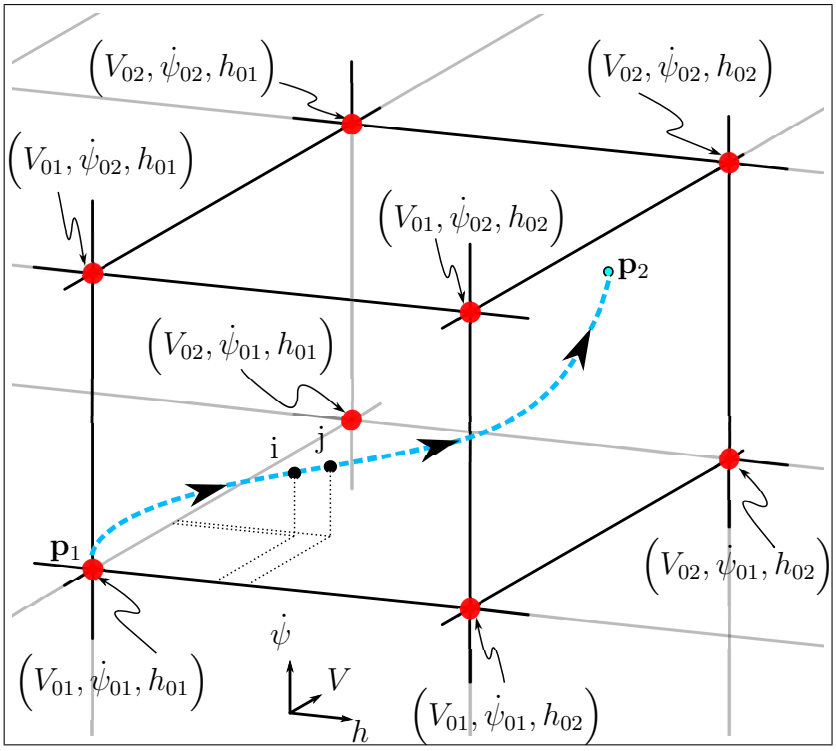

Figure 3.5: A single grid in sample space $\mathcal{S}$

The previous sections dealt with determining the trim states and controls, and the controller gains at every grid point in $\mathcal{S}$ using the corresponding plant linearizations. The control law in Eq.(3.38) is only locally valid at a trim point $(\mathbf{X}_0,\ \mathbf{U}_0)$ or alternatively $(\mathbf{X}_{g0}\ , \mathbf{U}_{g0})$. Therefore, a scheduling technique needs to be devised to render the locally valid control law for global, non-linear control. Fig.(3.5) shows a grid element in $\mathcal{S}$ which is lower bounded by the scheduling variables $\left(V_{01},\ \dot{\psi}_{01},\ h_{01}\right)$ and upper bounded by $\left(V_{02},\ \dot{\psi}_{02},\ h_{02}\right)$. Consider the aircraft to be in a trim point

'i' characterized the scheduling variables $\left(V_{0i},\ \dot{\psi}_{0i},\ h_{0i}\right)$, and trim values $\mathbf{U}_{g0i}$, $\mathbf{X}_{g0i}$, $\mathbf{K}_i$, and $\mathbf{K}_{Ii}$. The control law at this point is given by

$$\mathbf{U}_{gi} \ = \ \mathbf{U}_{g0i} - \mathbf{K}_i \ \left(\mathbf{X}_{gi} - \mathbf{X}_{g0i}\right) - \mathbf{K}_{Ii} \int_0^t \left(\mathbf{r}_{ci}\left(\tau\right) - \mathbf{Y}_i\left(\tau\right)\right) d\tau \tag{3.42}$$

where $\mathbf{r}_{ci} \ = \ \left[\ V_{ci}\ h_{ci}\ v_{ci}\right]^T$ and $\mathbf{Y}_i \ = \ \left[\ V_i\ H_i\ v_i\right]^T$ are commanded reference signal, and plant output respectively at the trim point 'i'. This control law stabilizes the aircraft about the flight condition 'i' facilitating in tracking the reference commands of airspeed altitude and slip velocity. Let 'j' be a trim point that is present in the immediate vicinity of 'i'. Suppose it is desired to transit from 'i' to 'j', the trim states, controls and gains are changed to those found at 'j' such that Eq.(3.42) becomes

$$\mathbf{U}_{gj} \ = \ \mathbf{U}_{g0j} - \mathbf{K}_j \ \left(\mathbf{X}_{gj} - \mathbf{X}_{g0i}\right) - \mathbf{K}_{Ij} \int_0^t \left(\mathbf{r}_{cj}\left(\tau\right) - \mathbf{Y}_i\left(\tau\right)\right) d\tau \tag{3.43}$$

Since, the asymptotic properties of LQI control law in Eq.(3.43) are valid at 'i', the flight condition that is initially at 'i' smoothly transitions to 'j'. This process of transitioning to a neighboring trim point is repeated until the aircraft reaches the desired flight condition in $\mathcal{S}$. This is illustrated in Fig.(3.5) where scheduling is performed within the grid, in order to transit from a flight condition p_1 to p_2 along a smooth equilibrium trajectory. It is to be noted that the trim states and controls,$\mathbf{X}_{g0}$ and $\mathbf{U}_{g0}$, and gains $\mathbf{K}$ and $\mathbf{K_I}$ are known only at the vertices/ grid points of the grid element. Therefore, for all other points, in $\mathcal{S}$, $\mathbf{X}_{g0}$, $\mathbf{U}_{g0}$, $\mathbf{K}$, $\mathbf{K_I}$ are determined using trilinear interpolation scheme.

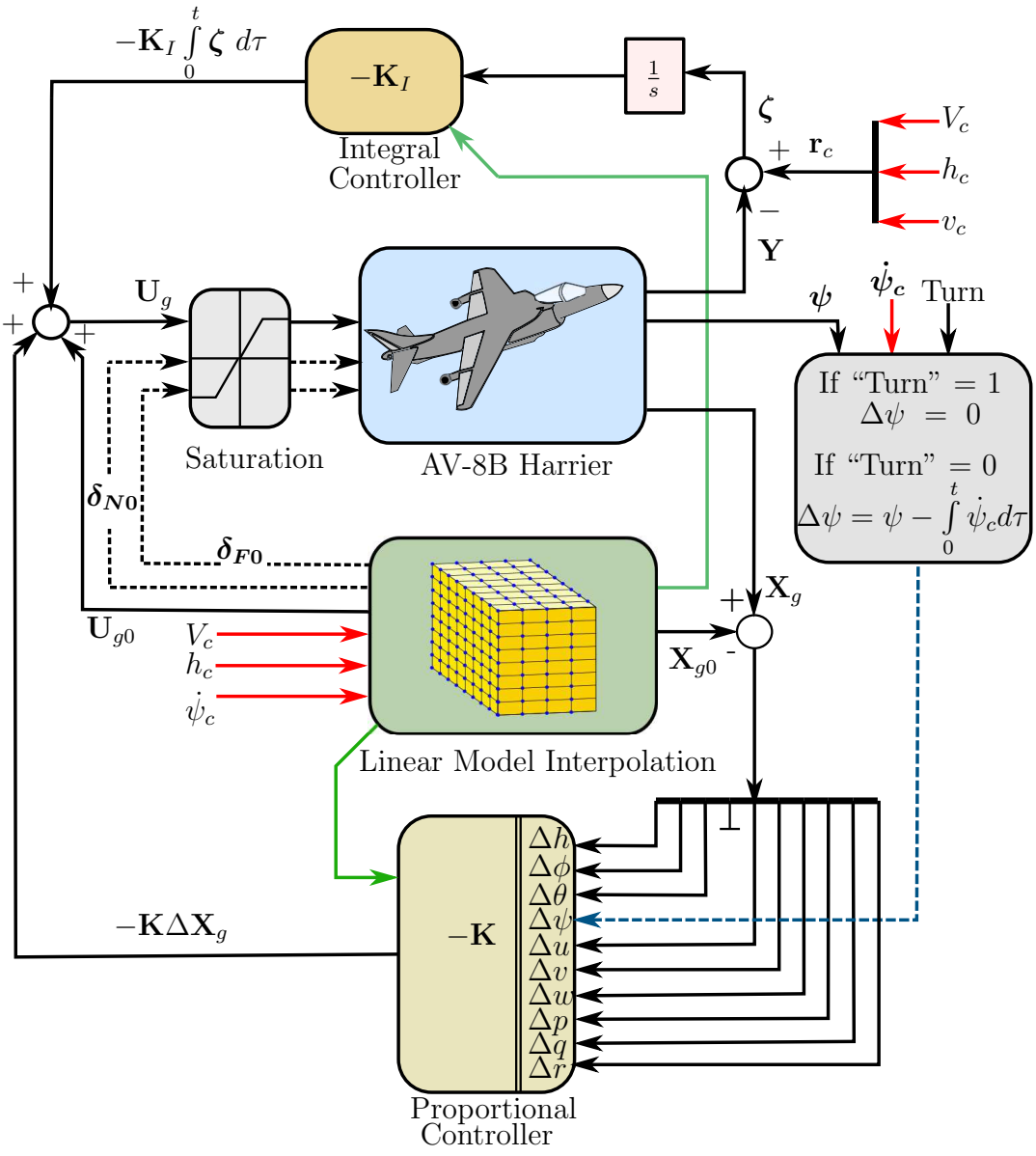

Figure 3.6: Implementation of gain-scheduled flight control laws

The implementation of the flight control law in Eq.(3.41) is illustrated in Fig.(3.6). The scheduling variables $\boldsymbol{\sigma}_c = \left[V_c \ \dot{\psi}_c \ h_c \right]^T$, and the commanded reference signal $\mathbf{r}_c = [\ V_c \ h_c \ v_c\ ]^T$ are provided as inputs to the gain-scheduled control system, and are indicated by the red arrows. Both the scheduling variables and the reference commands are determined using the guidance laws, which have been discussed in chapter 5, based on relative position of the aircraft with respect to the carrier. Interpolated values of the trim state vector $\mathbf{X}_{g0} = [\ h_0\ \phi_0\ \theta_0\ \psi_0\ u_0\ v_0\ w_0\ p_0\ q_0\ r_0\ ]^T$, trim control vector $\mathbf{U}_{g0} = [\delta_{S0}\ \delta_{T0}\ \delta_{A0}\ \delta_{R0}\ ]^T$, trim nozzle and flap deflections δ_{N0} and δ_{F0}, respectively, and the gains $\mathbf{K}$ and $\mathbf{K}_I$ are calculated by the block labeled "linear model interpolation" for the specified scheduling signal. These interpolated quantities are used for synthesizing the control input $\mathbf{U}_g$ using the control law in Eq.(3.41), which along with δ_{N0} and δ_{F0} are supplied to the aircraft through a saturation block which serves to restrict the input signals to their limits specified in table(2.1).

Extraction of the trim data in section 3.1 was performed by restricting the heading angle to zero for all points in $\mathcal{S}$. As a result, the trim state vectors contain zeros for the heading angle because of which the proportional feedback of the heading error signal $\Delta\psi = \psi - \psi_0$ stabilizes the aircraft about the heading angle of 0°, thus not permitting the aircraft to turn or stabilize about other heading angles. To overcome this issue, a logic variable "turn" is defined to determine whether heading angle feedback is to be provided or not, using which $\Delta\psi$ is determined as follows

$$\Delta\psi = \begin{cases} \psi - \int_0^t \dot{\psi}(\tau)d\tau & \text{if turn} = 0 \\ 0 & \text{if turn} = 1 \end{cases}$$

The value of the logic variable is set by the guidance laws. For turning maneuvers involving large turn-rates and large heading angle changes, "turn" is set to 1 which in turn eliminates the undesired heading error feedback signal by selecting $\Delta\psi = 0$. For straight and level flights where it is necessary to stabilize the aircraft about the desired heading angle, "turn" is set to 0, thereby choosing the heading error feedback to be $\Delta\psi = \psi - \int_0^t \dot{\psi}_c(\tau)d\tau$. The integral term $\int_0^t \dot{\psi}_c(\tau)d\tau$ represents the commanded heading angle, because of which the heading error feedback results in the aircraft's heading angle ψ asymptotically tracking the commanded heading angle ψ_c .

CHAPTER 4

$\mathcal{L}_1$ ADAPTIVE CONTROLLER

4.1 Introduction

Ever since the advent of high performance aircraft, there has been a great deal of interest in designing flight control systems (FCS) whose parameters adapt to varying conditions of flight, and uncertainties. Adaptive control, unlike gain-scheduling, do not require an extensive, precomputed database of controller parameters, and their global stability and performance can be guaranteed by resorting to Lyapunov stability theory. One of the most widely researched adaptive control techniques is model reference adaptive control (MRAC). Here, the control objective is to ensure that the aircraft replicates the behavior of a specified reference model, even in the presence of uncertainties. MRAC augmentation of gain-scheduled flight control systems have been explored using multiple reference models in [17], and for guidance of munition in [18]. However, [19] and [20] show that MRAC subjected to large uncertainties during transients lead to unbounded control signals, large transient tracking errors, and slow parameter convergence rates. Moreover, the adaptation rate is shown to set a trade-off between performance and robustness - fast adaptation improves tracking performance, but at the cost of phase margin. These key drawbacks of the highly potent MRAC scheme led to the development of the $\mathcal{L}_1$ adaptive control theory. The architecture of $\mathcal{L}_1$ adaptive control guarantees performance and robustness even in the presence of fast adaptation. Essentially, the adaptation loop is decoupled from the feedback loop by employing a low-pass filter which ensures that the control signals are confined to the low frequency range. The capabilities of the $\mathcal{L}_1$ adaptive control

have been substantiated with the help of a large number of flight tests of NASA's generic transport model [21]. $\mathcal{L}_1$ controllers have also been successfully tested on a number of UAVs in [22], [23],[24], and [25]. Numerous simulation studies performed in [27], [28], and [26] also corroborate the benefits of using $\mathcal{L}_1$ adaptive controllers. In this chapter, an $\mathcal{L}_1$ adaptive tracking controller is designed for the AV-8B Harrier by considering full state feedback. The design is based on the fundamental principles of the $\mathcal{L}_1$ adaptive control theory provided in [20].

4.2 Mathematical Preliminaries

4.2.1 Norms of Vectors and Matrices

Consider a vector $\mathbf{y} \in \mathbb{R}^m$ and a matrix $\mathbf{A} \in \mathbb{R}^{n\times m}$. If $||y||_p$ and $||A||_p$ denote p-norms of the vector $\mathbf{y}$ and $\mathbf{A}$, respectively, then the norm definitions are as follows.

$$||\mathbf{y}||_1 = \sum_{i=1}^{m} |\mathbf{y}_i| \tag{4.1}$$

$$||\mathbf{y}||_2 = \sqrt{\mathbf{y}^T\mathbf{y}} \tag{4.2}$$

$$||\mathbf{y}||_\infty = \max_{1\le i\le m} |\mathbf{y}_i| \tag{4.3}$$

$$||\mathbf{A}||_1 = \max_{1\le j\le m} \sum_{i=1}^{n} |a_{ij}| \tag{4.4}$$

$$||\mathbf{A}||_2 = \sqrt{\lambda_{max}\left(\mathbf{A}^T\mathbf{A}\right)} \tag{4.5}$$

$$||\mathbf{A}||_\infty = \max_{1\le i\le n} \sum_{i=1}^{m} |a_{ij}| \tag{4.6}$$

4.2.2 $\mathcal{L}$-Norms

Consider a function $\mathbf{f} : [0, \infty) \rightarrow \mathbb{R}^n$ for which $\mathcal{L}$-norm definition are as follows

$$||\mathbf{f}||_{\mathcal{L}_1} = \int_0^\infty ||\mathbf{f}(\tau)|| \, d\tau \tag{4.7}$$

$$||\mathbf{f}||_{\mathcal{L}_\infty} = \max_{1 \leq i \leq n} \left(\sup_{\tau \geq 0} |f_i(\tau)| \right) \tag{4.8}$$

The truncated $\mathcal{L}_\infty$ norm is defined as

$$||(\mathbf{f})_t||_{\mathcal{L}_\infty} \triangleq \max_{1 \leq i \leq n} \left(\sup_{0 \leq \tau \leq t} |f_i(\tau)| \right) \tag{4.9}$$

4.2.3 $\mathcal{L}_1$ Gain

For a stable proper single-input-single-output-system $G(s)$, its $\mathcal{L}_1$ gain is defined as follows.

$$||G(s)||_{\mathcal{L}_1} \triangleq \int_0^\infty |g(\tau)| \, d\tau \tag{4.10}$$

where $g(t)$ denotes the impulse response of $G(s)$. For a stable m input n output linear time invariant (LTI) system $\boldsymbol{\mathcal{H}}(s)$, its $\mathcal{L}_1$ gain is given by

$$||\boldsymbol{\mathcal{H}}(s)||_{\mathcal{L}_1} \triangleq \max_{1 \leq i \leq n} \sum_{j=1}^{m} ||\mathcal{H}_{ij}(s)||_{\mathcal{L}_1} \tag{4.11}$$

4.3 Problem Formulation

Consider the dynamics of the AV-8B Harrier to be as follows

$$\Delta \dot{\mathbf{X}}_{ad}(t) = \mathbf{A}_m \, \Delta \mathbf{X}_{ad}(t) + \mathbf{B}_m \, \boldsymbol{\omega} \, \Delta \mathbf{U}_{ad}(t) + \mathbf{f} \left(\Delta \mathbf{X}_{ad}(t), \mathbf{Z}(t), t \right) \tag{4.12}$$

$$\dot{\mathbf{x}}_z(t) = \mathbf{g} \left(\mathbf{x}_z(t), \Delta \mathbf{X}_{ad}(t), t \right) \tag{4.13}$$

$$\mathbf{Z}(t) = \mathbf{g}_\circ \left(\mathbf{x}_z(t), t \right) \tag{4.14}$$

$\Delta\mathbf{X}_{ad}(t) = [\ \Delta h(t)\ \Delta\phi(t)\ \Delta\theta(t)\ \Delta\psi(t)\ \Delta u(t)\ \Delta v(t)\ \Delta w(t)\ \Delta p(t)\ \Delta q(t)\ \Delta r(t)\ ]^T$ and $\Delta\mathbf{U}_{ad}(t) = [\ \Delta\delta_S(t)\ \Delta\delta_T(t)\ \Delta\delta_A(t)\ \Delta\delta_R(t)\ ]^T$. $\mathbf{A}_m \in \mathbb{R}^{10\times10}$ is a known Hurwitz matrix that specifies the desired dynamics for closed loop, and $\mathbf{B}_m \in \mathbb{R}^{10\times4}$ is a known control influence matrix such that the pair $(\mathbf{A}_m, \mathbf{B}_m)$ is controllable. $\boldsymbol{\omega} \in \mathbb{R}^{4\times4}$ is an uncertain input gain matrix; $\mathbf{Z}(t) \in \mathbb{R}^p$ and $\mathbf{x}_z(t) \in \mathbb{R}^l$ are the output and state vectors of unmodeled internal dynamics; $\mathbf{f} : \mathbb{R}^{10} \times \mathbb{R}^p \times \mathbb{R} \to \mathbb{R}^{10}$, $\mathbf{g} : \mathbb{R}^l \times \mathbb{R}^{10} \times \mathbb{R} \to \mathbb{R}^l$, and $\mathbf{g}_\circ : \mathbb{R}^l \times \mathbb{R} \to \mathbb{R}^p$ are unknown non-linear functions that are continuous in their arguments. The $\mathcal{L}_1$ adaptive control formulation requires systems to be square, i.e. systems with equal number of outputs and inputs. In this regard, heading angle $\Delta\psi(t)$ is chosen as an output in conjunction with velocity $\Delta V(t)$, altitude $\Delta h(t)$, and slip velocity $\Delta v(t)$, which were considered in the LQI formulation. If $\mathbf{y} \in \mathbb{R}^4$ denotes the vector of outputs, then

$$\mathbf{y}(t) \ = \ \mathbf{C}_m\ \Delta\mathbf{X}_{ad}(t) \tag{4.15}$$

$\mathbf{y}(t) \ = \ [\ \Delta V(t)\ \Delta h(t)\ \Delta v(t)\ \Delta\psi(t)\ ]^T$, $\mathbf{C}_m \in \mathbb{R}^{4\times10}$ is a known full rank constant output matrix, and the pair $(\mathbf{A}_m, \mathbf{C}_m)$ is observable. Also, let $\bar{\mathbf{X}}(t) \triangleq \left[\Delta\mathbf{X}_{ad}^T(t)\ \mathbf{Z}^T(t)\right]^T$ such that $\mathbf{f}\left(\Delta\mathbf{X}_{ad}(t),\ \mathbf{Z}(t), t\right) \triangleq \mathbf{f}\left(\bar{\mathbf{X}}(t), t\right)$. The system in Eqs. (4.12) - (4.14) also satisfies the following assumptions.

1 - Initial condition : The initial state $\Delta\mathbf{X}_{ad}(0)$ is assumed to be inside an arbitrarily large known set, i.e. $\left|\left|\Delta\mathbf{X}_{ad}(0)\right|\right|_\infty \leq \rho_0 < \infty$ for some $\rho_0 > 0$.

Also if $\rho_{in} \triangleq \left|\left|s\left(s\mathbb{I}_{10\times10} - \mathbf{A}_m\right)^{-1}\right|\right|_{\mathcal{L}_1} \rho_0$ and $\Delta\mathbf{X}_{in}(t) \triangleq \left(s\mathbb{I}_{10\times10} - \mathbf{A}_m\right)^{-1} \Delta\mathbf{X}_{ad}(0)$, then $\left|\left|\Delta\mathbf{X}_{in}(t)\right|\right|_{\mathcal{L}_\infty} \leq \rho_{in}$.

2 - Matching condition : There exists an unknown non-linear function $\mathbf{f}^* : \mathbb{R}^{10} \times \mathbb{R}^p \times \mathbb{R} \mapsto \mathbb{R}^4$ such that the matching condition $\mathbf{B}_m\ \mathbf{f}^*\left(\bar{\mathbf{X}}(t), t\right) \ = \ \mathbf{f}\left(\bar{\mathbf{X}}(t), t\right)$ is satisfied due to which Eq.(4.12) can be written as

$$\Delta\dot{\mathbf{X}}_{ad}(t) = \mathbf{A}_m\ \Delta\mathbf{X}_{ad}(t) + \mathbf{B}_m\ \left(\boldsymbol{\omega}\ \Delta\mathbf{U}_{ad}(t) + \mathbf{f}^*\left(\bar{\mathbf{X}}(t), t\right)\right) \tag{4.16}$$

3 - Boundedness of $\mathbf{f}^*(0,t)$: There exists a constant $\mathcal{B}^* > 0$ such that $||\mathbf{f}^*(0,t)||_\infty < \mathcal{B}^*$ for all $t \geq 0$.

4 - Semiglobal uniform boundedness of partial derivatives For any $\epsilon > 0$, there exist arbitrary constants $d_{f_x}(\epsilon) > 0$ and $d_{f_t}(\epsilon) > 0$ such that if $\left|\left|\bar{\mathbf{X}}(t)\right|\right|_\infty < \epsilon$, the partial derivatives are piecewise continuous and bounded.

$$\left|\left|\frac{\partial \mathbf{f}^*}{\partial \bar{\mathbf{X}}}\right|\right|_\infty \leq d_{f_x}(\epsilon) \quad \text{and} \quad \left|\left|\frac{\partial \mathbf{f}^*}{\partial t}\right|\right|_\infty \leq d_{f_t}(\epsilon)$$

Assumptions 3 and 4 ensure that the non-linear differential equation in 4.16 with the initial condition $\bar{\mathbf{X}}(0)$ has a has a unique solution for $t \geq 0$

5 - Stability of unmodeled dynamics The unmodeled dynamics given in Eqs. (4.13)-(4.14) are bounded-input-bounded-output (BIBO) stable with respect to the input $\Delta\mathbf{X}_{ad}(t)$ and the initial conditions $x_z(0)$, and satisfy the following relation for all $t \geq 0$

$$||(\mathbf{Z})_t||_{\mathcal{L}_\infty} \leq L_z\, ||(\Delta\mathbf{X}_{ad})_t||_{\mathcal{L}_\infty} + \mathcal{B}_z \tag{4.17}$$

where L_z and $\mathcal{B}_z$ are positive constants, and $||(\cdot)_t||_{\mathcal{L}_\infty}$ denotes the extended $\mathcal{L}_\infty$ norm in the interval $[0, t]$

6 - Knowledge of the input gain The uncertain input gain $\boldsymbol{\omega}$ is assumed to be strictly row diagonally dominant with known signs for its diagonal elements. Also there exists a known compact convex set Ω such that $\boldsymbol{\omega} \in \Omega$.

7 - Stability of transmission zeros The choice of $\mathbf{A}_m$, $\mathbf{B}_m$ and $\mathbf{C}_m$ ensures that the transmission zeros of the transfer matrix $\mathbf{H}(s) = \mathbf{C}_m(s\mathbb{I}_{10\times 10} - \mathbf{A}_m)^{-1}\mathbf{B}_m$ lie in the open left half plane.

The objective of $\mathcal{L}_1$ adaptive control is to synthesize a state feedback control law $\Delta\mathbf{U}_{ad}(t)$, which compensates for the non-linear uncertainty $\mathbf{f}^*$ in the control bandwidth that is defined by a low pass filter $\mathbf{C}(s)$, and ensures that the output tracks the reference input $\Delta\mathbf{r}_c(t) \in \mathbb{R}^{4\times 1}$ both in transient and steady-state, while other signals remain bounded. Therefore, the desired closed loop dynamics is given by

$$\Delta\dot{\mathbf{X}}_{ad}(t) = \mathbf{A}_m\ \Delta\mathbf{X}_{ad}(t)\ +\ \mathbf{B}_m\mathbf{K}_g\ \Delta\mathbf{r}_c(t) \tag{4.18}$$

where $\mathbf{K}_{ad} \in \mathbb{R}^{4\times 4}$ is the feed-forward gain matrix given be $\mathbf{K}_g = -\mathbf{C}_m\mathbf{A}_m^{-1}\mathbf{B}_m$. The low-pass filter $\mathbf{C}(s)$ is a proper stable transfer matrix for all $\boldsymbol{\omega} \in \Omega$ given by

$$\mathbf{C}(s) = \boldsymbol{\omega}\mathbf{k}\mathbf{D}(s)\left(\mathbb{I}_{4\times 4} + \boldsymbol{\omega}\mathbf{k}\mathbf{D}(s)\right)^{-1} \tag{4.19}$$

where $\mathbf{D}(s)$ is a strictly proper 4×4 transfer matrix which ensures, and $\mathbf{k} \in \mathbb{R}^{4\times 4}$ is a feedback gain matrix, and $\mathbf{C}(0) = \mathbb{I}_{4\times 4}$. Introducing the low pass filter in the feedback loop eliminates the presence of any high frequency signals in the control channels arising due to fast adaptation. This essentially means the adaptation loop is decoupled from the feedback loop, and the adaptation rates can be set arbitrarily high. The bandwidth of the low-pass filter also governs the trade-off between performance and robustness.

4.4 Equivalent Linear Time Varying System

To cancel the unknown non-linear uncertainty $\mathbf{f}^*(\cdot,\cdot)$ in Eq.(4.16) and thus obtain the desired closed loop dynamics in Eq.(4.18), the uncertainty needs to be first estimated. This is achieved by estimating the unknown time varying parameters of a linear system representation of $\mathbf{f}^*(\cdot,\cdot)$ which is defined below. If ρ, ρ_u and d_x are positive constants such that $||(\Delta\mathbf{X}_{ad})_\tau||_{\mathcal{L}_\infty} \leq \rho$, $||(\Delta\mathbf{U}_{ad})_\tau||_{\mathcal{L}_\infty} \leq \rho_u$ and

$\left|\left|\Delta\dot{\mathbf{X}}_{ad}\right|\right|_{\mathcal{L}_\infty} \leq d_x$, then for all $t \in [0\ \tau]$, there exist differentiable $\boldsymbol{\mu}(t) \in \mathbb{R}^{4\times 1}$ and $\boldsymbol{\eta}(t) \in \mathbb{R}^{4\times 1}$ such that

$$\mathbf{f}^*(\Delta\mathbf{X}_{ad}(t), \mathbf{Z}(t), t) = \boldsymbol{\mu}(t)\, ||(\Delta\mathbf{X}_{ad})_t||_{\mathcal{L}_\infty} + \boldsymbol{\eta}(t) \tag{4.20}$$

and for some positive constants μ_b, η_b, $d\mu_b$, and $d\eta_b$

$$||\boldsymbol{\mu}(t)||_\infty < \mu_b \qquad ||\dot{\boldsymbol{\mu}}(t)||_\infty < d_\mu$$
$$||\boldsymbol{\eta}(t)||_\infty < \mu_b \qquad ||\dot{\boldsymbol{\eta}}(t)||_\infty < d_\eta$$

Owing to this transformation, Eq.(4.16) becomes

$$\Delta\dot{\mathbf{X}}_{ad}(t) = \mathbf{A}_m\ \Delta\mathbf{X}_{ad}(t) + \mathbf{B}_m \left(\ \boldsymbol{\omega}\ \Delta\mathbf{U}_{ad}(t) + \boldsymbol{\mu}\, ||(\Delta\mathbf{X}_{ad})_t||_{\mathcal{L}_\infty} + \boldsymbol{\eta}(t)\ \right) \tag{4.21}$$

4.5 State Predictor

Consider the state predictor which replicates the plant dynamics in Eq.(4.21) using the adaptive estimates as follows

$$\Delta\dot{\hat{\mathbf{X}}}_{ad}(t) = \mathbf{A}_m\ \Delta\hat{\mathbf{X}}_{ad}(t) + \mathbf{B}_m \left(\ \hat{\boldsymbol{\omega}}\ \Delta\mathbf{U}_{ad}(t) + \hat{\boldsymbol{\mu}}(t)\, ||(\Delta\mathbf{X}_{ad})_t||_{\mathcal{L}_\infty} + \hat{\boldsymbol{\eta}(t)}\ \right) \tag{4.22}$$

$$\text{with } \Delta\hat{\mathbf{X}}_{ad}(0) = \Delta\mathbf{X}_{ad}(0)$$

where $\Delta\hat{\mathbf{X}}_{ad}(t) \in \mathbb{R}^{10\times 1}$ is the predictor state vector; $\hat{\boldsymbol{\omega}} \in \mathbb{R}^{4\times 4}$, $\hat{\boldsymbol{\mu}}(t) \in \mathbb{R}^{4\times 1}$ and $\hat{\boldsymbol{\eta}}(t) \in \mathbb{R}^{4\times 1}$ are the adaptive estimates.

4.6 Adaptation laws

The adaptation laws for $\hat{\boldsymbol{\omega}}$, $\hat{\boldsymbol{\mu}}(t)$, and $\hat{\boldsymbol{\eta}}(t)$ are defined as

$$\dot{\hat{\boldsymbol{\omega}}}(t) = \Gamma_k\ \text{Proj}\left(\hat{\boldsymbol{\omega}}(t), -\left(\Delta\tilde{\mathbf{X}}_{ad}^T(t)\mathbf{P}\mathbf{B}_m\right)^T \Delta\mathbf{U}_{ad}^T(t)\right) \tag{4.23}$$

$$\dot{\hat{\boldsymbol{\mu}}}(t) = \Gamma_k\ \text{Proj}\left(\hat{\boldsymbol{\mu}}(t), -\left(\Delta\tilde{\mathbf{X}}_{ad}^T(t)\mathbf{P}\mathbf{B}_m\right)^T ||(\Delta\mathbf{X}_{ad})_t||_{\mathcal{L}_\infty}\right) \tag{4.24}$$

$$\dot{\hat{\boldsymbol{\eta}}}(t) = \Gamma_k \text{ Proj}\left(\hat{\boldsymbol{\eta}}(t), -\left(\Delta\tilde{\mathbf{X}}_{ad}^T(t)\mathbf{P}\mathbf{B}_m\right)^T\right) \tag{4.25}$$

where, $\Gamma_k \in \mathbb{R}$ denotes the adaptation again, $\Delta\tilde{\mathbf{X}}_{ad}(t) = \Delta\hat{\mathbf{X}}_{ad}(t) - \Delta\mathbf{X}_{ad}(t)$, and $\mathbf{P} = \mathbf{P}^T > 0$ is determined as a solution to the Lyapunov equation $\mathbf{A}_m^T\mathbf{P} + \mathbf{P}\mathbf{A}_m = -\boldsymbol{\mathcal{Q}}$ for a specified $\boldsymbol{\mathcal{Q}} = \boldsymbol{\mathcal{Q}}^T > 0$. Proj$(\cdot,\cdot)$ is the projection operator which guarantees $\hat{\boldsymbol{\omega}} \in \Omega$, $||\hat{\boldsymbol{\mu}}(t)||_\infty \leq \mu_{\mathbf{B}}$, and $||\hat{\boldsymbol{\eta}}(t)||_\infty \leq \eta_{\mathbf{B}}$. The projection operator for any two vectors $\boldsymbol{\Theta}, \boldsymbol{\mathcal{Y}} \in \mathbb{R}^n$ is defined as

$$\text{Proj}(\boldsymbol{\Theta}(t), \boldsymbol{\mathcal{Y}}(t)) = \begin{cases} \boldsymbol{\mathcal{Y}} & \text{if } \mathcal{F}(\boldsymbol{\Theta}) < 0, \\ \boldsymbol{\mathcal{Y}} & \text{if } \mathcal{F}(\boldsymbol{\Theta}) \geq 0 \text{ and } \nabla\mathcal{F}^T\boldsymbol{\mathcal{Y}} \leq 0, \\ \boldsymbol{\mathcal{Y}} - \dfrac{\nabla\mathcal{F}\nabla\mathcal{F}^T}{||\nabla\mathcal{F}||^2}\boldsymbol{\mathcal{Y}}\mathcal{F}(\boldsymbol{\Theta}) & \text{if } \mathcal{F}(\boldsymbol{\Theta}) \geq 0 \text{ and } \nabla\mathcal{F}^T\boldsymbol{\mathcal{Y}} > 0, \end{cases} \tag{4.26}$$

where, $\mathcal{F} : \mathbb{R}^n \to \mathbb{R}$ is a smooth convex function defined as

$$\mathcal{F}(\boldsymbol{\Theta}) \triangleq \frac{(\epsilon_{\boldsymbol{\Theta}} + 1)\,\boldsymbol{\Theta}^T\boldsymbol{\Theta} - \boldsymbol{\Theta}_{\max}^2}{\epsilon_{\boldsymbol{\Theta}}\boldsymbol{\Theta}_{\max}^2} \tag{4.27}$$

where $\boldsymbol{\Theta}_{\max}$ is the specified norm bound for $\boldsymbol{\Theta}$, and $\epsilon_{\boldsymbol{\Theta}}$ is the projection tolerance.

4.7 Control Law

The $\mathcal{L}_1$ adaptive control law is given by

$$\Delta\mathbf{U}_{ad}(s) = -\mathbf{k}\mathbf{D}(s)\hat{\boldsymbol{\mathcal{N}}}(s) \tag{4.28}$$

where $\hat{\boldsymbol{\mathcal{N}}}(s)$ is the Laplace transform of the signal

$$\hat{\boldsymbol{\mathcal{N}}}(t) \triangleq \hat{\boldsymbol{\omega}}\ \Delta\mathbf{U}_{ad}(t) + \boldsymbol{\mu}(t)\,||(\Delta\mathbf{X}_{ad})_t||_{\mathcal{L}_\infty} + \boldsymbol{\eta}(t) - \mathbf{K}_g\ \Delta\mathbf{r}_c(t) \tag{4.29}$$

4.8 Sufficient Condition for Stability

The $\mathcal{L}_1$ adaptive controller tracks a closed-loop reference system both in transient and in steady state, whose stability needs to be characterized first. The ideal reference system is defined as follows, under the assumption that $\boldsymbol{\omega}$ and $\mathbf{f}^*(\cdot,\cdot)$ are known.

$$\Delta\dot{\mathbf{X}}_{ref}(t) = \mathbf{A}_m\ \Delta\mathbf{X}_{ref}(t) + \mathbf{B}_m\ \left(\boldsymbol{\omega}\ \Delta\mathbf{U}_{ref}(t) + \mathbf{f}^*\left(\bar{\mathbf{X}}_{ref}(t), t\right)\right) \tag{4.30}$$

$$\Delta\mathbf{U}_{ref}(s) = -\mathbf{k}\mathbf{D}(s)\boldsymbol{\mathcal{N}}_{ref}(s) \tag{4.31}$$

$$\boldsymbol{\mathcal{N}}_{ref}(t) \triangleq \boldsymbol{\omega}\ \Delta\mathbf{U}_{ref}(t) + \mathbf{f}^*\left(\bar{\mathbf{X}}_{ref}(t), t\right) - \mathbf{K}_g\ \Delta\mathbf{r}_c(t) \tag{4.32}$$

$$\Delta\mathbf{Y}_{ref}(t) = \mathbf{C}_m\Delta\mathbf{X}_{ref}(t) \tag{4.33}$$

The choice of $\mathbf{k}$ and $\mathbf{D}(s)$ should guarantee the existence of a constant $\rho_r > \rho_\circ$ such that $\left|\left|\left(\Delta\mathbf{X}_{ref}(t)\right)_\tau\right|\right|_{\mathcal{L}_\infty} < \rho_r$ by satisfying the following $\mathcal{L}_1$ norm condition.

$$||\mathbf{H}_x(s)\left(\mathbb{I}_{4\times4} - \mathbf{C}(s)\right)||_{\mathcal{L}_1} < \frac{\rho_r - ||\mathbf{H}_x(s)\mathbf{C}(s)\mathbf{K}_g||_{\mathcal{L}_1}\ ||(\Delta\mathbf{r}_c)_\tau||_{\mathcal{L}_\infty} - \rho_{in}}{\mu_B\ \rho_r + \mathcal{B}^*} \tag{4.34}$$

where $\mathbf{H}_x(s) = (s\mathbb{I}_{10\times10} - \mathbf{A}_m)^{-1}\mathbf{B}_m$. Increasing the bandwidth of the low pass filter $\mathbf{C}(s)$ results in reduction of $||(\mathbb{I}_{4\times4} - \mathbf{C}(s))||_{\mathcal{L}_1}$. Hence, the left hand side of Eq.(4.34) can be rendered arbitrarily small by increasing the filter bandwidth, thus satisfying the sufficient condition for stability.

4.9 Stability of the Adaptation Laws

This section presents a proof for boundedness of the prediction error for the specific $\mathcal{L}_1$ controller developed in this thesis. A more generalized proof can be found in [20].

Lemma 1 : For the plant dynamics in Eq.(4.16), the controller and adaptation laws defined in Eqs.(4.22) -(4.28) subject to the $\mathcal{L}_1$ norm condition, if $||(\Delta \mathbf{X}_{ad})_\tau||_{\mathcal{L}_\infty} \leq \rho$ and $||(\Delta \mathbf{U}_{ad})_\tau||_{\mathcal{L}_\infty} \leq \rho_u$, the prediction error is bounded as follows

$$\left|\left|\left(\Delta \tilde{\mathbf{X}}_{ad}\right)_\tau\right|\right|_{\mathcal{L}_\infty} \leq \sqrt{\frac{\Theta_m}{\Gamma_k \ \lambda_{min}\left(\mathbf{P}\right)}} \tag{4.35}$$

where

$$\Theta_m \triangleq \frac{16 \ \lambda_{max}\left(\mathbf{P}\right)}{\lambda_{min}\left(\boldsymbol{\mathcal{Q}}\right)} \left[\ \mu_B d_\mu + \eta_B d_\eta \ \right] + 4 \left[\max_{\boldsymbol{\omega} \in \Omega} \text{tr}\left(\boldsymbol{\omega}^T \boldsymbol{\omega}\right) + 4\mu_B^2 + 4\eta_B^2 \right] \tag{4.36}$$

Proof : For all $t \in [0, \tau]$, the following upper bounds are

$$\begin{aligned} ||\boldsymbol{\mu}(t)||_\infty < \mu_b \qquad ||\dot{\boldsymbol{\mu}}(t)||_\infty < d_\mu \\ ||\boldsymbol{\eta}(t)||_\infty < \mu_b \qquad ||\dot{\boldsymbol{\eta}}(t)||_\infty < d_\eta \end{aligned}$$

Consider a candidate Lyapunov function given by

$$\mathcal{V}(t) = \Delta \tilde{\boldsymbol{X}}_{ad}^T(t) \mathbf{P} \Delta \tilde{\boldsymbol{X}}_{ad}(t) + \frac{1}{\Gamma_k} \left[tr\left(\tilde{\boldsymbol{\omega}}^T(t) \tilde{\boldsymbol{\omega}}(t)\right) + \tilde{\boldsymbol{\mu}}^T(t) \tilde{\boldsymbol{\mu}}(t) + \tilde{\boldsymbol{\eta}}^T(t) \tilde{\boldsymbol{\eta}}(t) \right] \tag{4.37}$$

Let $\tau_1 \in (0, \tau]$ be a time instant of discontinuity of either $\dot{\boldsymbol{\mu}}(t)$ or $\dot{\boldsymbol{\eta}}(t)$. Consider the derivative of the candidate Lyapunov function in $t \in [0, \tau_1)$ as follows.

$$\begin{aligned} \dot{\mathcal{V}}(t) \ = \ & -\Delta \tilde{\boldsymbol{X}}_{ad}^T(t) \ \boldsymbol{\mathcal{Q}} \ \Delta \tilde{\boldsymbol{X}}_{ad}(t) + 2 \ \Delta \tilde{\boldsymbol{X}}_{ad}^T(t) \ \mathbf{P}\mathbf{B}_m \ \tilde{\boldsymbol{\omega}}(t) \ \Delta \mathbf{U}_{ad}(t) \\ & + 2 \ \Delta \tilde{\boldsymbol{X}}_{ad}^T(t) \ \mathbf{P}\mathbf{B}_m \ \tilde{\boldsymbol{\mu}}(t) \ \ ||(\Delta \mathbf{X}_{ad}(t))_t||_{\mathcal{L}_\infty} \\ & + 2 \ \Delta \tilde{\boldsymbol{X}}_{ad}^T(t) \ \mathbf{P}\mathbf{B}_m \ \tilde{\boldsymbol{\eta}}(t) \\ & + \frac{2}{\Gamma_k} \left[tr\left(\tilde{\boldsymbol{\omega}}^T(t) \ \dot{\tilde{\boldsymbol{\omega}}}(t)\right) + \tilde{\boldsymbol{\mu}}^T(t) \dot{\tilde{\boldsymbol{\mu}}}(t) + \tilde{\boldsymbol{\eta}}^T(t) \dot{\tilde{\boldsymbol{\eta}}}(t) \right] \end{aligned} \tag{4.38}$$

Further simplifying these equations,

$$
\begin{aligned}
\dot{\mathcal{V}}(t) \;=\; & -\Delta\tilde{\boldsymbol{X}}_{ad}^{T}(t)\ \boldsymbol{\mathcal{Q}}\ \Delta\tilde{\boldsymbol{X}}_{ad}(t) \\
& + \frac{2}{\Gamma_k}\ \mathrm{tr}\left[\tilde{\boldsymbol{\omega}}^{T}(t)\left(\dot{\hat{\boldsymbol{\omega}}}(t) + \Gamma_k\left(\boldsymbol{X}_{ad}^{T}(t)\ \mathbf{PB}_m\ \right)^{T}\Delta\mathbf{U}_{ad}^{T}\right)\right] \\
& + \frac{2}{\Gamma_k}\tilde{\boldsymbol{\mu}}^{T}(t)\left[\dot{\hat{\boldsymbol{\mu}}}(t) + \Gamma_k\left(\boldsymbol{X}_{ad}^{T}(t)\ \mathbf{PB}_m\right)^{T}||(\Delta\mathbf{X}_{ad}(t))_t||_{\mathcal{L}_\infty}\right] \\
& + \frac{2}{\Gamma_k}\tilde{\boldsymbol{\eta}}^{T}(t)\left[\dot{\hat{\boldsymbol{\eta}}}(t) + \Gamma_k\left(\boldsymbol{X}_{ad}^{T}(t)\ \mathbf{PB}_m\right)^{T}\right] \\
& + \frac{2}{\Gamma_k}\left[\tilde{\boldsymbol{\mu}}^{T}(t)\dot{\boldsymbol{\mu}}(t) + \tilde{\boldsymbol{\eta}}^{T}(t)\dot{\boldsymbol{\eta}}(t)\right] \qquad (4.39)
\end{aligned}
$$

Consider the following property of projection based adaptation laws as given in [29]. For any two vectors $\boldsymbol{\Theta}(t), \boldsymbol{\mathcal{Y}}(t) \in \mathbb{R}^n$ and a given $\boldsymbol{\Theta}^*(t) \in \mathbb{R}^n$,

$$
\left(\boldsymbol{\Theta}(t) - \boldsymbol{\Theta}^*(t)\right)^{T}\left(\mathrm{Proj}\left(\boldsymbol{\Theta}(t), \boldsymbol{\mathcal{Y}}(t)\right) - \boldsymbol{\mathcal{Y}}(t)\right) \leq 0 \qquad (4.40)
$$

By substituting the projection based adaptation laws from Eqs(4.23) to (4.25) in Eq.(4.39), and using the above projection property, the following relation is obtained.

$$
\dot{\mathcal{V}}(t) \leq -\Delta\tilde{\mathbf{X}}_{ad}^{T}(t)\ \boldsymbol{\mathcal{Q}}\ \Delta\tilde{\mathbf{X}}_{ad}(t) + \ \frac{2}{\Gamma_k}\left[\tilde{\boldsymbol{\mu}}^{T}(t)\dot{\boldsymbol{\mu}}(t) + \tilde{\boldsymbol{\eta}}^{T}(t)\dot{\boldsymbol{\eta}}(t)\right] \qquad (4.41)
$$

Further,

$$
\dot{\mathcal{V}}(t) \leq -\Delta\tilde{\mathbf{X}}_{ad}^{T}(t)\ \boldsymbol{\mathcal{Q}}\ \Delta\tilde{\mathbf{X}}_{ad}(t) + \ \frac{2}{\Gamma_k}\left|\left[\tilde{\boldsymbol{\mu}}^{T}(t)\dot{\boldsymbol{\mu}}(t) + \tilde{\boldsymbol{\eta}}^{T}(t)\dot{\boldsymbol{\eta}}(t)\right]\right| \qquad (4.42)
$$

The maximum value that the second term in the above equation can take is obtained by substituting the respective upper bounds to obtain

$$
\dot{\mathcal{V}}(t) \leq -\Delta\tilde{\mathbf{X}}_{ad}^{T}(t)\ \boldsymbol{\mathcal{Q}}\ \Delta\tilde{\mathbf{X}}_{ad}(t) + \ \frac{16}{\Gamma_k}\left[\ \mu_B d_\mu(t) + \eta_B d_\eta(t)\ \right] \qquad (4.43)
$$

The quadratic forms are bounded as shown below.

$$\lambda_{min}\left(\mathbf{P}\right)\left|\left|\Delta\tilde{\mathbf{X}}_{ad}(t)\right|\right|_2^2 \leq \Delta\tilde{\mathbf{X}}_{ad}^T(t)\mathbf{P}\Delta\tilde{\mathbf{X}}_{ad}(t) \leq \lambda_{max}\left(\mathbf{P}\right)\left|\left|\Delta\tilde{\mathbf{X}}_{ad}(t)\right|\right|_2^2 \tag{4.44}$$

$$\lambda_{min}\left(\boldsymbol{\mathcal{Q}}\right)\left|\left|\Delta\tilde{\mathbf{X}}_{ad}(t)\right|\right|_2^2 \leq \Delta\tilde{\mathbf{X}}_{ad}^T(t)\boldsymbol{\mathcal{Q}}\Delta\tilde{\mathbf{X}}_{ad}(t) \leq \lambda_{max}\left(\boldsymbol{\mathcal{Q}}\right)\left|\left|\Delta\tilde{\mathbf{X}}_{ad}(t)\right|\right|_2^2 \tag{4.45}$$

From Eq.(4.37),

$$\mathcal{V}(t) \leq \lambda_{max}\left(\mathbf{P}\right)\left|\left|\Delta\tilde{\mathbf{X}}_{ad}(t)\right|\right|_2^2 + \frac{4}{\Gamma_k}\left[\max_{\boldsymbol{\omega}\in\Omega}\mathrm{tr}\left(\boldsymbol{\omega}^T\boldsymbol{\omega}\right) + 4\mu_B^2 + 4\eta_B^2\right] \tag{4.46}$$

To determine a uniform upper bound on $\mathcal{V}(t)$ for $t \in [0, \tau)$, two cases of the Lyapunov derivative are considered.

Case 1 When $\dot{\mathcal{V}}(t) \geq 0$. From Eq.(4.39),

$$\left|\left|\Delta\tilde{\mathbf{X}}_{ad}(t)\right|\right|_2^2 \leq \frac{16}{\Gamma_k\ \lambda_{min}\left(\boldsymbol{\mathcal{Q}}\right)}\left[\ \mu_B d_\mu + \eta_B d_\eta\ \right] \tag{4.47}$$

The upper bound on $\mathcal{V}(t)$, found from Eqs. (4.46) and(4.47), is

$$\mathcal{V}(t) \leq \frac{16\ \lambda_{max}\left(\mathbf{P}\right)}{\Gamma_k\ \lambda_{min}\left(\boldsymbol{\mathcal{Q}}\right)}\left[\ \mu_B d_\mu + \eta_B d_\eta\ \right] + \frac{4}{\Gamma_k}\left[\max_{\boldsymbol{\omega}\in\Omega}\mathrm{tr}\left(\boldsymbol{\omega}^T\boldsymbol{\omega}\right) + 4\mu_B^2 + 4\eta_B^2\right] \tag{4.48}$$

Let

$$\Theta_m = \frac{16\ \lambda_{max}\left(\mathbf{P}\right)}{\lambda_{min}\left(\boldsymbol{\mathcal{Q}}\right)}\left[\ \mu_B d_\mu + \eta_B d_\eta\ \right] + 4\left[\max_{\boldsymbol{\omega}\in\Omega}\mathrm{tr}\left(\boldsymbol{\omega}^T\boldsymbol{\omega}\right) + 4\mu_B^2 + 4\eta_B^2\right] \tag{4.49}$$

Therefore, $\mathcal{V}(t) \leq \dfrac{\Theta_m}{\Gamma_k}$ when $\dot{\mathcal{V}}(t) \geq 0$

Case 2 When $\dot{\mathcal{V}}(t) < 0$. Since $\Delta\tilde{\mathbf{X}}_{ad}(0) = \Delta\mathbf{X}_{ad}(0)$

$$\mathcal{V}(0) = \frac{1}{\Gamma_k}\left[tr\left(\tilde{\boldsymbol{\omega}}^T(t)\tilde{\boldsymbol{\omega}}(t)\right) + \tilde{\boldsymbol{\mu}}^T(t)\tilde{\boldsymbol{\mu}}(t) + \tilde{\boldsymbol{\eta}}^T(t)\tilde{\boldsymbol{\eta}}(t)\right] \tag{4.50}$$

This implies

$$\mathcal{V}(0) \leq \frac{4}{\Gamma_k}\left[\max_{\boldsymbol{\omega}\in\Omega}\mathrm{tr}\left(\boldsymbol{\omega}^T\boldsymbol{\omega}\right) + 4\mu_B^2 + 4\eta_B^2\right] \leq \Theta_m \tag{4.51}$$

Moreover, from Eq.(4.43), for $\dot{\mathcal{V}} < 0$,

$$\left|\left|\Delta\tilde{\mathbf{X}}_{ad}(t)\right|\right|_2^2 > \frac{16}{\Gamma_k\ \lambda_{min}\left(\boldsymbol{\mathcal{Q}}\right)}\left[\ \mu_B d_\mu + \eta_B d_\eta\ \right] \tag{4.52}$$

On substituting Eq,(4.52) in Eq.(4.46), the upper bound on $\mathcal{V}$ in Eq.(4.46) is

$$\lambda_{max}\left(\mathbf{P}\right)\left|\left|\Delta\tilde{\mathbf{X}}_{ad}(t)\right|\right|_2^2 + \frac{4}{\Gamma_k}\left[\max_{\boldsymbol{\omega}\in\Omega}\mathrm{tr}\left(\boldsymbol{\omega}^T\boldsymbol{\omega}\right) + 4\mu_B^2 + 4\eta_B^2\right] > \frac{\Theta_m}{\Gamma_k} \tag{4.53}$$

However, since $\dot{\mathcal{V}}(t) < 0$, $\mathcal{V}(t)$ cannot grow larger than $\frac{\Theta_m}{\Gamma_k}$, i.e. $\mathcal{V}(t) \leq \frac{\Theta_m}{\Gamma_k}$. Therefore, for all $t \in [0, \tau_1)$ the bound $\mathcal{V}(t) \leq \frac{\Theta_m}{\Gamma_k}$ holds good. Moreover,

$$\Delta\tilde{\mathbf{X}}_{ad}^T(t)\mathbf{P}\Delta\tilde{\mathbf{X}}_{ad}(t) \leq \mathcal{V}(t) \leq \frac{\Theta_m}{\Gamma_k} \tag{4.54}$$

$$\lambda_{min}\left(\mathbf{P}\right)\left|\left|\Delta\tilde{\mathbf{X}}_{ad}(t)\right|\right|_2^2 \leq \frac{\Theta_m}{\Gamma_k} \tag{4.55}$$

$$\left|\left|\Delta\tilde{\mathbf{X}}_{ad}(t)\right|\right|_2 \leq \sqrt{\frac{\Theta_m}{\Gamma_k\ \lambda_{min}\left(\mathbf{P}\right)}} \tag{4.56}$$

This further implies

$$\left|\left|\Delta\tilde{\mathbf{X}}_{ad}(t)\right|\right|_\infty \leq \sqrt{\frac{\Theta_m}{\Gamma_k\ \lambda_{min}\left(\mathbf{P}\right)}} \qquad \forall t \in [0, \tau_1)$$

Also, $\mathcal{V}(t) \leq \frac{\Theta_m}{\Gamma_k}$ because $\boldsymbol{\mu}(t)$, $\boldsymbol{\eta}(t)$, $\hat{\boldsymbol{\mu}}(t)$, and, $\hat{\boldsymbol{\eta}}(t)$ are continuous. If there exists another time instant $\tau_2 \in [\tau_1, \tau)$ when the derivative of either of $\boldsymbol{\mu}(t)$ or $\boldsymbol{\eta}(t)$ is discontinuous, it can be shown that

$$\left|\left|\Delta\tilde{\mathbf{X}}_{ad}(t)\right|\right|_\infty \leq \sqrt{\frac{\Theta_m}{\Gamma_k\ \lambda_{min}\left(\mathbf{P}\right)}} \qquad \forall t \in [\tau_1, \tau_2)$$

Repeating this procedure for $t \in [0, \tau]$, the following relation is obtained.

$$\left|\left|\left(\Delta\tilde{\mathbf{X}}_{ad}\right)_\tau\right|\right|_{\mathcal{L}_\infty} \leq \sqrt{\frac{\Theta_m}{\Gamma_k\ \lambda_{min}\left(\mathbf{P}\right)}} \tag{4.57}$$

The above equation presents a highly conservative upper bound on $\left|\left|\left(\Delta\tilde{\mathbf{X}}_{ad}(t)\right)_\tau\right|\right|_{\mathcal{L}_\infty}$. Hence, the prediction error dynamics can be driven arbitrarily small by increasing the adaptation gain.

4.10 Transient and Steady State performance

The ideal closed loop reference system shown in Eqs.(4.30) -(4.32) that the actual system tracks involves the unknown terms, $\boldsymbol{\omega},\ \mathbf{f}(\cdot,\cdot),$ and $\mathbf{Z}$ because of which the ideal reference system cannot be implemented The stability and performance of the actual closed loop system with respect to the reference system is determined using the following theorem.

Theorem 1 : Let c_1 and c_2 be positive constants such that

$$c_1 \triangleq \frac{||\mathbf{H}_x(s)\mathbf{C}(s)\mathbf{H}^{-1}(s)\mathbf{C}_m||_{\mathcal{L}_1}}{1-\mu_B\,||\mathbf{H}_x(s)\,(\mathbb{I}_{4\times4}-\mathbf{C}(s))||_{\mathcal{L}_1}}c_0+c_3 \tag{4.58}$$

$$c_2 \triangleq \mu_B\ c_1\ \left|\left|\boldsymbol{\omega}^{-1}\mathbf{C}(s)\right|\right|_{\mathcal{L}_1}+c_0\left|\left|\boldsymbol{\omega}^{-1}\mathbf{C}(s)\mathbf{H}^{-1}(s)\mathbf{C}_m\right|\right|_{\mathcal{L}_1} \tag{4.59}$$

where, c_0 and c_3 are arbitrarily small constants, and let the adaptive gain be lower bounded as follows.

$$\Gamma_k > \frac{\Theta_m}{\lambda_{min}\,(\mathbf{P})\,c_0^2} \tag{4.60}$$

Given the actual system in 4.16 implemented with the $\mathcal{L}_1$ adaptive controller in Eqs. (4.22) to (4.28) subject to the $\mathcal{L}_1$ norm condition, and the closed-loop reference system given in Eqs.(4.30) - (4.32), if $||\Delta\mathbf{X}_{ad}\,(0)||_\infty \leq \rho_0 < \infty$, then

$$||(\Delta\mathbf{X}_{ad})_\tau||_{\mathcal{L}_\infty} \leq \rho \tag{4.61}$$

$$||(\Delta\mathbf{U}_{ad})_\tau||_{\mathcal{L}_\infty} \leq \rho_u \tag{4.62}$$

$$\left|\left|\left(\Delta\tilde{\mathbf{X}}_{ad}\right)_\tau\right|\right|_{\mathcal{L}_\infty} < c_0 \tag{4.63}$$

$$\left|\left|(\Delta\mathbf{X}_{ad}-\Delta\mathbf{X}_{ref})_\tau\right|\right|_{\mathcal{L}_\infty} < c_1 \tag{4.64}$$

$$\left|\left|(\Delta\mathbf{U}_{ad}-\Delta\mathbf{U}_{ref})_\tau\right|\right|_{\mathcal{L}_\infty} < c_2 \tag{4.65}$$

$$\left|\left|(\Delta\mathbf{Y}_{ad}-\Delta\mathbf{Y}_{ref})_\tau\right|\right|_{\mathcal{L}_\infty} < c_1\,||\mathbf{C}_m||_\infty \tag{4.66}$$

Proof : The reader is referred to Theorem 3.2.1 in [20] for the proof. The constants c_0, c_1, and c_2 can be rendered small by arbitrarily increasing Γ_k as a consequence of which the actual closed loop system closely tracks the reference system both in steady state and in transients.

4.11 Reference Systems Design

Initially, an $\mathcal{L}_1$ adaptive controller was designed based on the linear model corresponding to the steady, straight and level flight condition at $V = 500ft/s$, $H = 1000ft$, and $\dot{\psi} = 0°/s$ to perform the automatic landing. However, simulations indicated that the tracking performance of the controller degraded at speeds below $100ft/s$ due to its inability to handle the uncertainties. Hence, for low speed flight conditions, another $\mathcal{L}_1$ adaptive controller is designed based on the reference model corresponding to $V = 150ft/s$, $\dot{\psi} = 0°/s$ and $H = 1000ft$. The switch from the high-speed controller to the low sped controller is made at a velocity of $150ft/s$. The drift and the control influence matrices, $\mathbf{A} \in \mathbb{R}^{10\times10}$ and $\mathbf{B} \in \mathbb{R}^{10\times4}$, respectively, at these flight conditions are taken from the linear model database that was developed for the gain-scheduled controller. For each of the two flight conditions, a reference model matrix $\mathbf{A}_m$ is designed using linear quadratic regulator (LQR) technique by selecting the state and control weighting matrices,$\mathbf{Q}_w \in \mathbb{R}^{10\times10}$ and $\mathbf{R}_w \in \mathbb{R}^{4\times4}$, appropriately. If $\mathbf{k}_m \in \mathbb{R}^{4\times10}$ denotes the feedback gain matrix determined using LQR, then $\mathbf{A}_m = \mathbf{A} - \mathbf{B}\mathbf{k}_m$ and $\mathbf{B}_m = \mathbf{B}$. The output matrix $\mathbf{C}_m$ needed for

calculating the inverse DC gain $\mathbf{K}_g$ for each of these flight conditions, is determined as follows.

$$\mathbf{C}_m = \begin{bmatrix} 0 & 0 & 0 & 0 & \frac{u_0}{V_0} & \frac{v_0}{V_0} & \frac{w_0}{V_0} & 0 & 0 & 0 \\ 1 & 0 & 0 & 0 & 0 & 0 & 0 & 0 & 0 & 0 \\ 0 & 0 & 0 & 0 & 0 & 1 & 0 & 0 & 0 & 0 \\ 0 & 0 & 0 & 1 & 0 & 0 & 0 & 0 & 0 & 0 \end{bmatrix} \tag{4.67}$$

where $u_0,\ v_0,\ w_0,$ and V_0 are the trim velocities that were defined in chapter 2. The $\boldsymbol{\mathcal{Q}}$ matrix required for calculating $\mathbf{P}$ is chosen to be an identity matrix, i.e. $\boldsymbol{\mathcal{Q}} = \mathbb{I}_{10\times 10}$. Henceforth, subscripts 'hi' and 'lo' will be used to denote the matrices corresponding to high-speed and low-speed reference models, respectively. The state and control weighting matrices that are chosen to assign the closed loop dynamics for the high-speed controller are $\mathbf{Q}_{hi} = 200 \cdot \mathbb{I}_{10\times 10}$ and $\mathbf{R}_{hi} = 10 \cdot \mathbb{I}_{4\times 4}$, while those chosen for the low speed controller are $\mathbf{Q}_{lo} = \text{diag}\left(\left[\ 100\ 100\ 100\ 100\ 1000\ 100\ 100\ 100\ 100\ 100\right]^T\right)$ and $\mathbf{R}_{lo} = 10 \cdot \mathbb{I}_{4\times 4}$. Eqs.(4.68) - (4.71) show the reference models that are used for designing the two controllers.

$$\mathbf{A}_{m_{hi}} = \begin{bmatrix} 0 & 0 & 8.73 & 0 & 0.06 & 0 & -1 & 0 & 0.43 & 0 \\ 0 & 0 & 0 & 0 & 0 & 0 & 0 & 1 & 0 & 0.06 \\ 0 & 0 & 0 & 0 & 0 & 0 & 0 & 0 & 1 & 0 \\ 0 & 0 & 0 & 0 & 0 & 0 & 0 & 0 & 0 & 1 \\ -0.07 & 0.38 & -2.5 & 0.18 & -1.96 & 0.29 & 0.03 & 0.38 & -0.76 & -0.28 \\ 0.07 & 1.48 & 0.79 & 2.11 & 0.03 & -2.3 & -0.06 & 1.44 & 0.05 & -5.9 \\ -1.25 & 1.32 & -15.61 & 1.24 & -0.69 & 0 & -0.71 & 1.28 & 6.78 & 0.3 \\ -7.62 & -297.71 & -64.72 & -253.39 & -0.16 & -34.99 & 4.86 & -297.06 & -4.98 & -13.62 \\ -18.35 & -2.44 & -223.51 & -2.12 & -3.25 & 0 & 6.79 & -2.62 & -25.92 & -0.31 \\ -0.97 & -13.72 & -10.3 & -27.97 & -0.33 & 25.04 & 0.82 & -13.47 & -0.65 & -35.13 \end{bmatrix} \tag{4.68}$$

$$\mathbf{C}_{m_{hi}} = \begin{bmatrix} 0 & 0 & 0 & 0 & 1 & 0 & 0.06 & 0 & 0 & 0 \\ 1 & 0 & 0 & 0 & 0 & 0 & 0 & 0 & 0 & 0 \\ 0 & 0 & 0 & 0 & 0 & 1 & 0 & 0 & 0 & 0 \\ 0 & 0 & 0 & 1 & 0 & 0 & 0 & 0 & 0 & 0 \end{bmatrix} \tag{4.69}$$

$$\mathbf{B}_{m_{hi}} = \begin{bmatrix} 0 & 0 & 0 & 0 \\ 0 & 0 & 0 & 0 \\ 0 & 0 & 0 & 0 \\ 0 & 0 & 0 & 0 \\ 0.01 & 0.43 & -0.07 & -0.07 \\ 0 & 0 & -0.3 & 0.49 \\ 0.29 & 0.11 & -0.29 & 0 \\ 0 & 0 & 65.61 & 9.07 \\ 4.09 & 0.24 & 0.66 & 0 \\ 0 & 0 & 4.22 & -6.02 \end{bmatrix} \tag{4.70}$$

$$\mathbf{A}_{m_{lo}} = \begin{bmatrix} 0 & 0 & 2.62 & 0 & 0.06 & 0 & -1 & 0 & 0.06 & 0 \\ 0 & 0 & 0 & 0 & 0 & 0 & 0 & 1 & 0 & 0.07 \\ 0 & 0 & 0 & 0 & 0 & 0 & 0 & 0 & 1 & 0 \\ 0 & 0 & 0 & 0 & 0 & 0 & 0 & 0 & 0 & 1 \\ -0.62 & 0.1 & -1.2 & 0.08 & -2.05 & 0.03 & 0.79 & 0.09 & 0.11 & 0.01 \\ 0 & 0.62 & 0.02 & 0.28 & -0.02 & -0.33 & 0 & 0.24 & 0.01 & -2.13 \\ 1.69 & -0.93 & 0.86 & -0.73 & 6.13 & -0.25 & -2.47 & -0.82 & 1.5 & -0.13 \\ -1.3 & -61.25 & -15.06 & -45.84 & 9.25 & -20.57 & 1.06 & -55.02 & -4.23 & -2.78 \\ -2.02 & -2.84 & -19.5 & -2.09 & 10.55 & -0.99 & 2.09 & -2.5 & -6.91 & -0.14 \\ -0.03 & -3.05 & -0.86 & -5.37 & 0.6 & 2.78 & 0.08 & -3.03 & -0.22 & -6.86 \end{bmatrix} \tag{4.71}$$

$$\mathbf{C}_{m_{lo}} = \begin{bmatrix} 0 & 0 & 0 & 0 & 0.99 & 0 & 0.065 & 0 & 0 & 0 \\ 1 & 0 & 0 & 0 & 0 & 0 & 0 & 0 & 0 & 0 \\ 0 & 0 & 0 & 0 & 0 & 1 & 0 & 0 & 0 & 0 \\ 0 & 0 & 0 & 1 & 0 & 0 & 0 & 0 & 0 & 0 \end{bmatrix} \tag{4.72}$$

$$\mathbf{B}_{m_{lo}} = \begin{bmatrix} 0 & 0 & 0 & 0 \\ 0 & 0 & 0 & 0 \\ 0 & 0 & 0 & 0 \\ 0 & 0 & 0 & 0 \\ -0.01 & 0.29 & -0.04 & 0 \\ 0 & 0 & -0.04 & 0.11 \\ 0.08 & -0.84 & 0.29 & 0 \\ 0 & 0 & 17.01 & 1.44 \\ 1.29 & -0.42 & 0.88 & 0.11 \\ 0 & 0 & 1.18 & -1.43 \end{bmatrix} \tag{4.73}$$

4.12 Filter Design

The design of the low pass filter for the $\mathcal{L}_1$ adaptive controller involves selection the gain matrix $\mathbf{K}$ and the transfer matrix $\mathbf{D}(s)$ to obtain the desired tracking performance and robustness. The bounds for the projection operator are chosen conservatively as follows. $\mu_B = 20$, $\eta_B = 20$, and

$$\Omega = \begin{bmatrix} [0.1, 10] & [-10, 10] & [-10, 10] & [-10, 10] \\ [-10, 10] & [0.1, 10] & [-10, 10] & [-10, 10] \\ [-10, 10] & [-10, 10] & [0.1, 10] & [-0.1, 10] \\ [-10, 10] & [-10, 10] & [-10, 10] & [0.1, 10] \end{bmatrix}$$

The diagonal elements of Ω are chosen to be strictly positive since it is known from the trim analysis that no control reversal occurs in the flight envelope considered for the automatic carrier landing system development. $\mathbf{C}(s)$ is chosen to be a first order filter for both high and low speed flight conditions by selecting $\mathbf{D}(s) = \frac{1}{s} \cdot \mathbb{I}_{4\times4}$. For both the flight conditions, $\mathbf{k} = 100 \cdot \mathbb{I}_{4\times4}$ is chosen initially, and their elements are tuned until the desired tracking performance is obtained without the presence of any high frequency signals in the input channel. The gain matrices were obtained after tuning are $\mathbf{k}_{hi} = \text{diag}\left(\begin{bmatrix} 50 & 2 & 40 & 40 \end{bmatrix}^T\right)$ and $\mathbf{k}_{lo} = \text{diag}\left(\begin{bmatrix} 50 & 30 & 40 & 40 \end{bmatrix}^T\right)$. These values of $\mathbf{k}_{hi}$ and $\mathbf{k}_{lo}$ do not satisfy the $\mathcal{L}_1$ gain condition for any value of ρ_r, but yield a satisfactory performance which is witnessed in simulations.

It is to be noted that selecting $\mathbf{k}$ to obtain the desired performance while satisfying $\mathcal{L}_1$ stability condition is still an open-ended problem [20]. By examining the condition in Eq.(4.34), it is seen that by increasing the bandwidth of the filter matrix, $||\mathbf{C}(s)||_{\mathcal{L}_1}$ can be increased arbitrarily, which in turn decreases the value of $||\mathbb{I}_{4\times4} - \mathbf{C}(s)||_{\mathcal{L}_1}$. However, this also increases $||\mathbf{H}_x(s)\mathbf{C}(s)\mathbf{K}_g||_{\mathcal{L}_1}$, in turn decreasing the magnitude of the right hand side of the expression.

4.13 Remarks on implementation

The adaptation gain Γ_k for both the low-speed and the high-speed controllers are chosen to be 500. The control law in Eq.(4.28) is written in terms of trim states and controls as follows

$$\mathbf{U}_{ad} = \mathbf{U}_{ad_0} + \Delta\mathbf{U}_{ad}(t) \tag{4.74}$$

Similarly, the state perturbation needed in Eq.(4.29) is found using $\Delta\mathbf{X}_{ad} = \mathbf{X}_{ad} - \mathbf{X}_{ad_0}$. $\mathbf{X}_{ad_0}$ and $\mathbf{U}_{ad_0}$ are the trim state and input vectors corresponding to the

commanded signals, $V_c,\ h_c,$ and $\dot{\psi}_c$, found by the trilinear interpolation of the trim values in $\mathcal{S}$. The reference signal supplied is

$$\Delta \mathbf{r}_c = [\Delta V \ \ \Delta h \ \ \Delta v \ \ \Delta \psi]^T \tag{4.75}$$

where, $\Delta V = V_c - V$, $\Delta h = h_c - h$, $\Delta v = v_c - v$, The heading angle error $\Delta\psi$, which is a constituent of the reference signal $\Delta \mathbf{r}_c$, and $\Delta \mathbf{X}_{ad}$, is determined using the technique illustrated in section(3.7). $V_c,\ h_c,$ and v_c are determined using guidance laws, while $V,\ h,\ v$ are the outputs of the aircraft model.

CHAPTER 5

GUIDANCE LAW DESIGN

5.1 Flight plan

So far, optimal, gain-scheduled, and $\mathcal{L}_1$ adaptive autopilots have been developed for the AV-8B Harrier in chapters (3) and (4), respectively, which allow for the tracking of commanded trajectories of velocity, turn-rate, altitude, and slip-velocity. The objective, in this chapter, is to develop guidance laws which enable the aircraft to fly along a predefined flight path, rendezvous with the aircraft carrier, and execute a vertical shipboard landing.

For the simulation of automatic landing, the aircraft carrier is initially assumed to be moving with an initial velocity of $50ft/s$ with a heading of 60° under the influence of sea-state 4 perturbations. To construct the flight path, the relative position of the aircraft with respect to the carrier is first transformed to "flight deck frame", a new coordinate frame defined such that its origin is centered at that of the inertial reference with its axes being parallel to the carrier's axes - x_S, y_S, z_S. Let $\tilde{x}$ and $\tilde{y}$ denote the relative position of the aircraft with respect to carrier measured in flight deck coordinates given by

$$\begin{bmatrix} \tilde{x} \\ \tilde{y} \end{bmatrix} = \begin{bmatrix} \cos\psi_{ac} & \sin\psi_{ac} \\ -\sin\psi_{ac} & \cos\psi_{ac} \end{bmatrix} \begin{bmatrix} p_N - x_{ac} \\ p_E - y_{ac} \end{bmatrix} \tag{5.1}$$

A flight plan is comprising of 3 flight legs shown fig.(5.1) is considered for designing the guidance laws. Initially, the aircraft is assumed to flying straight and level, with a heading of 240° and a velocity of $500ft/s$. The flight plan begins at waypoint 1 which is along the downwind leg, at the end of which the aircraft is

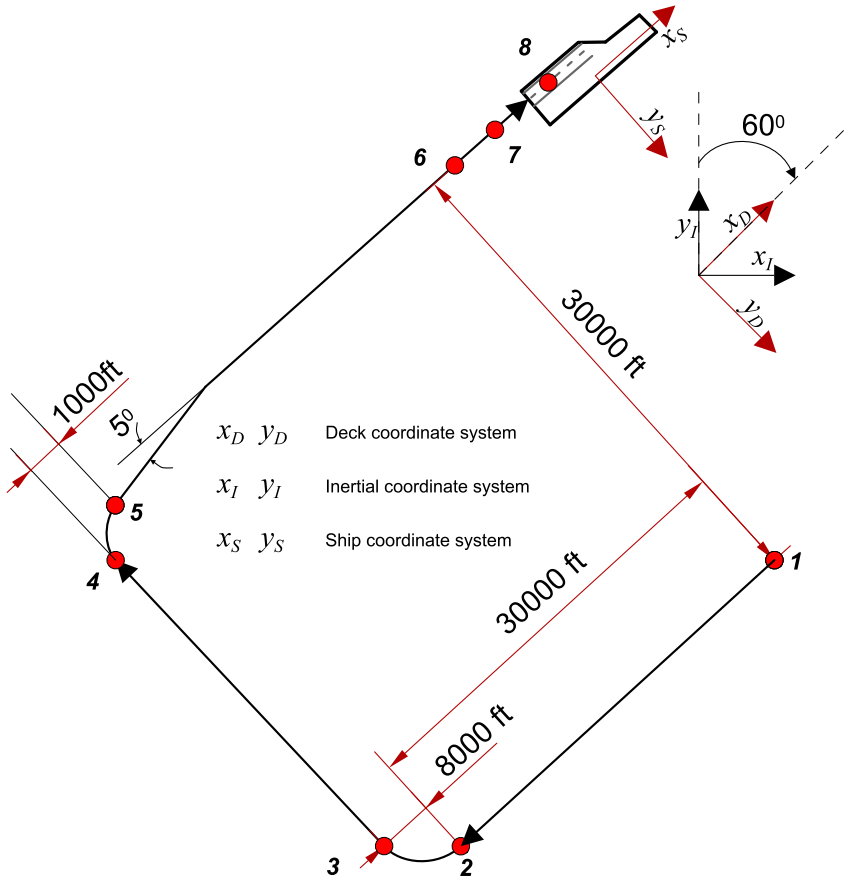

Figure 5.1: Flight path considered for automatic landing

required to decelerate to a velocity of $350ft/s$. Between waypoints 2 and 3, the aircraft is required to execute a 90° right hand turn, so that it is lined up with the base leg. The aircraft is further needed to decelerate from a velocity of 350 ft/s to $250ft/s$ along this leg while the altitude is maintained constant. The final leg begins at waypoint 4 with the execution of another right hand 85° turn towards the final leg. When the lateral separation between the aircraft and the carrier, which is measured perpendicular to the direction of carrier motion, is less than $50ft$, a 5°

heading correction is made to the flight path so that the aircraft is in-line with the touchdown point. Between waypoint 5 and 6, the aircraft velocity is decreased from $250ft/s$ to $51ft/s$, while it descents from an altitude of $1000ft$ to $120ft$. At waypoint 6, which is just $20ft$ to the aft of the landing zone on the carrier, the aircraft begins to fly at a relative velocity of just $1ft/s$ during which lateral position errors are minimized. When the axial separation between the aircraft and the waypoint is less than $5ft$, between waypoints 7 and 8, proportional navigational laws are activated to stabilize the aircraft over the landing point, and a vertical landing is performed with a constant descent rate.

5.2 Heading Angle Guidance

Heading angle reference commands are determined using two types of guidance laws. The first one is the widely used, lateral beam guidance law [30] which is given by

$$\psi_c = \psi_{des} - \sin^{-1}\left(\frac{\tilde{r} - \tilde{r}_{des}}{V\tau}\right) \tag{5.2}$$

where, ψ_c is the commanded heading angle, ψ_{des} is the desired heading angle, and $\tilde{r}$ is either $\tilde{x}$ or $\tilde{y}$ depending of the leg of flight, and $\tilde{r}_{des}$ is the value of $\tilde{r}$ at which the aircraft's heading angle ψ is desired to be equal to ψ_c. τ is a time constant, which is tuned to obtain a smooth trajectory. This guidance law was used only to prevent heading angle errors along straight flight paths, and not to perform the 90° turns at waypoints 2 and 4. This is because, when $\left(\frac{\tilde{r} - \tilde{r}_{des}}{V\tau}\right) \geq 1$, the commanded heading angle is indeterminate. To overcome this issue, a new heading angle command law is written by scaling and shifting a hyperbolic tangent function as follows

$$\psi_c = \psi_i + \left(\frac{\psi_{des} - \psi_i}{2\tanh(2.25)}\right)\left(\tanh(2.25) + \tanh\left(\left(1 - \frac{\tilde{r} - \tilde{r}_{des}}{\tilde{r}_i - \tilde{r}_{des}}\right)4.5 - 2.25\right)\right) \tag{5.3}$$

where, ψ_i is the initial heading angle, $\tilde{r}_i$ is the initial value of $\tilde{r}$. It is to be noted that the factor tanh(2.25) that is seen in the guidance law, is used so that the law replicates the behavior of tanh$(\cdot)$ function in the interval -2.5 and $+2.5$. To ensure that the aircraft tracks the heading angle commanded using the guidance laws in Eqs.(5.2) and (5.3) asymptotically, a turn-rate command law is employed as follows.

$$\dot{\psi}_c = -k_\psi \left(\psi_c - \psi\right) \tag{5.4}$$

The constant k_ψ is initially selected as 1, and tuned as needed to obtain the desired performance.

5.3 Velocity Guidance Law

Velocity reference commands are issued either using proportional laws or time-to-go laws. The proportional velocity command law is given by

$$V_c = V_i + \left(\frac{V_{des} - V_i}{\tilde{r}_{des} - \tilde{r}_i}\right)(\tilde{r} - \tilde{r}_i) \tag{5.5}$$

This guidance law is used to decelerate the aircraft along all flight segments except the final segment between waypoints 5 and 6. This is because the desired relative velocity at waypoint 6 is just $1ft/s$, and using the proportional would result in the aircraft requiring a large amount of time to reach the waypoint. To address this issue, a time-to-go based guidance law is formulated with a view to maintain constant deceleration between waypoints 5 and 6. At any instant of time 't', consider the following constant acceleration guidance law, given by

$$V_c = V_i + \left(\frac{V_f - V_i}{t_f - t_i}\right)(t - t_i) \tag{5.6}$$

$$= V_i + (V_f - V_i)\left(1 - \frac{t_f - t}{t_f - t_i}\right) \tag{5.7}$$

where, V_i and V_f are the initial and the desired final velocities, and t_f and t_i are the time instants corresponding to the start and the end points of the flight leg. Let $t_{go} = t_f - t$, which is known as time to go using which Eq.(5.7) is written as

$$V_c = V_i + (V_f - V_i)\left(1 - \frac{t_{go}}{t_{go_i}}\right) \tag{5.8}$$

However, by defining time-to-go as a ratio of range to the closing velocity [4], Eq.(5.8) becomes,

$$V_c = V_i + (V_f - V_i)\left(1 - \frac{\tilde{r}_f - \tilde{r}}{\tilde{r}_f - \tilde{r}_i}\frac{V_i - 50}{V - 50}\right) \tag{5.9}$$

5.4 Altitude Guidance Law

The altitude guidance law that is required to perform the final descent between waypoints 5 and 6 is chosen to be a time-to-go-based law, which takes a form similar to Eq.(5.9).

$$h_c = h_i + (h_f - h_i)\left(1 - \frac{\tilde{r}_f - \tilde{r}}{\tilde{r}_f - \tilde{r}_i}\frac{V_i - 50}{V - 50}\right) \tag{5.10}$$

The vertical touchdown which begins at waypoint 7 is achieved at a constant descent rate of $3ft/s$ using

$$h_c = h_i - 3(t_f - t_i) \tag{5.11}$$

5.5 Position Control Laws

At waypoint 7, it is imperative to minimize any axial and lateral position errors of the aircraft with respect to the touchdown point on the carrier. The axial position control is achieved by employing proportional navigation law

$$V_c = V_{ac} - k_V\tilde{x} \tag{5.12}$$

The lateral position control law is used to determine the slip velocity prior to touchdown as follows.

$$v_c = -k_v \tilde{y} \tag{5.13}$$

The constants k_V and k_v are initially chosen as 0.1, and are tuned to obtain satisfactory performance.

CHAPTER 6

RESULTS AND DISCUSSION

This chapter presents the results of the automatic carrier landing simulations that are performed using both control strategies : Gain-scheduled linear optimal control, and $\mathcal{L}_1$ adaptive control. These simulations are conducted in SIMULINK® using ODE45 Dormand-Prince solver, and are terminated when the altitude of the aircraft equals that of the carrier.

6.1 Gain-Scheduled Flight Control System

The simulation results of the automatic carrier landing performed using the gain-scheduled automatic flight coontrol system have been plotted in Figs.(6.1)-(6.9). From Fig.(6.1), the tracking performance is seen to satisfactory throughout the length of the flight. The spikes seen in the slip velocity at around 50 and 150 second mark are caused by the initiation and termination of the two 90° turns. The velocity tracking error, seen from Fig(6.2) is less than $1ft/s$. Between 250 and 350 seconds, the altitude tracking error ranges between $-5ft$ and $5ft$. This is attributed to the controller attempting to minimize velocity tracking error, at the expense of altitude tracking performance. Rendezvous of the aircraft with designated landing point on the carrier is achieved successfully, following which a vertical landing is performed as seen in Fig(6.3). The aircraft landed 1.86 ft to the aft and 0.35 ft to the right of the designated landing point. The maximum bank angle attained during turns is 60°, and the plots euler angles and body angular rates indicate smooth turns.

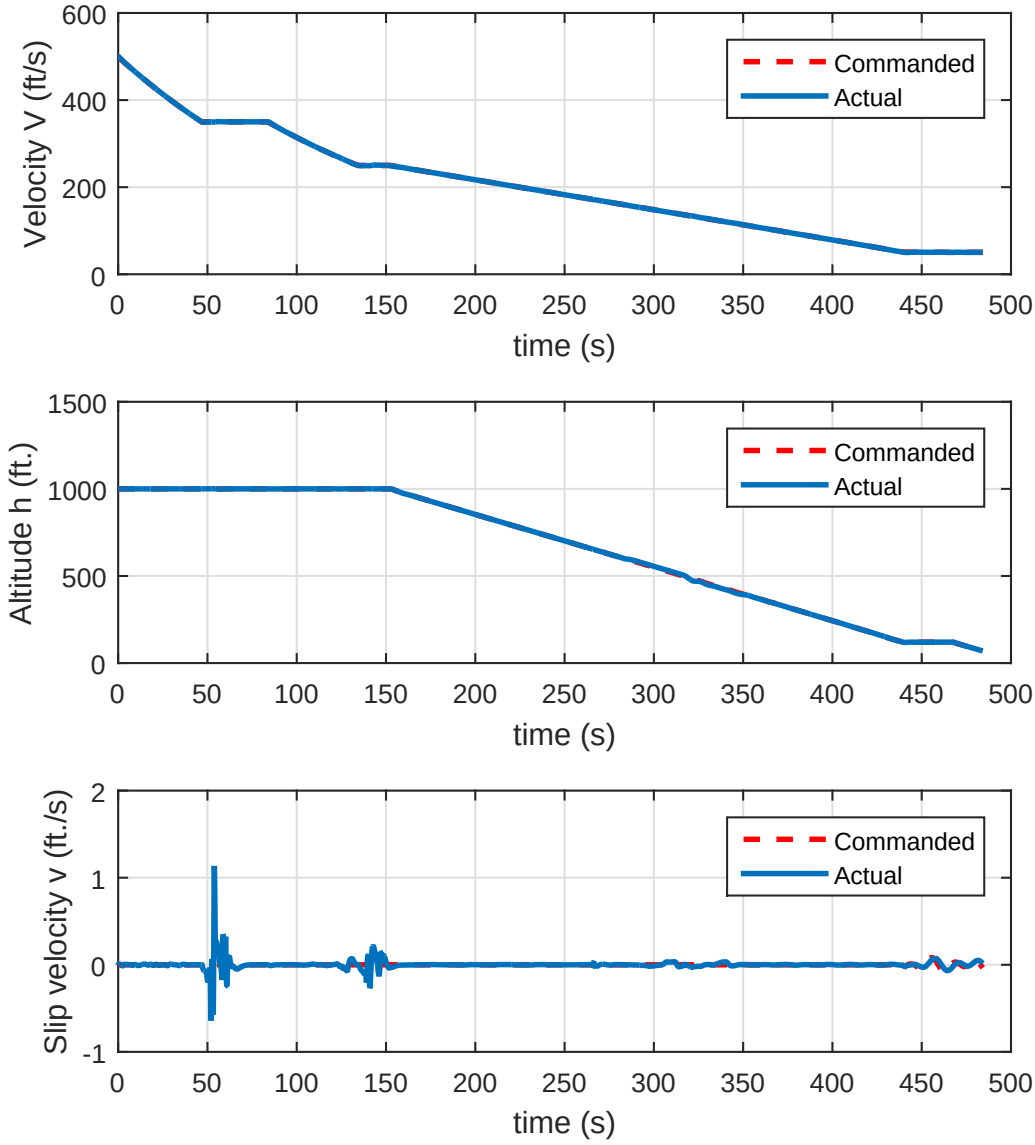

Figure 6.1: Velocity, altitude, and slip tracking performance

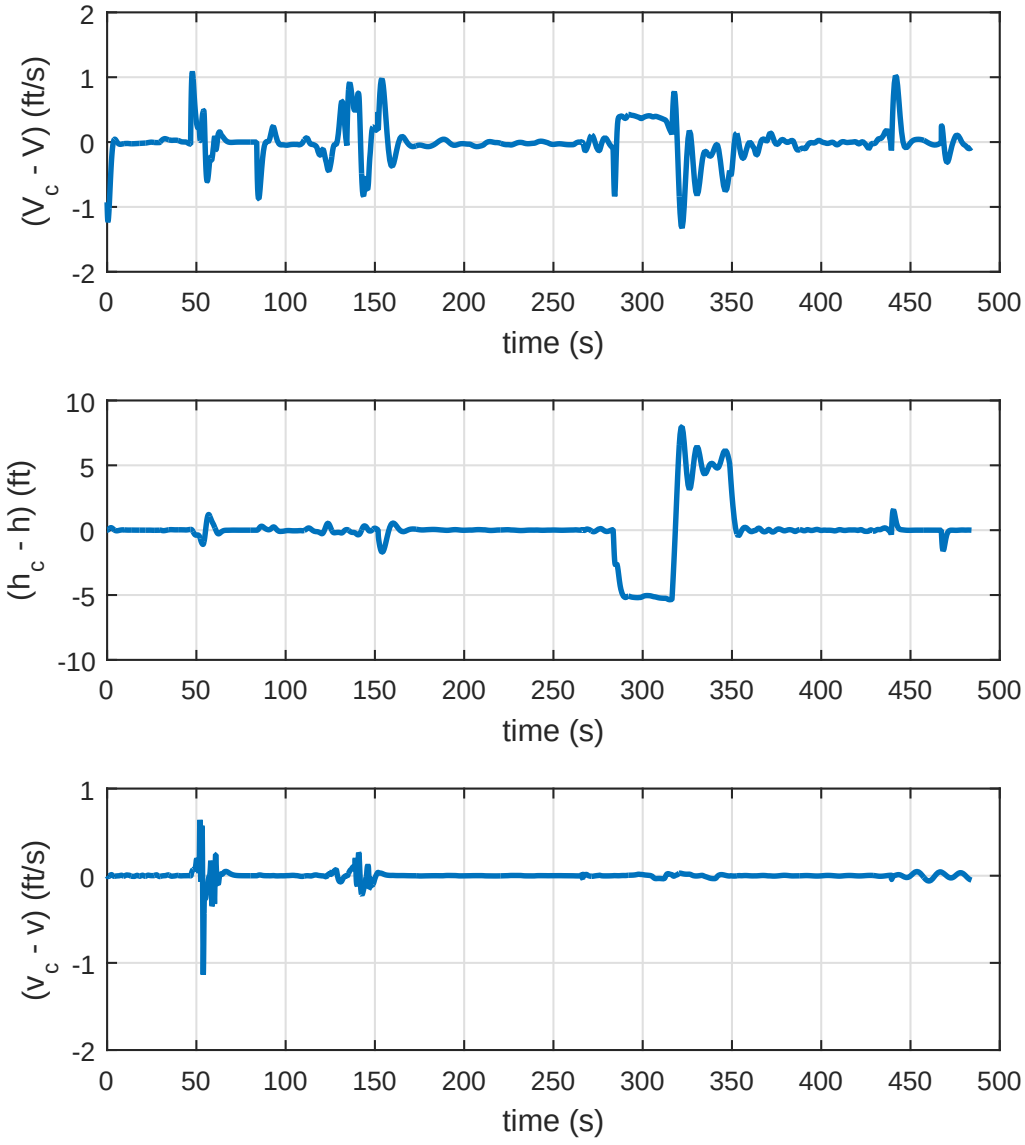

Figure 6.2: Variation of Velocity, altitude, and slip velocity tracking error with time

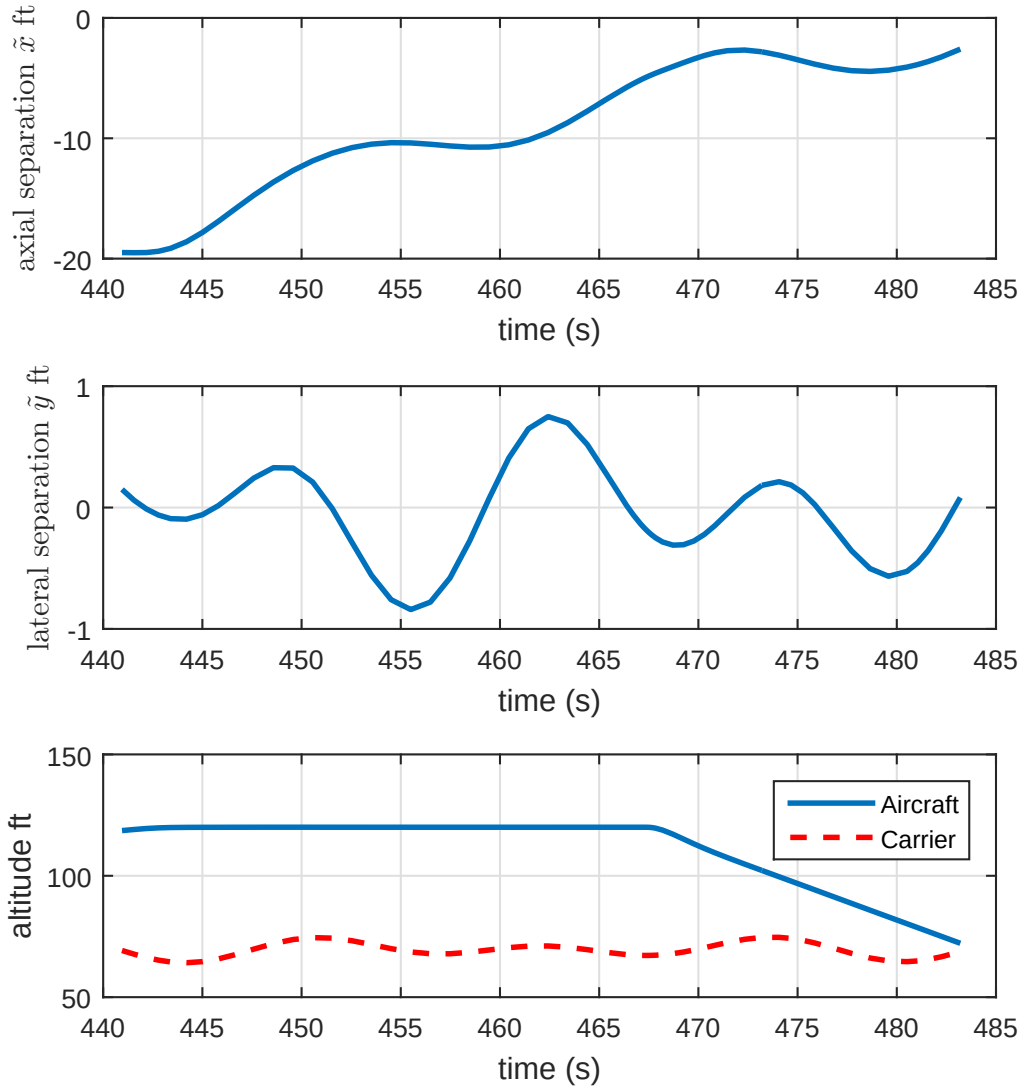

Figure 6.3: Variation of the longitudinal and lateral positions of the aircraft with respect to the carrier plotted along with altitude during touchdown

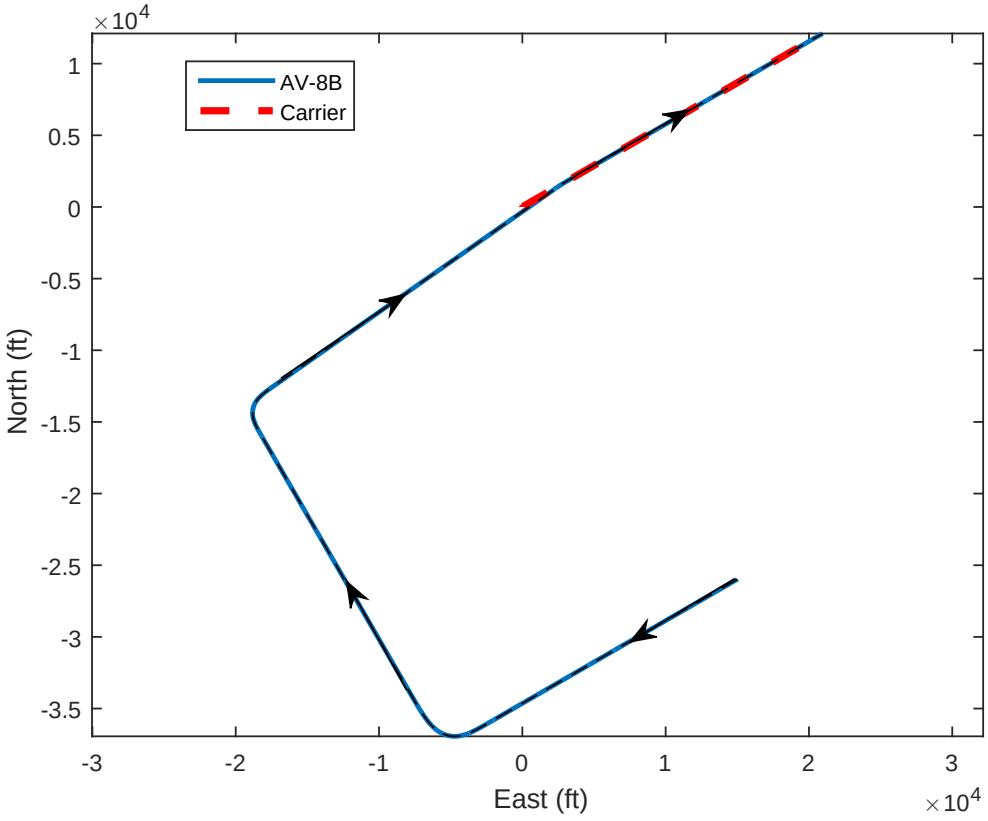

Figure 6.4: Ground track of the aircraft and the carrier

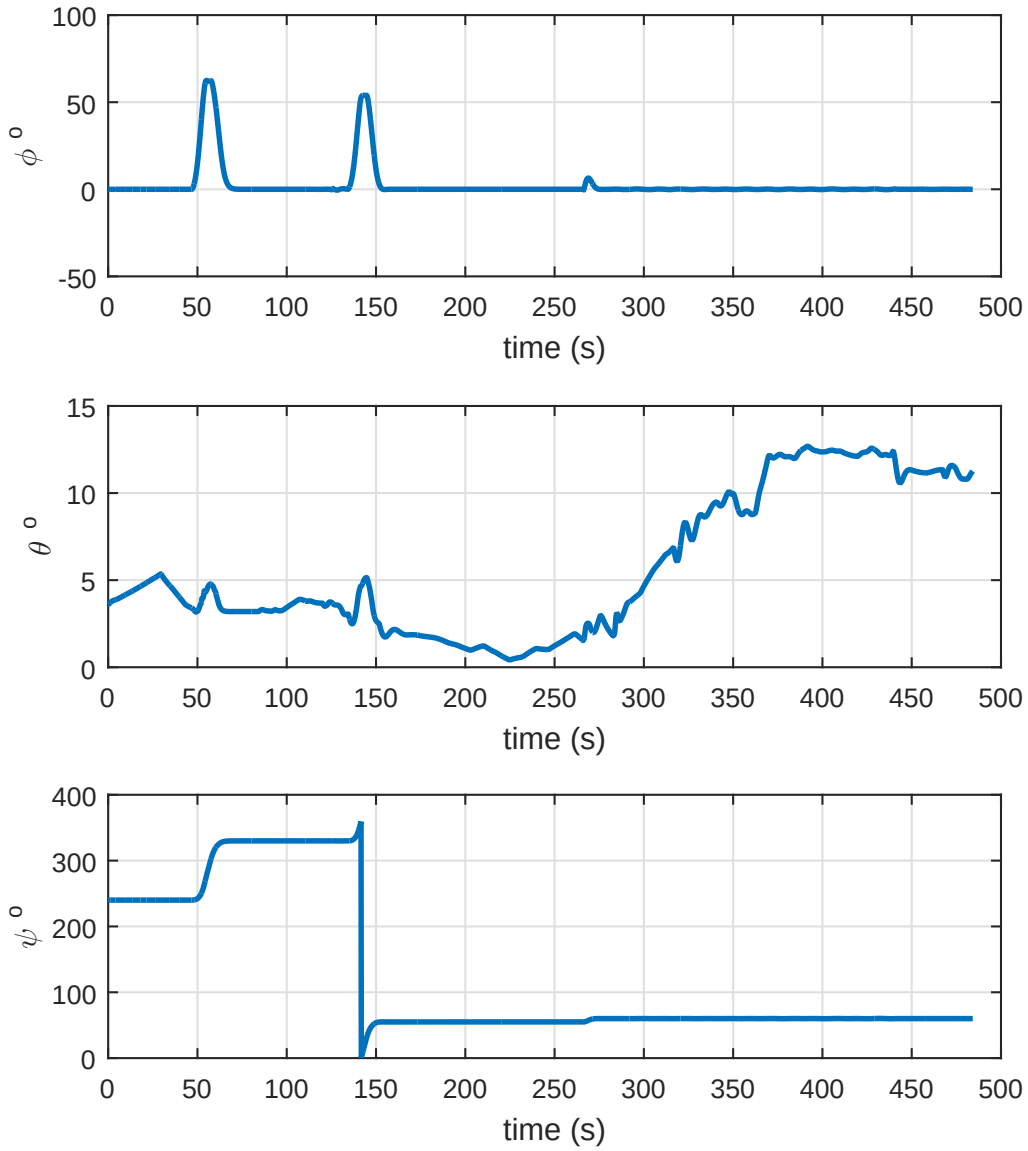

Figure 6.5: Variation of the aircraft's orientation with respect to the inertial frame in time

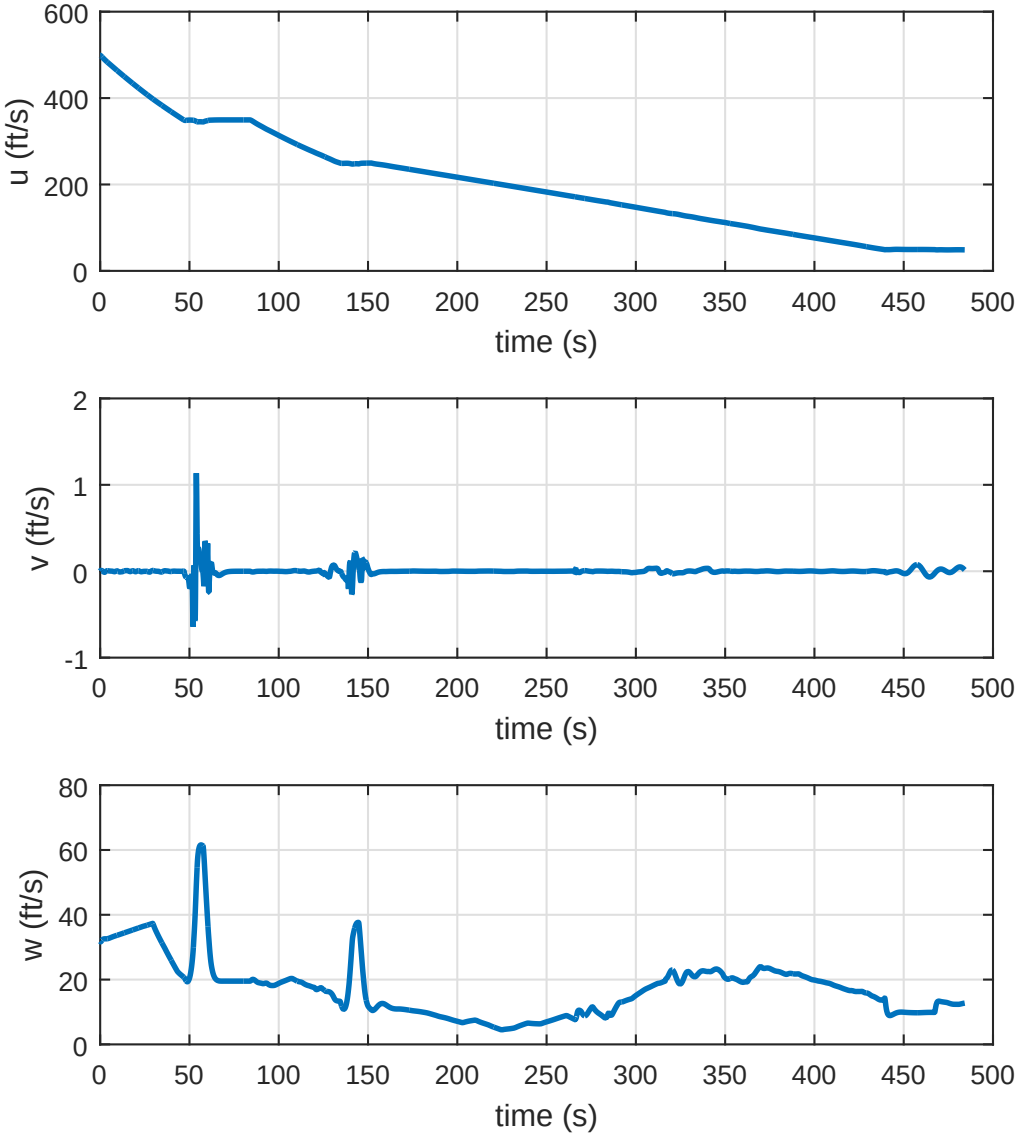

Figure 6.6: Variation of the aircraft's body component of velocities with respect to time

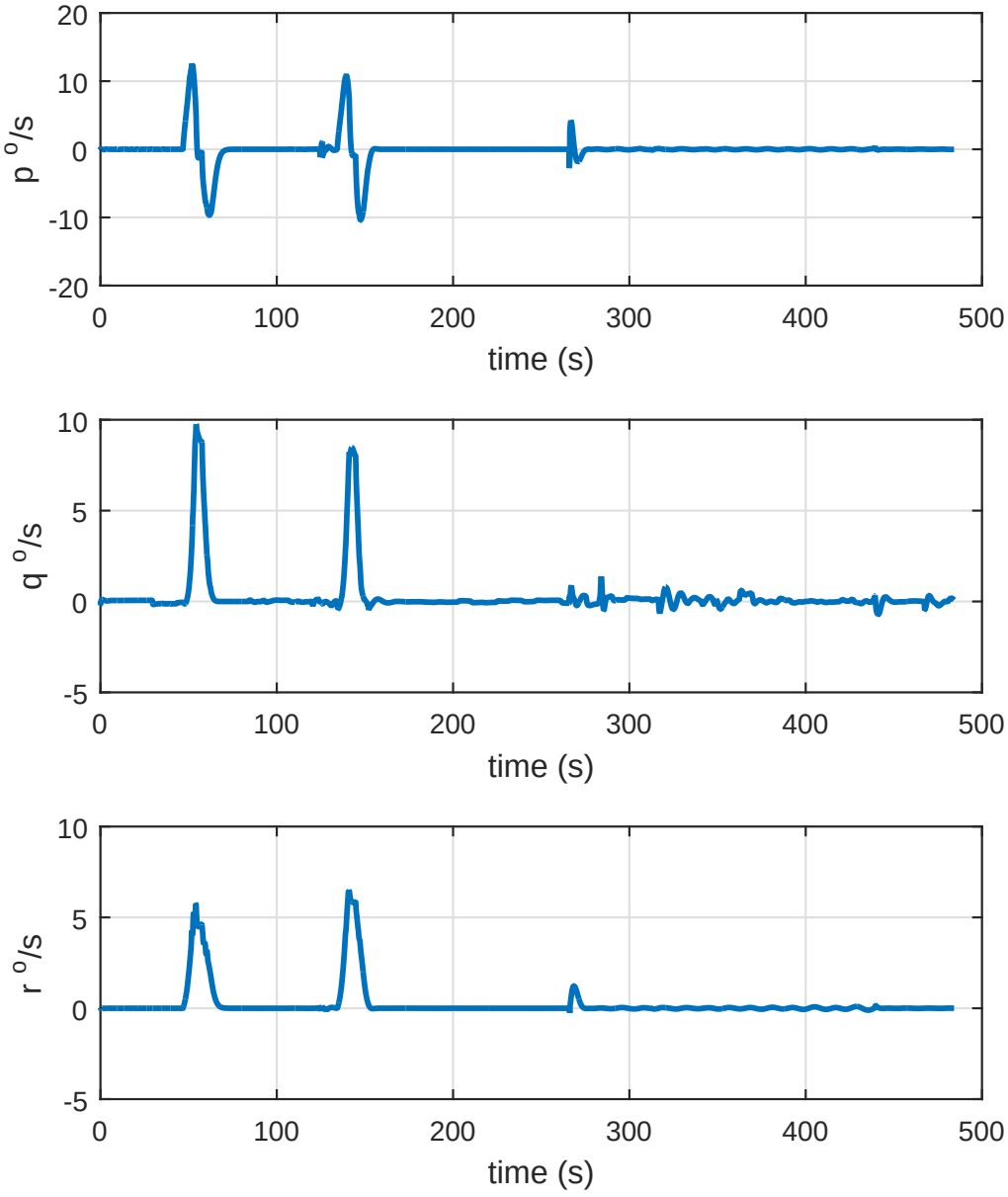

Figure 6.7: Variation of the aircraft's body angular velocities of the aircraft with respect to time

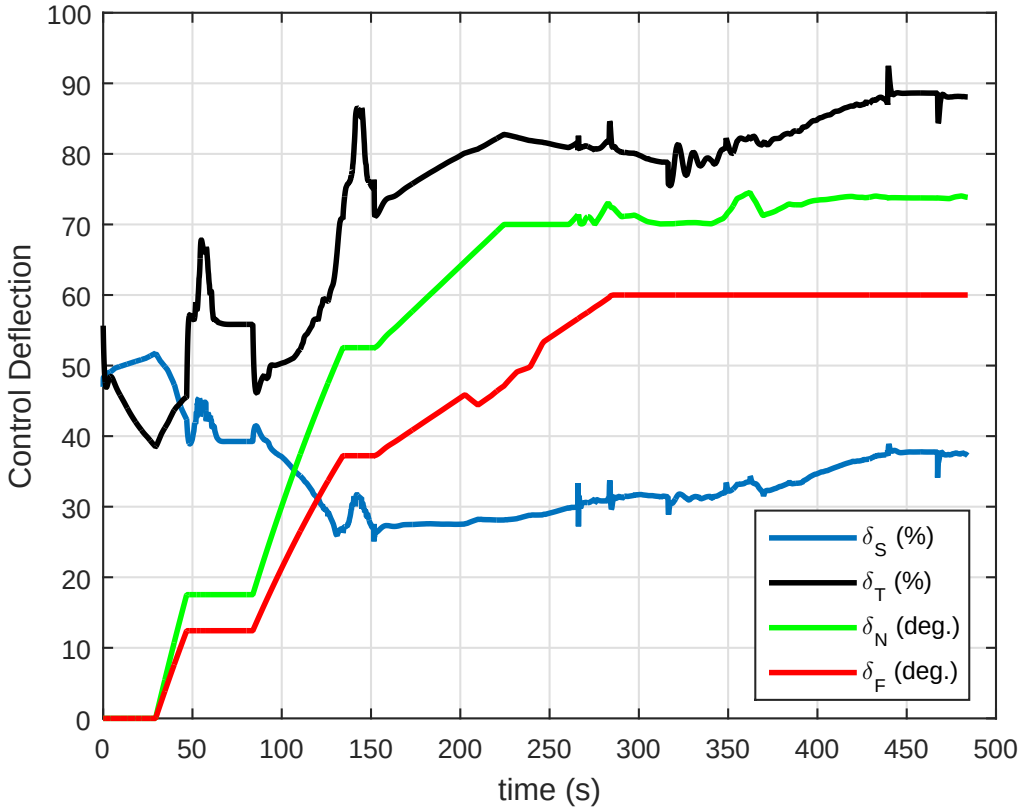

Figure 6.8: Stick, throttle, nozzle and flap deflection history

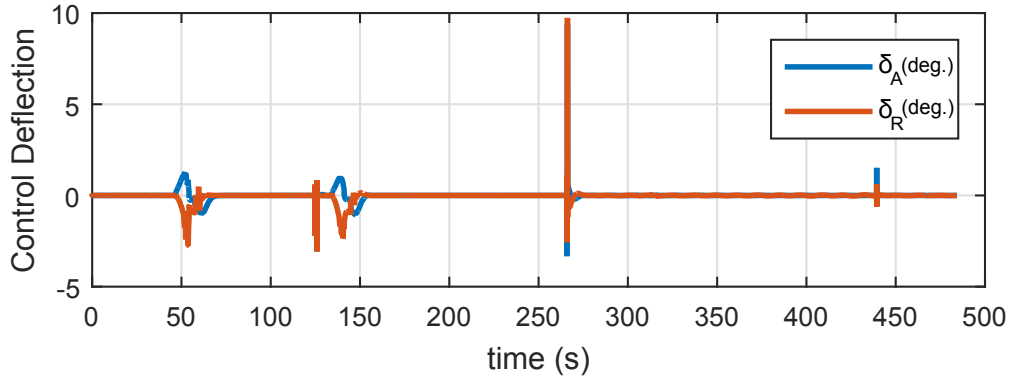

Figure 6.9: Aileron and rudder deflection history

6.2 $\mathcal{L}_1$ adaptive Flight Control System

The simulation results of automatic landing performed using the $\mathcal{L}_1$ adaptive flight control system have been plotted in Figs.(6.10)- (6.18). Fig.(6.1) indicates satisfactory tracking performance. Altitude tracking error is bounded between $\pm 5ft$, while the slip velocity tracking error is maintained less than $0.5ft/s$. The velocity tracking error which increases up to $5ft/s$ prior to touchdown. Also, Fig.(6.11) indicates that the velocity tracking error increases after a time instant of 300 seconds which corresponds to a velocity of $150ft/s$, when the switch from the high-speed to the low-speed $\mathcal{L}_1$ adaptive controller is made. The velocity tracking performance is found to degrade at hover conditions. For this reason, the simulation is terminated at an altitude of 20 ft above the flight deck at 454 seconds., when the aircraft is still in hover. The lateral and longitudinal position of the aircraft at time of termination of the simulation is found to be $4.8ft$ and $-0.68ft$, respectively. The spikes seen in the control histories in Figs(6.17) and (6.18), at 300 seconds is due to the switching between the controllers. However, the velocity tracking performance in hover can be greatly improved by employing a time varying reference as opposed to just two time-invariant reference systems. Also, the touchdown portion of the flight can be conducted by switching to the gain-scheduled controller from the $\mathcal{L}_1$ adaptive controller.

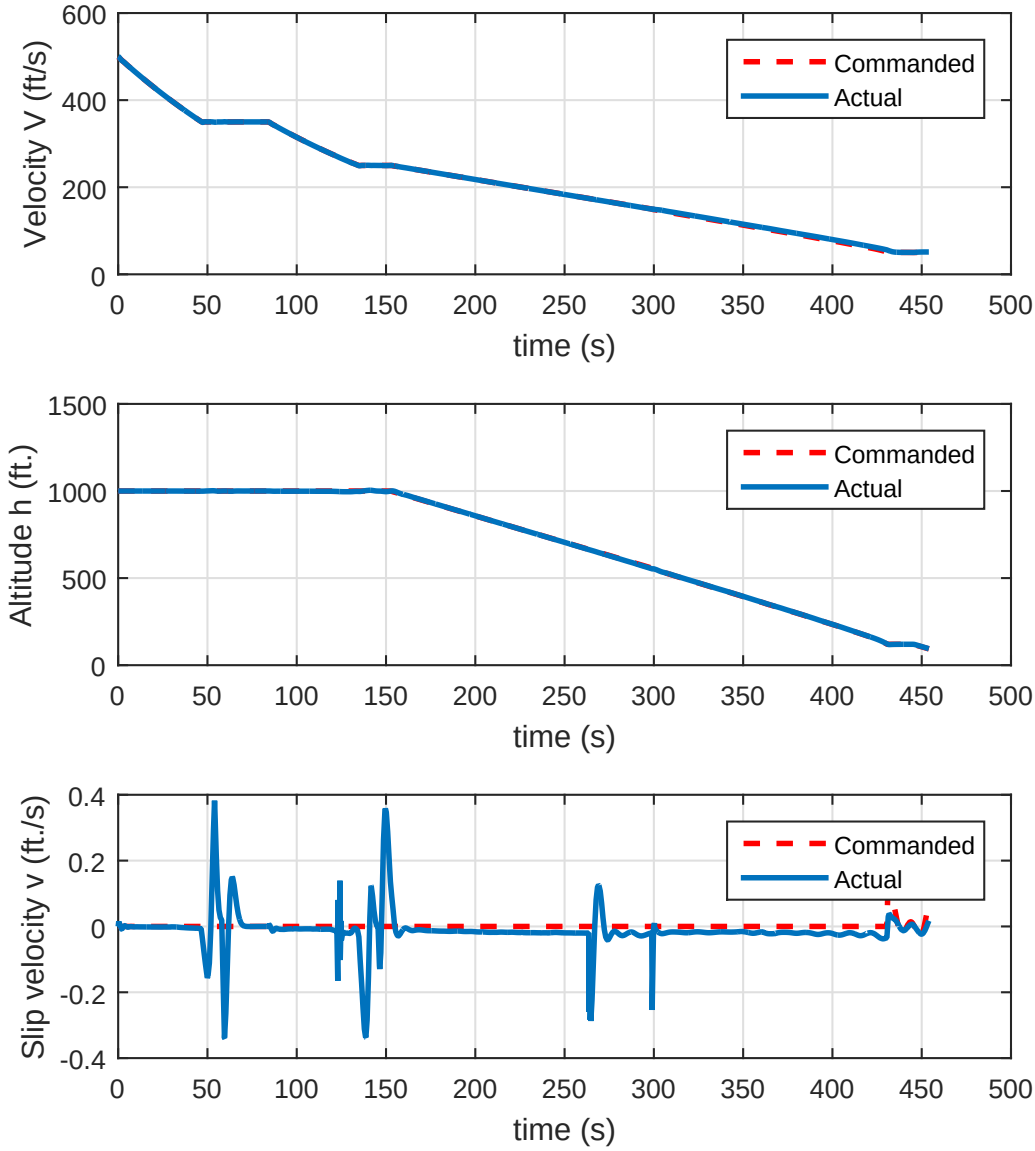

Figure 6.10: Velocity, altitude, and slip tracking performance

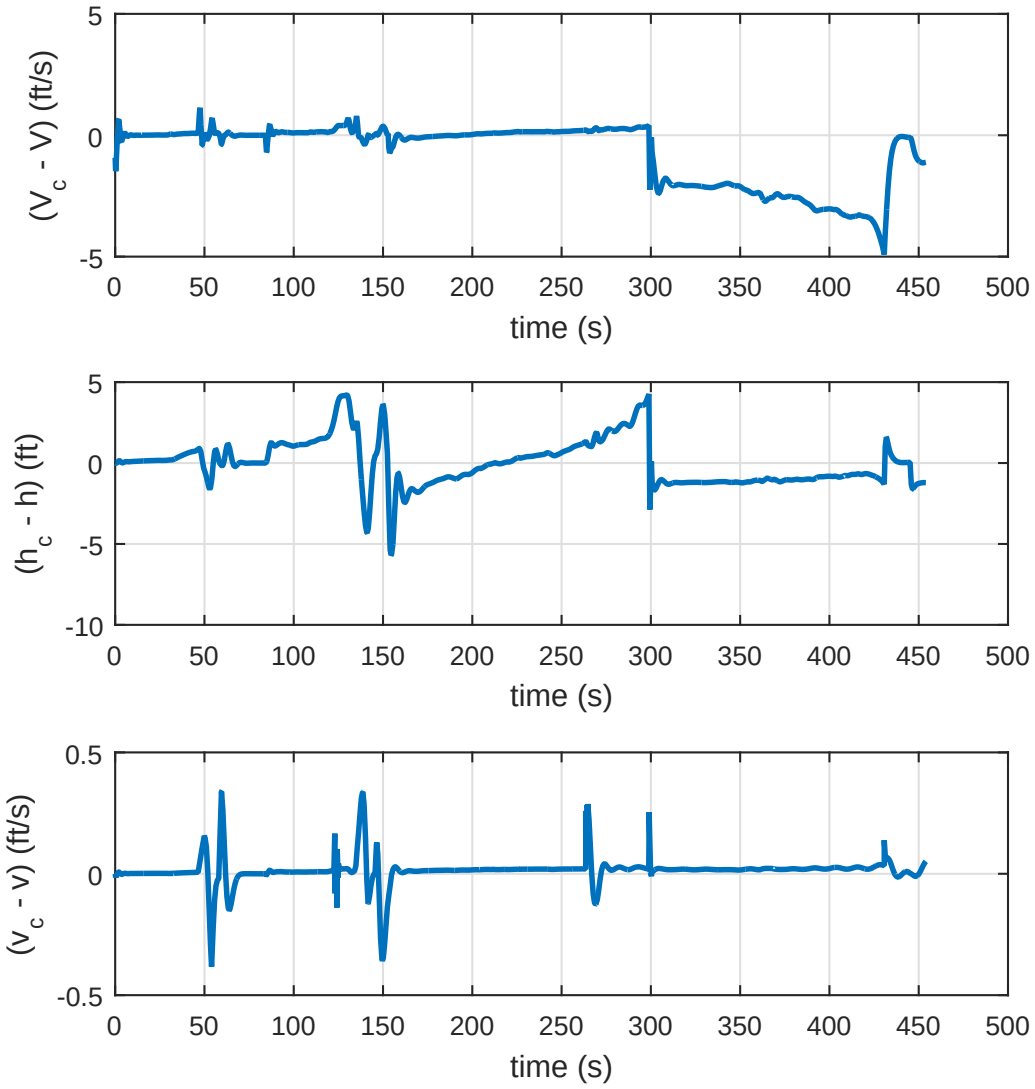

Figure 6.11: Variation of Velocity, altitude, and slip velocity tracking error with time

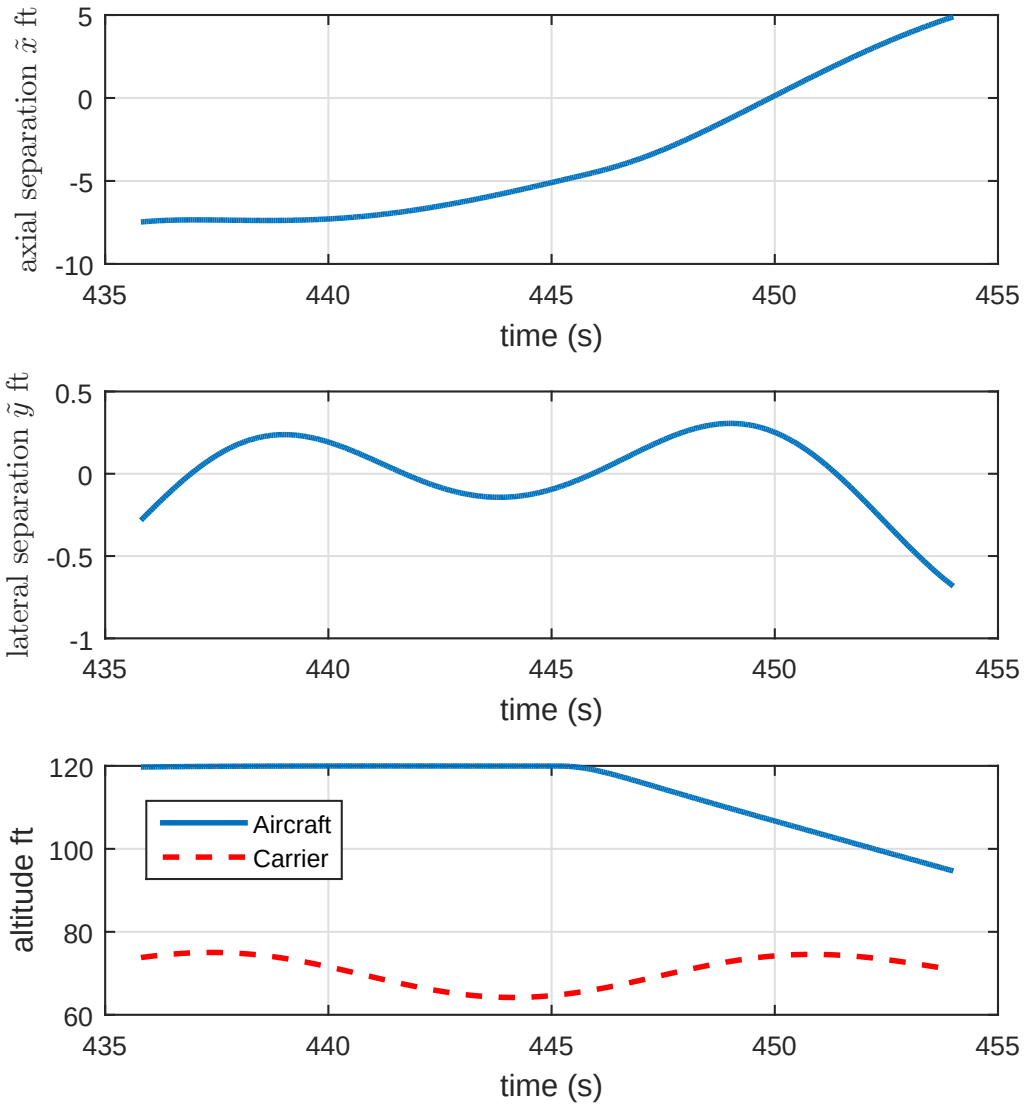

Figure 6.12: Variation of the longitudinal and lateral positions of the aircraft with respect to the carrier plotted along with altitude during touchdown

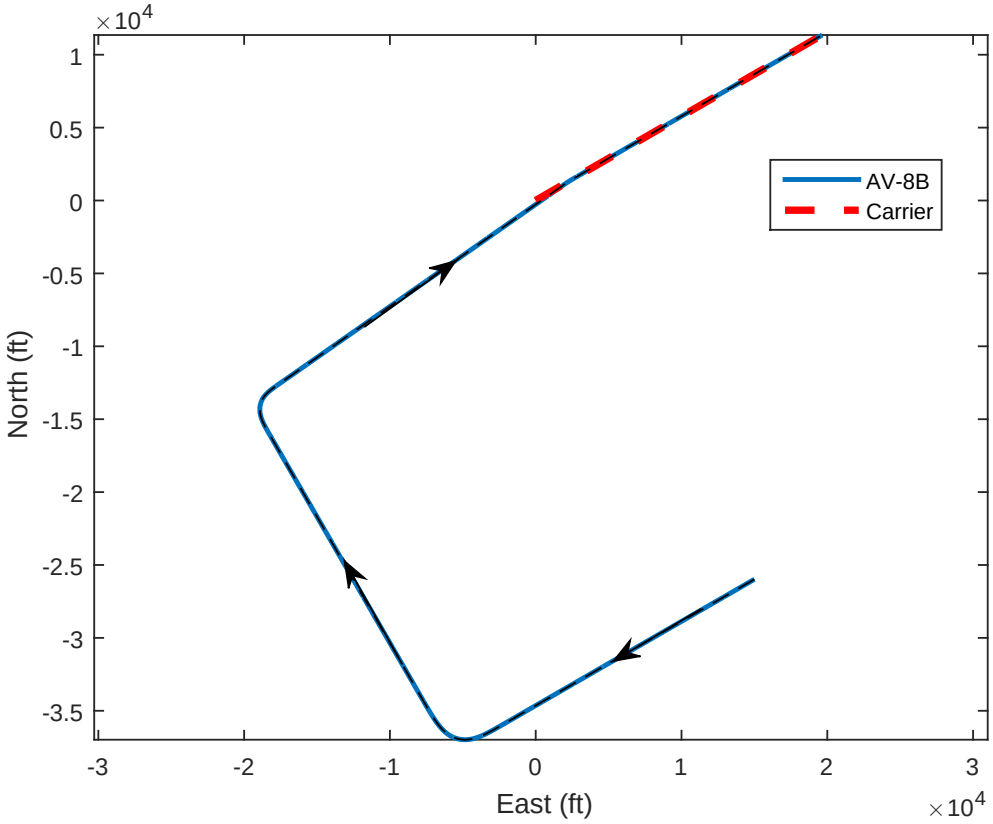

Figure 6.13: Ground track of the aircraft and the carrier

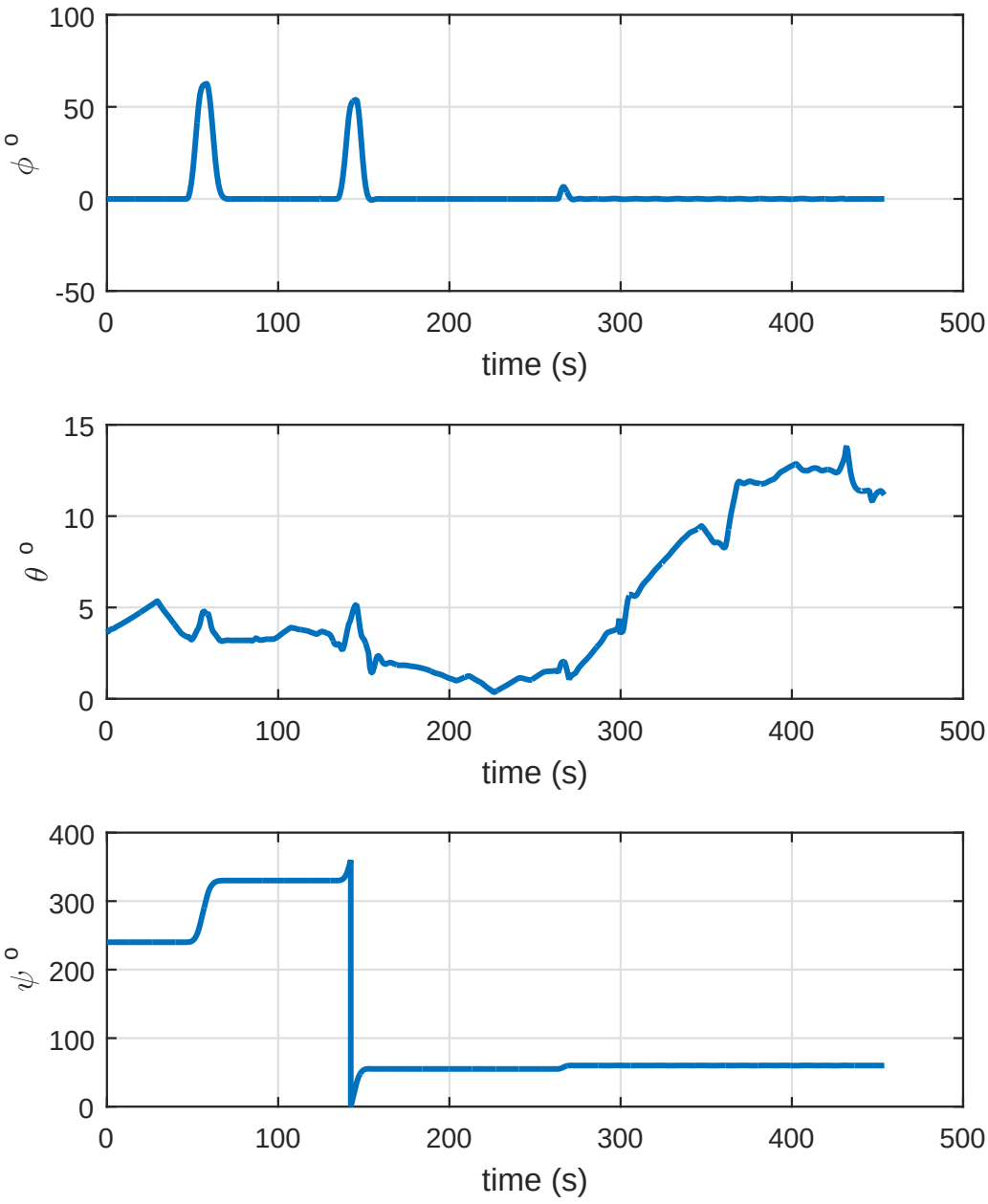

Figure 6.14: Variation of the aircraft's orientation with respect to the inertial frame in time

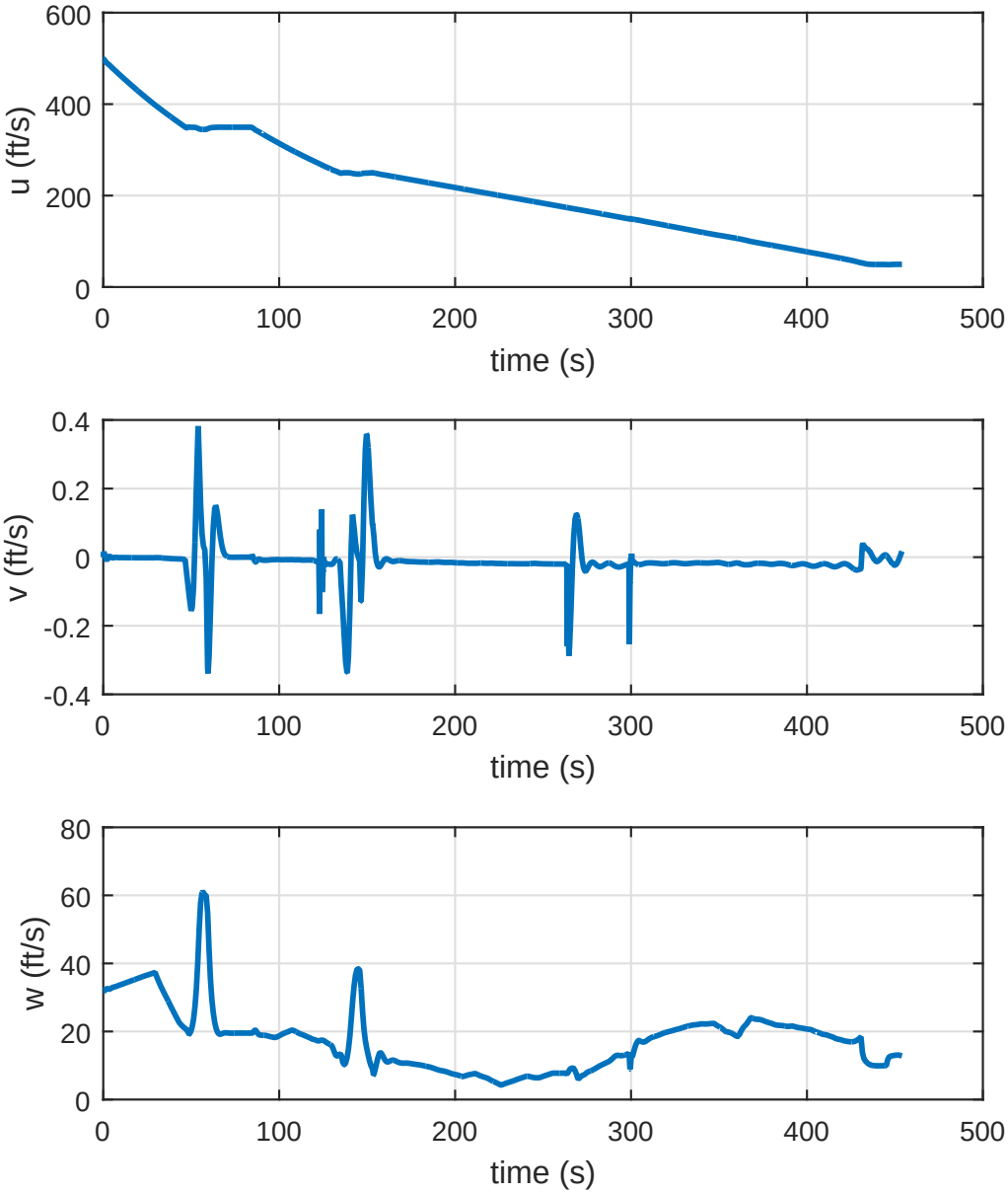

Figure 6.15: Variation of the aircraft's body component of velocities with respect to time

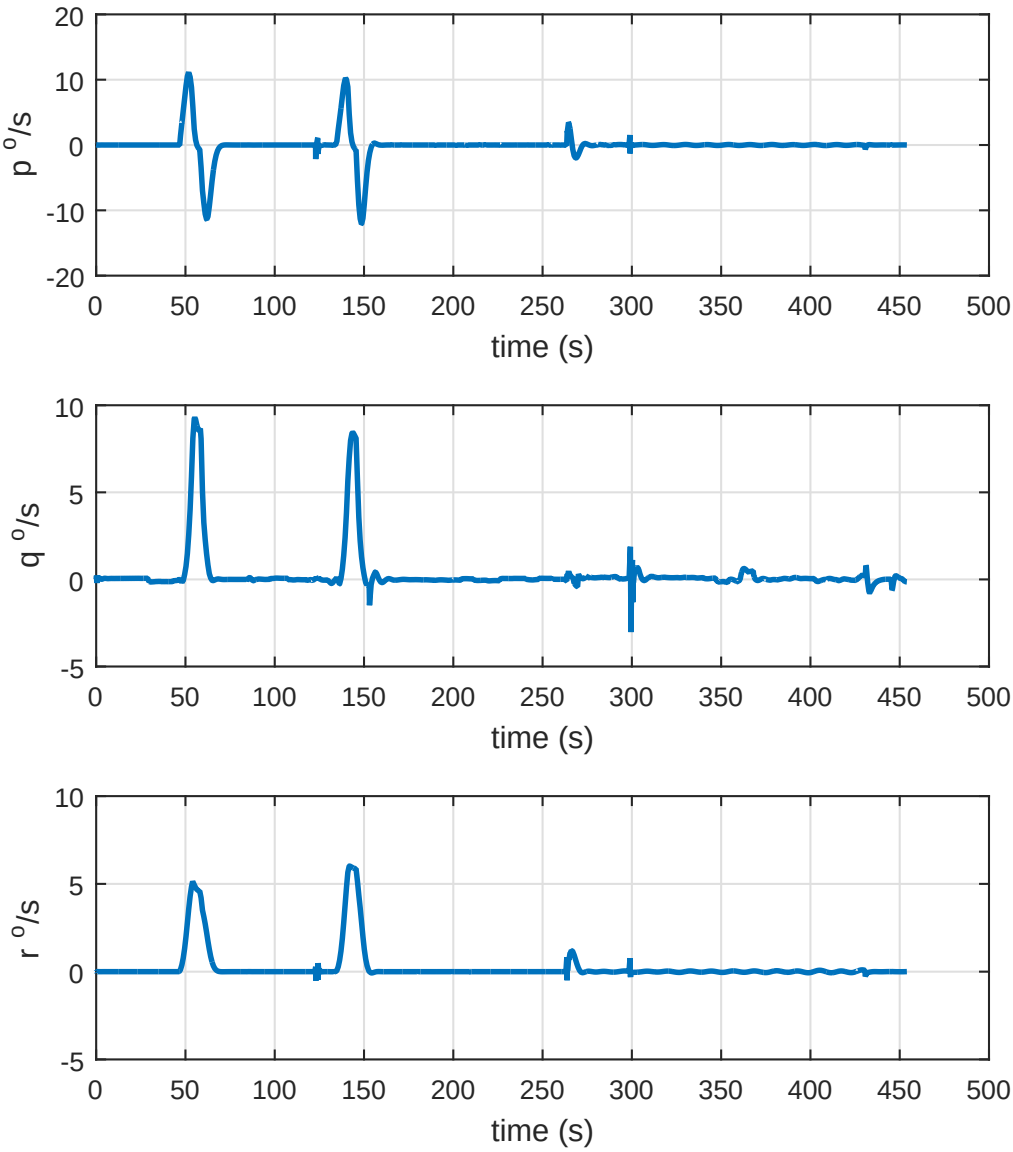

Figure 6.16: Variation of the aircraft's body angular velocities of the aircraft with respect to time

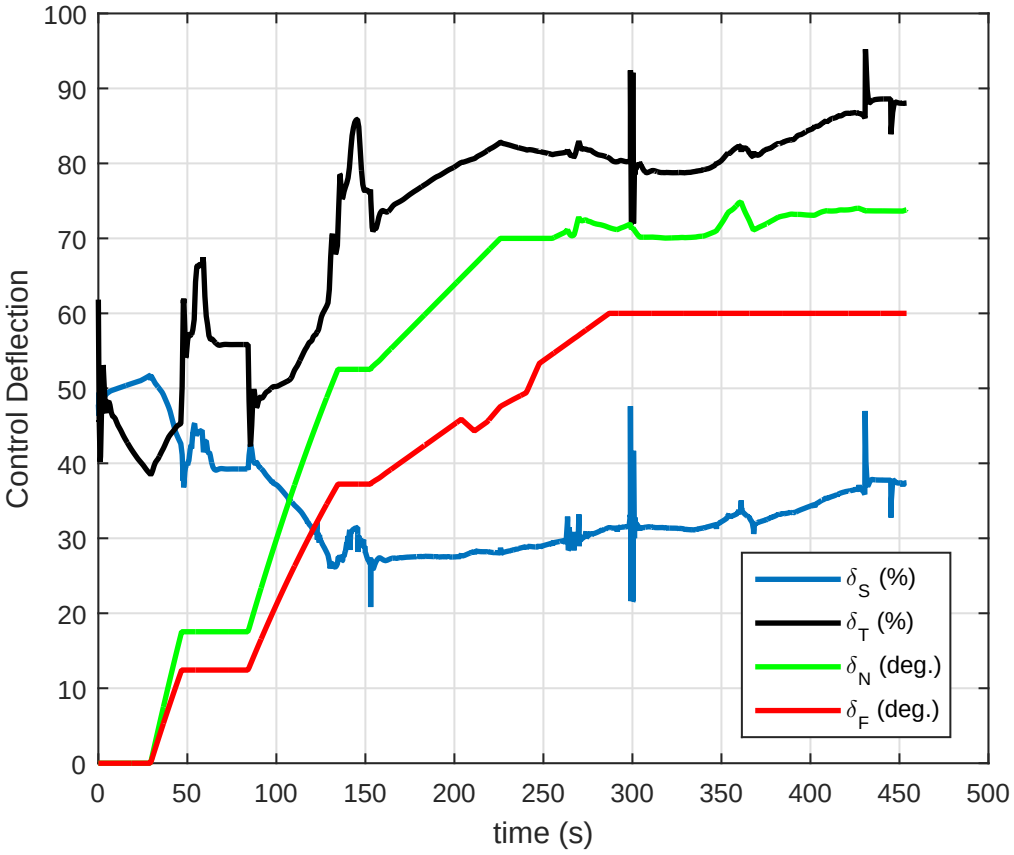

Figure 6.17: Stick, throttle, nozzle and flap deflection history

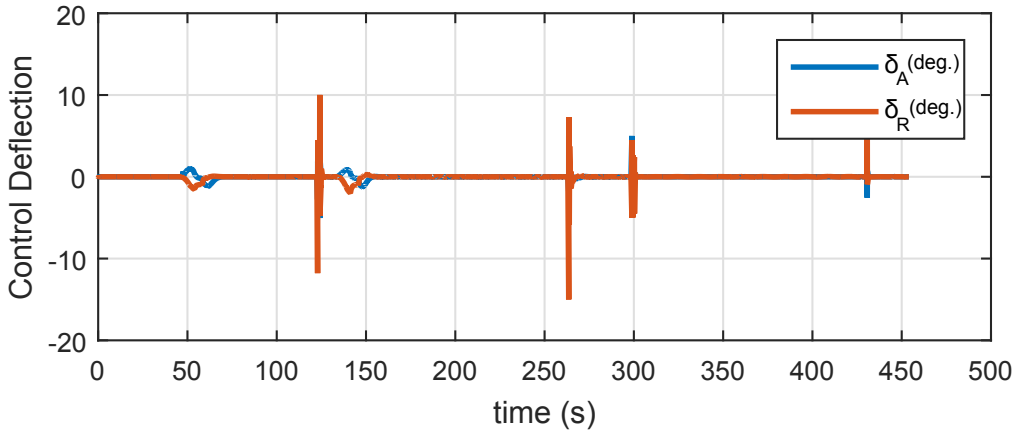

Figure 6.18: Aileron and rudder deflection history

CHAPTER 7

SUMMARY AND CONCLUSION

Automatic carrier landing systems for V/STOL aircraft play a crucial role in minimizing pilot workload, as well as mitigating accidents during shipboard landings. In this thesis, the goal was to design automatic carrier landing systems for AV-8B Harrier like V/STOL aircraft using the two leading control strategies, gain-scheduling, and $\mathcal{L}_1$ adaptive control. A high-fidelity simulation model of the AV-8B Harrier was considered for this purpose. Carrier motion was simulated by employing a kinematic model of a Nimitz class aircraft carrier subjected to sea-state-4 perturbations.

The gain-scheduled flight control system design began with the selection of scheduling variables. The large variations in the aircraft's velocity, turn-rate, and altitude seen in a carrier landing sequence renders the aircraft's dynamics highly non-linear, because of which it was suitable to choose them as scheduling variables. A sample space characterized by velocity, altitude, and turn-rate was defined and discretized to select a large number of equilibrium operating points. Trim states, and control inputs pertaining to these points were determined by the process of constrained minimization of a trim cost function. Linearized dynamics of the aircraft corresponding to each trim point was determined by performing jacobian linearization. Inter-mode coupling and control cross-coupling were investigated at a high-speed straight and level, and a turning flight conditions. While the coupling phenomenon was found to be absent in the straight and level flight condition, they manifested in the turning flight condition. To minimize control cross-coupling, a decoupling strategy was presented whose basis was the concept of partial inversion of the control

influence matrix. At each trimmed flight condition, an LQI controller was developed to track velocity, altitude, and slip. The presence of an integral feedback in the LQI technique ensured the elimination of any steady state error. The trim states and control inputs, and the controller gains pertaining to each trim point were stored in a three dimensional look-up table, and were scheduled with respect to commanded velocity, altitude, and turn-rate, using trilinear interpolation scheme.

The $\mathcal{L}_1$ adaptive flight control system was designed based only on two reference models - one based on a high speed flight condition which functions efficiently at speeds greater than $150 ft/s$, and the other for low-speed and hovering flight conditions. The formulation of the adaptive controller assumed an unknown non-linear matched uncertainty which was transformed to an equivalent linear time varying system. Projection based adaptation laws were incorporated to estimate the uncertainties, and ensure boundedness of the parameters. The low pass filter was chosen to be of first order, and the filter bandwidth was designed to minimize any high frequency noise arising from fast adaptation. The control law being non-linear, still required trim states, and control inputs which were determined from the linear model database that was populated for the gain-scheduled controller. The adaptive controller tracked reference commands of velocity, altitude, slip velocity, and heading angle.

Guidance laws were designed to compute reference commands of airspeed, altitude, turn-rate and slip velocity based on the deviation of the aircraft from a predefined flight path. The flight path consisted of a downwind leg, base leg, and final leg. Heading corrections along each leg was achieved using lateral beam guidance law, while turning maneuvers were performed with the help of a tan-hyperbolic guidance law. Velocity control was achieved with the help of proportional, and time-to-go based guidance laws. The time-to-go velocity guidance law was instrumental in reducing the time taken to rendezvous with the aircraft carrier.

Automatic carrier landing was simulated using both the $\mathcal{L}_1$ adaptive and the gain-scheduled controllers, and their overall performance was satisfactory. The velocity tracking performance of the $\mathcal{L}_1$ adaptive controller degraded in hover conditions because of which the vertical touchdown was partially completed, and the simulation was terminated when the aircraft was $20ft$ above the flight deck. However, the performance of the $\mathcal{L}_1$ adaptive controller at hover conditions can be greatly improved by accounting for unmatched uncertainties and by employing time-varying reference systems. The $\mathcal{L}_1$ adaptive controller performed better than the gain-scheduled controller when slip velocity tracking is considered.

CHAPTER 8

FUTURE WORK

Based on the techniques and ideas presented in this thesis, the future work can encompass :

- Considering robust multi-input-multi-output techniques such as $\mathcal{H}_\infty$, LQG-LTR, and μ-synthesis for designing the gain-scheduled automatic flight control system.
- Designing an $\mathcal{L}_1$ adaptive flight control system which can handl unmatched uncertainties.
- Selection of the low-pass filter in the $\mathcal{L}_1$ adaptive controller to maximize time delay margin.
- Including actuator dynamics, and time delays to make the controllers more robust.
- Including winds, turbulences, and burble models which were completely ignored in this research.
- Considering time-varying reference systems for the adaptive controller
- Designing an $\mathcal{L}_1$ adaptive augmented gain-scheduled flight control system to combine the benefits of both the techniques.

REFERENCES

[1] Walters, Robert Victor."*Microprocessor Control of Low Speed VSTOL Flight.*", Naval Academy, Annapolis, MD, Div. of Engineering and Weapons, 1979.

[2] Anon.," *AV-8B Aircraft Class A Mishaps and Engine Problems.*", Office of Inspector General, DoD

[3] Davies, W. D. T., and Roger Noury. ,"*AN/SPN-42 Automatic Carrier Landing System.*", Proceedings of the First Annual Advanced Control Conference. Chicago: Dun-Donnelley Publ. Corp., 1974.

[4] P. Nuthi and K. Subbarao, "*Autonomous Vertical Landing on a Marine Vessel.*", AIAA Atmospheric Flight Mechanics Conference, 2014. Proceedings of AIAA, Scitech 2014, 2014.

[5] McMuldroch, Christopher G. "*VTOL Controls for Shipboard Landing.*" MS thesis, M. I. T., Dept. of Aeronautics, 1979.

[6] Hauser, John, Shankar Sastry, and George Meyer, "*Nonlinear Control Design for Slightly Non-Minimum Phase Systems: Application to V/STOL aircraft.*", Automatica 28.4 (1992): 665-679.

[7] Marconi, Lorenzo, Alberto Isidori, and Andrea Serrani. " *Autonomous vertical landing on an oscillating platform: an internal-model based approach.*" Automatica 38.1 (2002): 21-32.

[8] Denison, Nicholas A., "*Automated carrier landing of an unmanned combat aerial vehicle using dynamic inversion.*" No. AFIT/GAE/ENY/07-J06. AIR FORCE INST OF TECH. WRIGHT-PATTERSON AFB OH SCHOOL OF ENGINEERING AND MANAGEMENT, 2007.

[9] , Fitzgerald, Pio. "Flight control system design for autonomous UAV carrier landing." (2004).PhD Thesis, http://dspace.lib.cranfield.ac.uk/handle/1826/840

[10] G. Ziegler, "*AV-8B Batch Simulator User's Guide", Texas A&M University*", Aerospace Engineering, College Station, Tx, August 1998.

[11] Dogan A, "*AE-5302 Advanced Flight Mechanics*" Lecture notes, 2014

[12] Stevens, Brian L., and Frank L. Lewis. "*Aircraft Control and Simulation*" John Wiley & Sons, 2003.

[13] "*NATOPS Flight Manual Navy Model AV8B/TAV8B 161573 and Up Aircraft*, retrieved from "https://publicintelligence.net/u-s-navy-natops-av-8b-harrier-ii-flight-manuals/"

[14] Lallman, Frederick J. "*Relative Control Effectiveness Technique with Application to Airplane Control Coordination*", Vol. 2416. National Aeronautics and Space Administration, Scientific and Technical Information Branch, 1985.

[15] Honeywell Technology Center, Lockheed Martin - Skunkworks "*Application of Multivariable Control Theory to Aircraft Control laws : Multivariable Control Design Guidelines*", Final Report, Flight Dynamics Directorate, Wright Patterson Air Force Base, May 1996

[16] Heller, Matthias, Thaddus Baier, and Falko Schuck. "*Lateral Fly by Wire Control System Dedicated to Future Small Aircraft*", Advances in Aerospace Guidance, Navigation and Control (2013): 353-372.

[17] Gregory, Irene, Ross Gadient, and Eugene Lavretsky. " *Flight Test of Composite Model Reference Adaptive Control (CMRAC) Augmentation Using NASA AirSTAR Infrastructure*" AIAA Guidance, Navigation, and Control Conference. 2011.

[18] Wise, Kevin, et al. "*Adaptive Flight Control of a Sensor Guided Munition*" AIAA Guidance, Navigation and Control Conference, San Francisco, USA. 2005.

[19] Cao, Chengyu, and Naira Hovakimyan, " *Design and Analysis of a Novel* $\mathcal{L}_1$ *Adaptive Controller, Part I: Control Signal and Asymptotic Stability*" American Control Conference, 2006. IEEE, 2006.

[20] Hovakimyan, Naira, and Chengyu Cao "$\mathcal{L}_1$ *Adaptive Control Theory: Guaranteed Robustness with Fast Adaptation*" Vol. 21. Siam, 2010.

[21] Gregory, Irene M., et al. ," $\mathcal{L}_1$ *Adaptive Control Design for NASA AirSTAR flight test vehicle*" AIAA guidance, navigation, and control conference. Vol. 5738. 2009.

[22] Cao, Chengyu, et al. "Stabilization of cascaded systems via L1 adaptive controller with application to a UAV path following problem and flight test results." American Control Conference, 2007. ACC'07. IEEE, 2007.

[23] Kaminer, Isaac, et al. "Coordinated path following for time-critical missions of multiple UAVs via L1 adaptive output feedback controllers." AIAA Guidance, Navigation and Control Conference and Exhibit. 2007.

[24] Michini, Buddy, and Jonathan How. "L1 adaptive control for indoor autonomous vehicles: design process and flight testing." Proceeding of AIAA Guidance, Navigation, and Control Conference. 2009.

[25] Wang, Jiang, et al. "L1 adaptive control of a uav for aerobiological sampling." American Control Conference, 2007. ACC'07. IEEE, 2007.

[26] Leman, Tyler J., et al.," $\mathcal{L}_1$ *Adaptive Control Augmentation System for the X-48B Aircraft*" Diss. University of Illinois, 2010.

[27] Patel, Vijay V., et al., " $\mathcal{L}_1$ *Adaptive Controller for Tailless Unstable Aircraft*" American Control Conference, 2007. ACC'07. IEEE, 2007.

[28] Liu, Ri, et al., " *Dynamics Modeling and L1 Adaptive Control of a Transport Aircraft for Heavyweight Airdrop*", Mathematical Problems in Engineering 501 (2015): 365130.

[29] Lavretsky, Eugene, Travis E. Gibson, and Anuradha M. Annaswamy "*Projection Operator in Adaptive Systems*" arXiv preprint arXiv:1112.4232 (2011).

[30] Blakelock, John H. "*Automatic control of aircraft and missiles*" John Wiley & Sons, 1991.

[31] Schust, A. P., P. N. Young, and W. R. Simpson ," *Automatic Carrier Landing System (ACLS) Category 3 Certification Manual. No. 1506-01-1-2750.* ARINC Research Corp, Annapolis, MD, 1982.

[32] "*V/STOL Shipboard And Landing Signal Officer Manual*", Naval Air Systems Command, Pax river,MD.

[33] Anderson, Mark R. ,"*Inner and Outer Loop Manual Control of Carrier Aircraft Landing*", AIAA Guidance, Navigation and Control Conference. Reston, VA: AIAA, 1996.

[34] Burken, John, " *Fundamentals of Aircraft Flight Control", Lecture Slides, NASA Engineering Safety Center*, NESC GNC-Webcast, Oct. 17 2012.

[35] Shamma, Jeff S.," *Analysis and Design of Gain-Scheduled Control Systems*", Diss. Massachusetts Institute of Technology, 1988.

[36] Shamma, Jeff S., and Michael Alhans. "*Gain Scheduling: Polential Hazards and Possible Remedies*". (1992).

BIOGRAPHICAL STATEMENT

Shashank Hariharapura Ramesh was born in the city of Bengaluru, India in 1989. He received his B.E. degree in Mechanical Engineering from B.M.S. College of Engineering, India, in 2011. He worked on rotor-dynamics of micro jet engines for his undergraduate project at CSIR - National Aerospace Laboratories, India. Before leaving his hometown for graduate studies, he worked as a research assistant at his alma mater, on using magneto-rheological fluids for isolating vibrations in rotating machinery. In 2013, Shashank moved to USA to pursue M.S. in Aerospace Engineering at the University of Texas at Arlington where he specialized in dynamics and control of aircraft. His current research interests include automatic flight control, non-linear control systems, and flight dynamics of highly maneuverable aircraft. His hobbies include music production, photography and sketching. He is also an avid aircraft enthusiast.